

UNIVERSITÉ LIBRE DE BRUXELLES

IIHE

FACULTÉ DES SCIENCES - DÉPARTEMENT DE PHYSIQUE

---

**Triple-GEM time resolution measurement for  
their installation in CMS**

---

*Author:*  
Laurent Pétré

*Supervisors:*  
Pr. Gilles De Lentdecker  
Pr. Frédéric Robert



Academic year 2017-2018

MÉMOIRE PRÉSENTÉ EN VUE DE L'OBTENTION DU DIPLÔME DE MASTER EN SCIENCES  
PHYSIQUES



## Abstract

The upcoming upgrades of the LHC will increase its luminosity up to  $10 \times 10^{34} \text{ cm}^{-2} \text{ s}^{-1}$ . To that extent, CMS will be upgraded to handle the increasing rate of particles, especially in the most forward regions,  $|\eta| > 1.6$ . The GEM Collaboration proposes to install triple-GEM gaseous detectors in the  $1.6 < |\eta| < 2.2$  region during the LS2 (2019-2020) with a project called GE1/1. During the quality control tests, the time resolution of the detector will be tested and must be better than 10 ns.

In order to improve the efficiency and reduce the costs of the procedures, we propose to implement the required TDC within the FPGA present on the embedded DAQ electronics. The final version of our embedded TDC reaches performances better than 150 ps in time resolution for a range of 3.2  $\mu\text{s}$ . The methodology and results are successfully crosschecked with a commercial TDC. Finally, we measure the time resolution of the triple-GEM detector with the version 2a of the electronics. The best value we measure is  $9.91 \pm 0.08 \text{ ns}$  for a drift field of 2.89 kV/cm.

**Keywords** HL-LHC, CMS, GE1/1, triple-GEM, FPGA, TDC, time resolution

## Résumé

Les mises à jour à venir du LHC vont augmenter sa luminosité jusqu'à  $10 \times 10^{34} \text{ cm}^{-2} \text{ s}^{-1}$ . À cet égard, CMS sera mis à jour pour gérer l'augmentation du taux de particules, particulièrement dans les régions les proches de l'axe des faisceaux,  $|\eta| > 1.6$ . La Collaboration GEM propose d'installer des détecteurs triple-GEM dans la région  $1.6 < |\eta| < 2.2$  pendant le LS2 (2019-2020) avec un projet dénommé GE1/1. Lors des tests de contrôle de qualité, la résolution temporelle sera testée et devra être meilleure que 10 ns.

Pour améliorer l'efficacité et réduire les coûts des procédures, nous proposons d'implémenter le TDC nécessaire dans un FPGA déjà présent dans l'électronique d'acquisition. La version finale de notre TDC atteint des performances supérieures à 150 ps en terme de résolution temporelle pour un intervalle de mesure de 3.2  $\mu\text{s}$ . La méthodologie ainsi que les résultats sont comparés avec un TDC commercial. Finalement, nous mesurons la résolution temporelle du détecteur triple-GEM équipé de la version 2a de son électronique. La meilleure valeur obtenue est de  $9.91 \pm 0.08 \text{ ns}$  pour un champ de dérive de 2.89 kV/cm.

**Mots-clés** HL-LHC, CMS, GE1/1, triple-GEM, FPGA, TDC, résolution temporelle



# Acknowledgments

Je tiens avant tout à remercier mes deux promoteurs pour leur aide précieuse dans la réalisation de ce mémoire. Le Prof. Gilles de Lentdecker pour son aide tout au long de mon travail et tout particulièrement pour sa relecture poussée. Le Prof. Frédéric Robert pour ses nombreux conseils ayant permis de faciliter la compréhension du mémoire.

Je remercie par avance mes relecteurs qui, je l'espère, apprécieront la lecture de mon mémoire.

I would to thanks the numerous people which are or were part of the GEM Collaboration for answering all my (sometimes naive) questions : Thomas Lenzi, Brian Dorney, Evaldas Juska, Andrew Peck, Yifan Yang and presently forget to mention.

Je remercie mes parents pour m'avoir toujours encouragé à et permis de poursuivre les études je souhaitais. Merci à ma maman pour avoir supporté ma, parfois, mauvaise humeur due au stress et à la frustration de résultats qui tardaient à arriver. Merci à mon papa de m'avoir introduit dès mon plus jeune âge aux sciences.

Finalement, merci à tous mes camarades et ami · e · s pour ces années d'étude (et plus) passées en leur compagnie : Aidan, Alice, Antoine, Louis, Martin, Morgane, Quentin et tous les autres. Aah,les puzzles du NO. ;-)

Profondément, merci !



# Contents

<b>Abstract</b>	<b>i</b>
<b>Acknowledgments</b>	<b>iii</b>
<b>Contents</b>	<b>v</b>
<b>Introduction</b>	<b>1</b>
<b>1 CMS, an experiment at the LHC</b>	<b>3</b>
1.1 The LHC	3
1.1.1 Main characteristics	5
1.1.2 LHC Planning	5
1.2 The CMS experiment	6
1.2.1 System of coordinates	6
1.2.2 Subdetectors	6
1.2.3 Muon subsystem	8
1.2.4 Trigger system	10
1.2.5 Upgrade	11
<b>2 Gaseous detectors</b>	<b>13</b>
2.1 Energy losses in medium	13
2.2 Gaseous detectors	14
2.2.1 Total ionization	14
2.2.2 Amplification	15
2.2.3 Drift	16
2.3 Technologies currently used in CMS	17
2.3.1 The drift tubes	17
2.3.2 The cathode strips chamber	17
2.3.3 The resistive plate chamber	18
2.4 Triple-GEM detectors	20
2.5 Factors affecting the time resolution	22
<b>3 The GE1/1 project</b>	<b>23</b>
3.1 Overview	23
3.2 GE1/1 chamber	25
3.3 Readout electronics	26
3.3.1 The VFAT3	26
3.3.2 The GEB	27
3.3.3 The opto-hybrid	28

3.3.4	Off-detector electronics . . . . .	28
3.4	Readout electronics used in this master thesis . . . . .	28
3.4.1	Electronics v2a . . . . .	30
<b>4</b>	<b>Implementation of the TDC</b>	<b>33</b>
4.1	What is an FPGA ? . . . . .	34
4.1.1	LUTs . . . . .	35
4.1.2	Clocks and flip-flops . . . . .	35
4.1.3	Carry logic . . . . .	36
4.2	Tapped delay line . . . . .	37
4.3	Implementation of the TDC . . . . .	37
4.3.1	Calibration . . . . .	38
4.3.2	Wave Union A . . . . .	41
4.3.3	Bubbles . . . . .	41
4.4	Performances . . . . .	41
4.5	Implementation in the GE1/1 opto-hybrid . . . . .	44
<b>5</b>	<b>Measurements and analysis</b>	<b>47</b>
5.1	Measurement principle . . . . .	47
5.2	The experimental setup . . . . .	49
5.2.1	Sources of uncertainties . . . . .	49
5.3	Simulations . . . . .	50
5.4	Crosscheck of the embedded TDC . . . . .	51
5.5	Optimized setup . . . . .	53
5.5.1	GEM detector optimizations . . . . .	53
5.5.2	Trigger optimizations . . . . .	56
5.5.3	Summary . . . . .	62
5.6	Results . . . . .	62
5.6.1	Influence of the drift field . . . . .	63
5.6.2	Geometrical selection . . . . .	63
5.6.3	Conclusions . . . . .	63
	<b>Conclusion</b>	<b>67</b>
	<b>A Delay line code</b>	<b>69</b>
	<b>List of Figures</b>	<b>73</b>
	<b>List of Tables</b>	<b>75</b>
	<b>Bibliography</b>	<b>77</b>

# Introduction

The *Large Hadron Collider (LHC)* is the world's largest and most powerful particle accelerator. Built between 2000 and 2008, it collides protons at energies of up to 7 TeV 40 million times per second.

While the LHC is regularly upgraded, the *Long Shutdown 3 (LS3)* between 2024 and 2026 will represent a crucial milestone for the search of new physics. Its nominal luminosity should grow from  $10^{34} \text{ cm}^{-2}\text{s}^{-1}$  to  $10 \times 10^{34} \text{ cm}^{-2}\text{s}^{-1}$ . The *High Luminosity-LHC (HL-LHC)*, as it is called, will also increase the maximal energy of the proton to 8 TeV.

This increased luminosity will raise the radiation doses and the particle rate for all the LHC experiments. The *Compact Muon Solenoid (CMS)* experiment, a general purpose particle detector, was not planned for such operating conditions and must therefore go under a phase of upgrades.

This is particularly the case for the most forward regions of the muon subsystem at  $|\eta| > 1.6$ . One of the main difficulties is to maintain the efficiency of the *Level-1 (L1)* trigger whose function is to select the relevant events among the 40 million collisions per second for further processing with a maximal latency of  $3.2 \mu\text{s}$ . The muon subsystem will be equipped with new detectors in order to maintain the efficiency of the L1 muon trigger, but also improve the muon track reconstruction as well as improving the redundancy of the  $|\eta| > 1.6$  region.

The GEM Collaboration has proposed the GE1/1 project to fulfill these needs. The GE1/1 project schedules to install 144 gaseous detector chambers based on the triple-GEM technology in the space left vacant for the innermost layers of *Resistive Plate Chamber (RPC)* gaseous detectors in the muon endcap. During development stages, it was proven that the triple-GEM technology can reach a spatial resolution better than  $300 \mu\text{rad}$  in  $\eta$ , a time resolution better than 10 ns and an efficiency above 97%.

Before their installation in CMS during the *Long Shutdown 2 (LS2)* in 2019-2020, the 144 GE1/1 chambers must pass *Quality Control (QC)* tests. Among the parameters to be tested, this master thesis focuses on the time resolution. It is defined as the standard deviation of the Gaussian distribution of the time difference between the passage of a muon through the detector and the signal detected at the output of the detector. Only detectors with a time resolution better than 10 ns are qualified.

Until now, measurements have been made using external, commercially available, devices called *Time-to-Digital Converter (TDC)*. While they are dedicated to the measurement of time intervals, the logistics and prices are major disadvantages for their use in the QC tests.

This master thesis proposes to implement a TDC within a fully programmable digital device, called an *Field Programmable Gate Array (FPGA)*, already present on the *Data Acquisition (DAQ)* electronics of each GE1/1 chamber. To prove the correct behaviour of the solution, measurements have been compared to a commercial solution as a cross-check. Moreover, we spend time to reproduce the time resolution values measured in previous works.

The chapter 1 of this master thesis describes the LHC and CMS. We emphasize on the LHC upcoming upgrades and their implications for the CMS experiment. The chapter 2 details the gaseous detector working principles and how they impact the time resolution. The gaseous detectors used in CMS are described with a focus on the triple-GEM technology. The chapter 3 describes the GE1/1 project which will be the first to use triple-GEM detectors in CMS. We explain the required characteristics of a gaseous detector located in a  $|\eta| > 1.6$  region as well as the GE1/1 DAQ electronics.

The TDC implementation is thoroughly explained in the chapter 4. After a quick explanation of the FPGA working principles and the basics of the delay, we detail the issues emerging from the implementation of a TDC on a FPGA. The final section is dedicated to the characterisation of the newly created TDC.

The time resolution measurements are done in the chapter 5. We begin by explaining the measurement principle and the setup we used. In order to achieve the most precise measurement, we detail the numerous optimizations. Finally, we present the actual measurements and the final results.

# Chapter 1

## CMS, an experiment at the LHC

In this chapter we introduce the Large Hadron Collider (LHC) and its key features as well as its planned upgrades. The Compact Muon Solenoid (CMS) experiment is later described with more details. We close the chapter with its upgrades made necessary to cope with the LHC upgrades.

### 1.1 The LHC

The LHC [17] is part of the CERN accelerator complex and is the world's largest and most powerful particle accelerator. Its construction spans from 2000 to 2008 in the tunnel which was previously used by the Large Electron-Positron (LEP) collider 100 m under the France–Switzerland border, near Geneva.

The LHC is built around a 27 km ring of two parallel pipes where an ultrahigh vacuum prevails. Superconducting dipole magnets confine beams of hadrons within these pipes. Although beams can be composed of heavy ions bunches, most of the time the LHC collides bunches of protons.

The beams circulate in opposite directions before being focused to collide in four interaction points at a frequency of 40 MHz. Quadrupole and octupole magnets focus and defocus the beams around the interaction points.

The bunches are provided to the LHC by the different accelerators present in the CERN complex (see figure 1.1). The energy of the protons is increased in multiple steps :

1. The protons are extracted from hydrogen whose electrons are stripped away.
2. The first acceleration step from rest is done by a linear accelerator, the LINAC2. The protons have reached an energy of 50 MeV at its output.
3. The protons are then injected into the Proton Synchrotron (PS) via the Booster. They are accelerated to 25 GeV.
4. The Super Proton Synchrotron (SPS) speeds up the protons up to 450 GeV.
5. They are finally transferred to the LHC where the final acceleration takes place into radiofrequency cavities. The protons reach their nominal energy of 7 TeV.

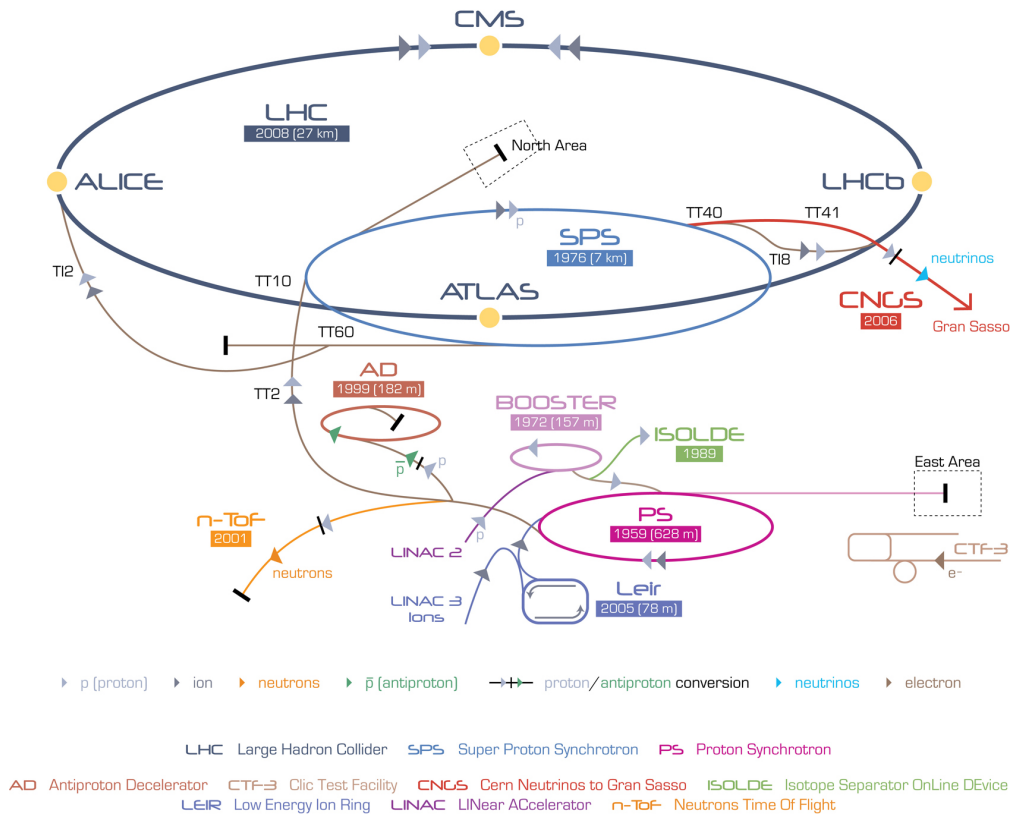


Figure 1.1 – Overview of the CERN accelerator complex. The LHC and its four main experiments are drawn in blue. The proton accelerating chain is composed (in order) by the LINAC2 (purple), the BOOSTER (rose), the PS (magenta) and the SPS (blue). [15]

Four experiments are located in caverns at the four interaction points. Both CMS [19] and ATLAS [9] are general-purpose detectors. Their main goals are the precise measurement of the standard model and the searches for new physics. They also successfully discovered the Brout-Englert-Higgs boson [18, 8]. While their goals are similar, their designs and technologies are different in order to crosscheck the results.

ALICE [4] is designed to analyse the heavy ion collisions. Such collisions permit the study of the Quantum ChromoDynamics (QCD) and particularly the properties of quark-gluon plasma. LHCb [34] is specialized in the study in the asymmetry present in the B-particles decays. This should lead to a better understanding of matter-antimatter asymmetry.

Three smaller experiments are installed in the caverns of the four bigger experiments. LHCf [35] measures the neutral particles produced in the direction of the beams. It provides calibration data for models used in the study of ultra high-energy cosmic rays. TOTEM [47] is designed to measure the total cross-section of the proton. Finally, MoEDAL [40] searches for new hypothetical particles such as magnetic monopoles or massive stable charged particles.

### 1.1.1 Main characteristics

In any accelerator, there are two main characteristics important for the physics :

- The center-of-mass energy (named  $\sqrt{s}$  according to the Mandelstam variables terminology) is the total amount of energy available in a collision. It is function of the energy  $E_i$  and the momentum  $\vec{p}_i$  of the two beams. As the LHC is a symmetric collider, the momentum are opposite ( $\vec{p}_1 = -\vec{p}_2$ ) and therefore the total energy is the sum of the energy of the two beams.

$$\sqrt{s} = \sqrt{(E_1 + E_2)^2 - (\vec{p}_1 + \vec{p}_2)^2} = E_1 + E_2$$

- The instantaneous luminosity is a function of the number of particles by bunch,  $n_i$ , the root mean squared (rms) transverse beam sizes,  $\sigma_x$  and  $\sigma_y$ , and the frequency of collision  $f$  [12]:

$$\mathcal{L}_{inst} = f \frac{n_1 n_2}{4\pi\sigma_x\sigma_y}$$

By integrating this instantaneous luminosity over time, one gets the total luminosity  $\mathcal{L}$  :

$$\mathcal{L} = \int_{t_1}^{t_2} \mathcal{L} dt$$

It is generally expressed in barn<sup>-1</sup> <sup>1</sup>. By definition that quantity is proportional to the expected number of events of a physical process of cross-section  $\sigma_{evt}$ :

$$N_{evt} = \mathcal{L}\sigma_{evt}$$

The LHC nominal center-of-mass energy is 14 TeV while its nominal instantaneous luminosity is  $10^{34} \text{ cm}^{-2}\text{s}^{-1}$ .

### 1.1.2 LHC Planning

Years after years the LHC is upgraded to improve its performances while replacing its aging parts. Both the center-of-mass energy and luminosity are increased to help in the discovery of new and rare physical processes.

One can see the past and future upgrades of the LHC on figure 1.2. The LHC first operated with a center-of-mass energy of 7 TeV and was progressively upgraded to currently reach 13 TeV. During the same time the instantaneous luminosity was also improved to reach  $2.06 \times 10^{34} \text{ cm}^{-2}\text{s}^{-1}$  or twice the designed value [41]. At the end of 2017, CMS had recorded an integrated luminosity of  $86.33 \text{ fb}^{-1}$  at 13 TeV [45].

The next big leap is what is called the High Luminosity-LHC (HL-LHC) or LHC Phase II [5]. While its center-of-mass energy will be limited to 14 TeV, the luminosity will peak at  $10 \times 10^{34} \text{ cm}^{-2}\text{s}^{-1}$ .

In order to prepare such a jump, a first Long Shutdown (LS2) of two years is planned at the end of this year. CMS will use this opportunity to perform the first phase of its upgrade. This is also when the GE1/1 detectors will be installed (see chapter 3 for more details).

The upgrade will be finalized during the Long Shutdown (LS3) between 2023 and 2026. At the end of the HL-LHC operation, the total integrated luminosity should reach  $3000 \text{ fb}^{-1}$ .

---

<sup>1</sup>1 barn =  $1 \times 10^{-24} \text{ cm}^2$



Figure 1.2 – The planned LHC long term calendar. It will lead to the commissioning of the HL-LHC, High Luminosity-LHC around 2025. [16]

## 1.2 The CMS experiment

CMS [21, 19] is one of the four big LHC experiments and one of the two general purpose detectors. It is shaped as a cylinder of 28.7 m of length and 15 m of diameter for a total weight of 14 000 tons. In order to optimally surround the interaction point, CMS is formed by a cylindrical barrel and two endcaps which close its ends.

### 1.2.1 System of coordinates

The CMS system of coordinates is centered on the collision point with the Y-axis pointing vertically, the X-axis pointing to the center of the LHC and the Z-axis pointing in the direction of the beams in a right handed way.

Due to the geometry of CMS, a cylindrical set of coordinates is more appropriate :  $\phi$  is the angle in the XY plane, R is the distance to the beam pipe and Z the distance along the beam pipe. However these coordinates do not present any Lorentz invariance. Therefore one of the coordinates (either R or Z) is replaced by the pseudo-rapidity [49]:

$$\eta = -\ln \frac{\theta}{2}$$

where  $\theta$  is the angle between the particle momentum,  $\vec{p}$  and the beam. This quantity has the nice property being a good approximation of the rapidity for highly relativistic particles :

$$\eta \approx y = \frac{1}{2} \ln \left( \frac{p + p_z}{p - p_z} \right)$$

The difference of pseudo-rapidity is therefore Lorentz invariant and the particle production is equally distributed in the coordinate. All these coordinates are illustrated figure 1.3.

### 1.2.2 Subdetectors

CMS is organized in multiple detection layers which have each a different objective. These detection layers are present both in the barrel of CMS and in the endcaps, but can use different technologies.

The figure 1.4 represents one octant of a slice of the CMS barrel. One can follow the path of a particle produced near the collision point, through the subdetectors [27, 19] :

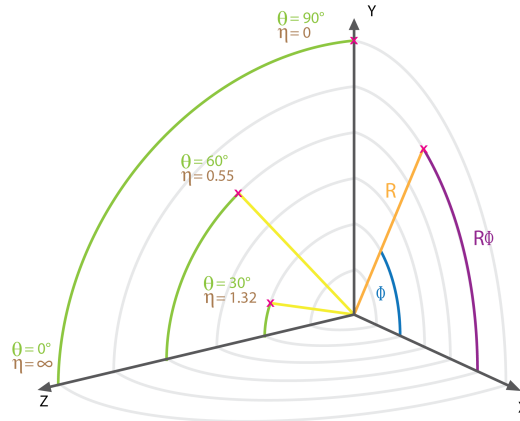


Figure 1.3 – CMS system of coordinates. The beam is along the Z axis. In green and brown, one can see the comparison between the  $\theta$  angle and the pseudo-rapidity  $\eta$ . [32]

- The tracker (in concentric black lines) is the first detector encountered by a produced particle. It reconstructs the trajectory of charged particles by measuring their crossing points with the detector. The momentum of the particles is extracted from the bending of the tracks and the production point is estimated from backward interpolation.

In CMS, the tracker is fully made of silicon detectors. The three inner layers are made of 64 million pixels ( $100\ \mu\text{m} \times 150\ \mu\text{m}$ ) while outer layers use 9.3 million strips (typical dimension of  $10\ \text{cm} \times 200\ \mu\text{m}$ ). This high granularity is required close to the interaction point to reduce the occupancy of the active cells. In addition, the pixels provides the spatial resolution needed to differentiate the secondary vertices.

The CMS tracker covers pseudo rapidities in the range  $|\eta| < 2.5$ . It achieves performances of 15 to 20  $\mu\text{m}$  in vertex reconstruction and  $\Delta p_T/p_T = 1\%$  at  $0.1\ \text{TeV}/c^2$  and 10% at  $10\ \text{TeV}/c^2$  in transverse momentum resolution.

- The Electromagnetic Calorimeter (ECAL, in green) measures the energy of photons and electrons by absorbing the particles.

The CMS ECAL is made of 75 848  $PbWO_4$  crystals which have a typical section of  $25\ \text{mm} \times 25\ \text{mm}$  for a typical length of 22 cm. They absorb the particles and produce low energy photons which are measured through photodetectors.

The barrel ECAL covers the range  $|\eta| < 1.479$  and has an energy resolution of  $\left(\frac{\sigma}{E}\right)^2 = \left(\frac{2.7\%}{\sqrt{E}}\right)^2 + \left(\frac{210}{E}\right)^2 + 0.55\%$ . For its part, the endcap ECALs cover the range  $1.479 < |\eta| < 3$  and have an energy resolution of  $\left(\frac{\sigma}{E}\right)^2 = \left(\frac{5.7\%}{\sqrt{E}}\right)^2 + \left(\frac{245}{E}\right)^2 + 0.55\%$ .

- The Hadronic Calorimeter (HCAL, in yellow) measures the energy of hadronic particles by absorbing them. At this distance from the interaction point ( $> 1.77\ \text{m}$ ), the particles are mainly neutrons, protons and pions.

In CMS, the HCAL is composed of layers of brass alternating with layers of scintillators. The typical thickness of brass layers is 50 mm.

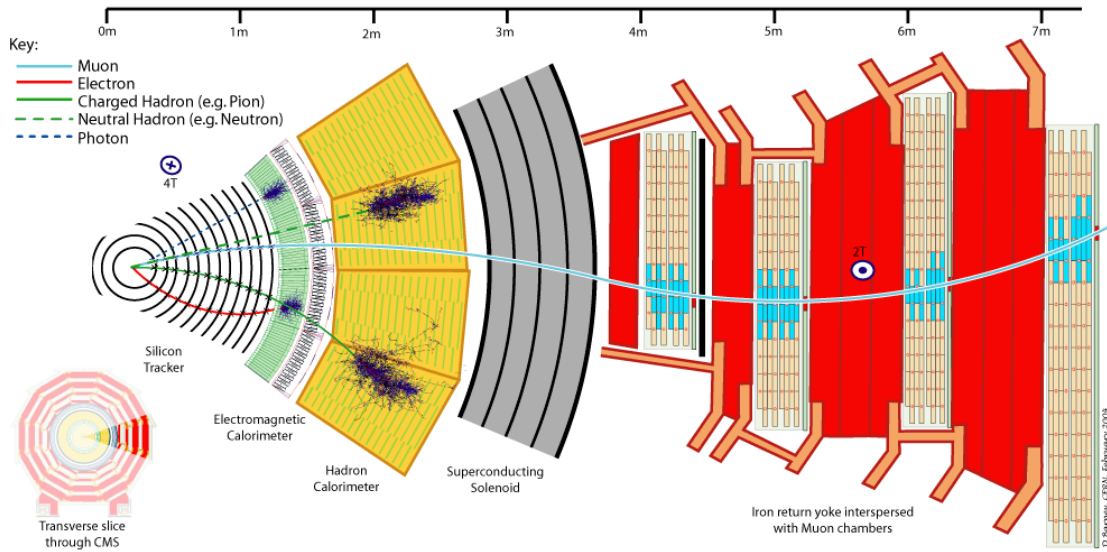


Figure 1.4 – Transverse view of one octant of the barrel of CMS. The lines represent the path of different particles through the different sub-detectors : the tracker in black, the ECAL in green, the HCAL in yellow and the muon system in orange. The solenoid is colored in grey. [30]

The CMS HCALs (barrel and endcap) cover the range  $|\eta| < 3$  and reach an energy resolution of  $\left(\frac{\sigma}{E}\right)^2 = \left(\frac{68\%}{\sqrt{E}}\right)^2 + 4.5\%$ .

- The solenoid (in grey) produces the magnetic field necessary to bend the charged particle trajectories. The precise measurement of the particle momentum relies on that curvature. The CMS solenoid produces a magnetic field of 3.8 T in its internal part, while the external magnetic field drops to 2 T.
- The muon detectors (in orange) are the outermost subdetectors. This subsystem is a tracker dedicated to the muons. The next section describe the muon subsystem in more details.

### 1.2.3 Muon subsystem

As the muons have a high penetrating power, there are multiples advantages for placing the muon subsystem in the outermost regions of CMS. The detectors have less space constraints compared to those included in the solenoid. While the surface to cover is larger, the rate of particles is lower so are the radiations. These characteristics make gaseous detectors ideal candidates. The solenoid and return yoke create a shielding which filters particles other than muons to produce a clean signal. The drawback of placing the muon detectors behind the return yokes is the degradation of the track positioning. Indeed, the muons may undergo multiple scattering and placing the detectors behind bigger amount of material will increase the deflection.

The current CMS experiment is composed of three technologies of gaseous detector as depicted on figure 1.5. The Drift Tubes (DT) are present only in the barrel while the Cathode Strip

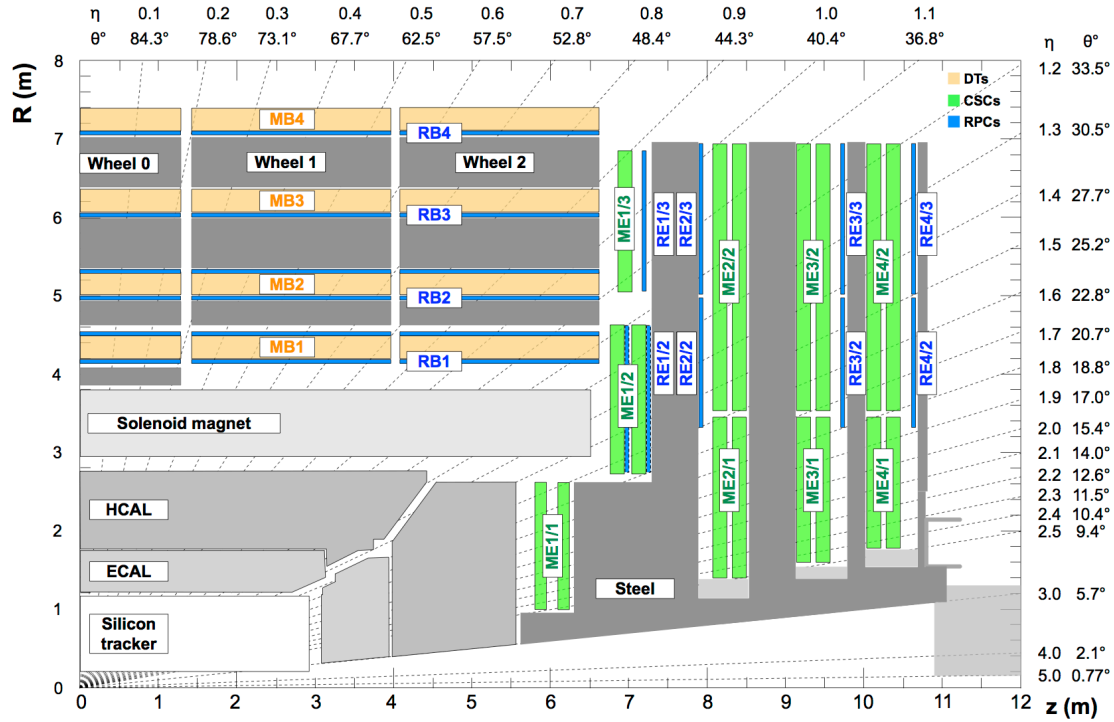


Figure 1.5 – Location of the different detectors used in the muon system. The collision point is in the bottom left corner. The DTs (in orange) are only present in the barrel. The CSCs (in green) are located only in the endcaps. The RPCs (in blue) are located both in the barrel and the endcaps. [46]

Chambers (CSC) are located in the endcaps. The Resistive Plate Chambers (RPC) are present both in the barrel and the endcap. All these chambers are slotted between the return yokes made of steel.

The DTs and the CSCs provide a good spatial resolution ( $\sim 100 \mu\text{m}$ ) in order to recover the momentum of the muons. For their part, the RPCs have a lower spatial resolution ( $\sim 1 \text{ mm}$ ), but they are fast and have a very good time resolution ( $\sim 1 \text{ ns}$ ). As the muons subsystem is an essential part of the trigger by the clean signature muons provide, the good time resolution is a significant advantage. Moreover the double technology provides a redundancy to avoid false positive triggers [3].

A more detailed explanations of these technologies will be given in section 2.3.

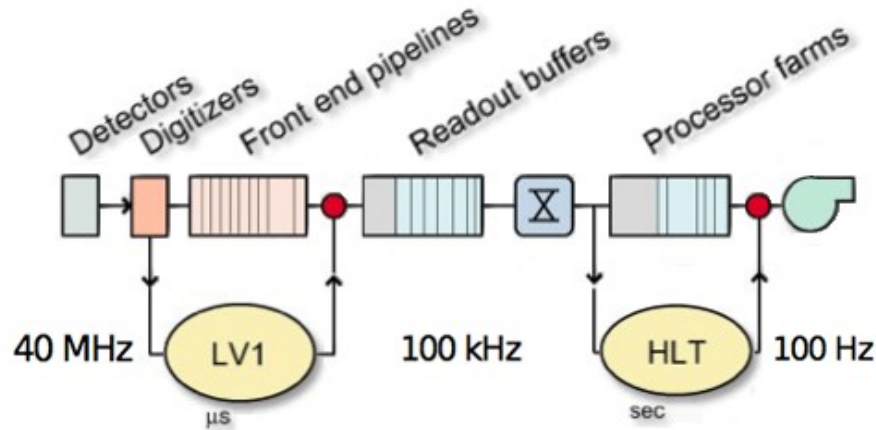


Figure 1.6 – Overview of the CMS trigger system. The yellow bubbles represent the two levels of trigger processing. They successively select the events to a rate that can be stored.

#### 1.2.4 Trigger system

At CMS interaction point, a collision between bunches occurs every 25 ns. The data generated for each collision has an average size of 1MB. Processing and storing every event is so unpractical but also useless as interesting physical processes are not present in every bunch crossing (BX).

The trigger system is in charge of selecting the events of interest before their storage. CMS has chosen a trigger system with two levels as represented figure 1.6 :

- The Level 1 (L1) trigger must reduce the data rate from 40 MHz to a maximum of 100 kHz. To achieve this goal, it receives the trigger data, a coarse grained dataset, from the calorimeters and the muon subsystem. During this decision process, the complete data remains stored in pipeline memories on the frontend electronics. This is the reason why the L1 trigger must issue a decision every 25 ns with a maximum latency of 3.2 μs. Such constraints require an hardware implementation.

Once an event is selected by the L1 trigger, the L1 accept signal (L1A) is sent to all the detector. The complete dataset, called the tracking data, is then routed to the High Level Trigger (HLT).

- At the HLT, the event rate reduction allows longer processing time of up to  $\sim 1$  ms. The HLT can so use more advanced algorithms on the full grained data as well as the tracker informations. This part of the trigger is composed of a computer farm. At the end of the process, the event rate is reduced to a few hundreds of Hz and the data are stored on disk for future offline analysis.

### 1.2.5 Upgrade

Before the start of the HL-LHC, CMS, as well as the other detectors at the LHC, must be upgraded [29]. Indeed, the number of collisions during a bunch crossing (pileup) is proportional to the instantaneous luminosity and while it was of 53 on average at the highest LHC luminosity it could increase to 200 with the HL-LHC. One consequence of the increase of luminosity, and so pileup, is the surge of the radiation levels. The new detectors and their electronics (particularly close to the interaction point) will need to cope with these new radiation levels.

The increase of pileup will also increase the particle rate. This means that the detectors must be able to measure these particles and the trigger must correctly discriminate the events.

While some of the detectors technologies of CMS can sustain the new rate of particles, others such as the tracker will need to be replaced. In that innermost region, the granularity needs to be improved.

To maintain its efficiency, the trigger will also be improved. The new L1 trigger will increase the acceptance rate from 100 kHz to 750 kHz while improving its discrimination power. To achieve this goal two enhancements are planned : (1) the L1 trigger will use informations from the tracker. (2) Its latency will increase from 3.2  $\mu$ s to 12.5  $\mu$ s. Because of the modifications in latency and trigger rate, all the electronics will have to be replaced.

From what is said before, the minimal upgrade for all the subdetectors is the replacement of the electronics. However, some detectors need to be fully replaced with a more appropriate technology. Moreover, new detectors will be added.

Here is a brief summary of the upgrades planned for LHC Phase II [27]:

- The tracker must be completely replaced to resist the new radiation levels. The new particle rate imposes that the granularity is multiplied by a factor  $\sim 4$  and the new trigger will require informations on the momentum of the particles.
- The barrel ECAL will be equipped with a new front-end board to cope with the higher radiation levels and data rate. The crystals can still be used but will be cooled at a lower temperature.
- The barrel HCAL will be equipped with new electronics and new sensor tiles to improve the granularity and the radiation tolerance. The innermost brass tiles will also be replaced by new ones.
- The endcap calorimeters will be totally replaced by a calorimeter integrating the ECAL and HCAL functions. This new calorimeter is called the High Granularity Calorimeter (HGCal) [38] and provides a granularity of roughly  $1 \text{ cm}^2$ . It is based on alternating layers of stainless steel and silicon sensors or scintillators.
- The actual muons chamber should be able to cope with the increased rate of particles. However, all its electronics will be replaced with a more radiation hard one.
- In parallel, the muon system will be enhanced through the use of glass-RPCs (iRPCs) and triple-GEM detectors in the endcaps as detailed in chapter 3. This upgrade will ensure to maintain the efficiency of the L1 trigger while improving the track reconstruction as well as increasing the redundancy in the most forward region.



## Chapter 2

# Gaseous detectors

Gaseous detectors are widely used in High Energy Physics (HEP) thanks to their multiple advantages. Two of these are :

- Gaseous detectors are relatively cheap (compared to silicon detectors for example) which makes them interesting to cover large areas.
- Gases have lower densities which reduce the multiple scattering and the energy losses when a particle crosses them.

In this chapter, we review the working principles of gaseous detectors focusing on the parameters relevant for the time resolution, that is ionization of the gas mixture and drift velocity. [26, 10]. We then briefly present the different technologies used within the CMS experiment. The next section is dedicated to the detailed description of the triple-GEM detectors. This chapter ends with a discussion about the intrinsic time resolution of a gaseous detector.

### 2.1 Energy losses in medium

While particles travel through matter, they undergo multiple interactions with its constituents. In the case of charged particles these interactions can be : Coulomb interactions, bremsstrahlung, Cerenkov effect, ... Energy is lost within these interactions and particles are scattered.

For the particles we are interested in, the muons, the dominant interaction is the Coulomb interaction. In this case, the Bethe-Bloch formula describes the mean loss of energy of a particle in a medium [12] :

$$-\left\langle \frac{dE}{dx} \right\rangle = K z^2 \frac{Z}{A} \frac{1}{\beta^2} \left[ \frac{1}{2} \ln \frac{2m_e c^2 \beta^2 \gamma^2 T_{max}}{I^2} - \beta^2 - \frac{\delta(\beta\gamma)}{2} \right]$$
$$K = 4\pi N_A r_e^2 m_e c^2$$

where  $N_A$  is the Avogadro's number,  $r_e$  the classical electron radius,  $m_e$  the electron mass at rest,  $z$  the charge of the incident particle,  $Z$  and  $A$  the atomic number and the atomic mass of the medium and  $T_{max}$ , the maximum energy transfer in one collision <sup>1</sup>.  $I$  is defined as the mean excitation energy of the medium while  $\delta(\beta\gamma)$  is the density effect correction. The equation is valid for  $0.1 \lesssim \beta\gamma \lesssim 1000$ .

---

<sup>1</sup> $T_{max} = \frac{2m_e c^2 \beta^2 \gamma^2}{1+2\gamma_e/M+(m_e/M)^2}$  where  $M$  is the mass of the incident particle.

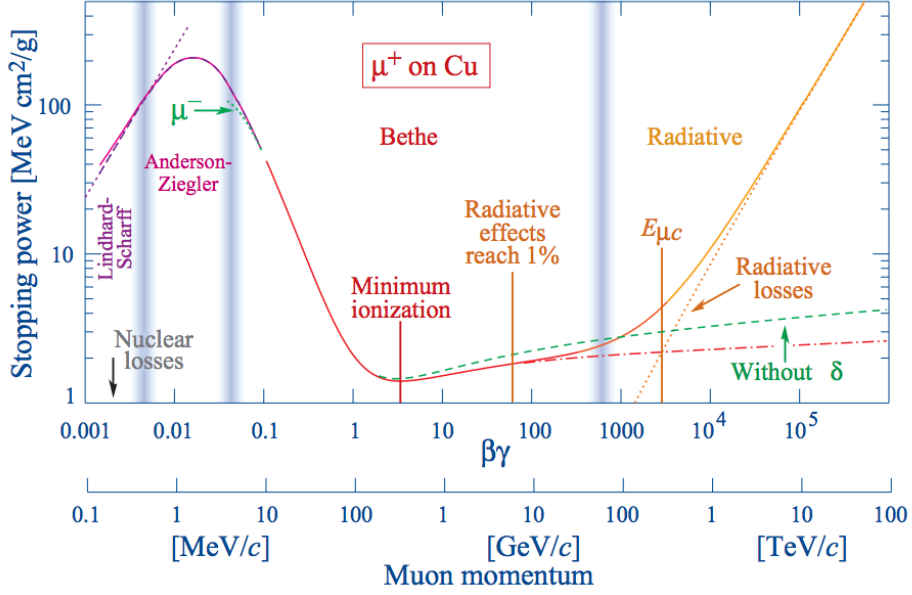


Figure 2.1 – The energy loss of a  $\mu^+$  in Cu. The Bethe-Bloch formula is represented in red. [12]

The figure 2.1 represents the energy loss normalized by material density for muons going through copper. The Bethe-Bloch equation is drawn in red.

At lower energies the particle velocity becomes comparable to atomic electron velocity while at higher energies the radiative loss becomes the dominant process, both increasing the total energy loss. In the range of validity of the Bethe-Bloch equation, one can spot the minimum ionizing energy around  $\beta\gamma \sim 3$ . In HEP experiments, the particles of interest are above that threshold and are called Minimum Ionizing Particles (MIP).

It is important to note that this formula only gives the mean energy loss. Indeed, the interaction process is an ionization of the medium by the traversing particles. For each ionization, a localized group of electrons, called a cluster, is deposited in the medium. This stochastic energy loss process is strongly asymmetric and is described by a Landau distribution.

For thin absorbers (with  $\Delta E \ll T_{max}$ ), the actual energy loss has so strong variations from one particle to another.

## 2.2 Gaseous detectors

### 2.2.1 Total ionization

The electrons ejected by the ionizing particle are called primary electrons,  $n_p$ . Some of these electrons can possess enough kinetic energy to ionize new atoms and free new electrons, called secondary electrons. The group of electrons gathered around a primary ionization is called a cluster.

The sum of the primary and secondary electrons forms the total ionization,  $n_{tot}$ . It can be computed by dividing the mean energy loss of the particle by the mean ionization energy of the

Gas	$n_p$ [cm <sup>-1</sup> ]	$W_I$ [eV]
Ar	25	26
CO <sub>2</sub>	35	34
CH <sub>4</sub>	28	30

Table 2.1 – Primary ionization  $n_p$  and average energy per ion pair  $W_I$  for the gases used in the triple-GEM detector. [12]

medium,  $W_I$ . This experimental parameter takes into account the energy losses unrelated to the ionization as well as the energy used for the ionization.

The number of primary electrons and the average ionization potential for the gases used in the CMS triple-GEM detector are listed in table 2.1.

The intrinsic efficiency of a gaseous detector is directly related to the number of primary electrons. Indeed, the probability that a particle produces  $k$  primary ionizations while traversing a medium is dictated by a Poisson law with  $n_p$  as mean :

$$P(k) = \frac{n_p^k}{k!} e^{-n_p} \quad (2.1)$$

The intrinsic inefficiency is the probability that a particle does not produce any primary ionization while traversing the medium :

$$\text{inef} = P(0) = e^{-n_p} \quad (2.2)$$

The required efficiency constrains the choice of the gas. As the noble gases usually have a lower ionization energy, they are the primary choice.

### 2.2.2 Amplification

The typical total ionization is about a few 100s  $e^-$  (for example 97  $e^-$  are produced in average in 1 cm of argon for a MIP) while an electronic amplifier has typically a noise around 1000  $e^-$ . If the signal was only amplified electronically, it would totally be masked by the noise. So, gaseous detectors amplify the signal by using an avalanche process.

A strong electric field (several tens of kV/cm) is produced in the gaseous detector chambers to accelerate the electrons. Once they have gained enough kinetic energy, they ionize the medium in turn. This process is repeated for each newly produced electron, creating an exponential growth of the avalanche.

Figure 2.2 details the formation of an avalanche around an anode wire. On figures (a), (b) and (c) we can see the electrons moving toward the anode while the ions are drifting to the cathode. During the drift, electrons gain enough energy to free new electrons and develop the avalanche process. This process stops when the internal electric field compensates the external field.

The figure (d) show the avalanche totally surrounding the anode wire. On figure (e) the electrons have been collected and the ions are slowly moving toward the cathode. In this geometry, the ions generate most of the measured signal.

The gain of the avalanche, also called the gas gain, is defined as :

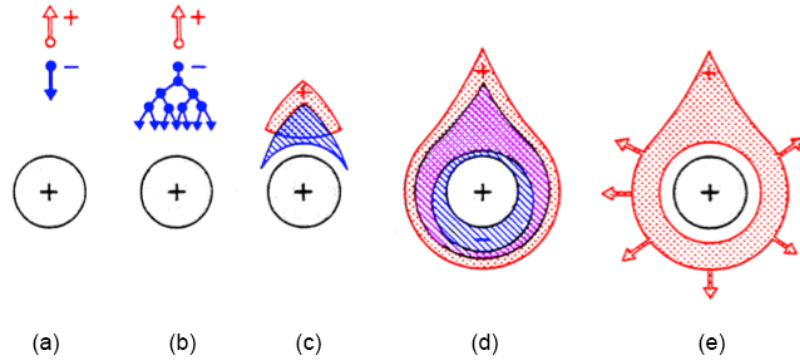


Figure 2.2 – Formation of an avalanche around an anode wire. [43]

$$A = \frac{N}{N_0}$$

where  $N$  is the final number of electrons while  $N_0$  is the total number of electrons at the start of the avalanche.

$N$  depends of the distance travelled by the electrons,  $D$ , and the first Townsend coefficient,  $\alpha(x)$ . The first Townsend coefficient is an empiric parameter which has to be measured for each gas mixture. The variation of the number of electrons along a path is given by :

$$dN = N\alpha(x)dx$$

Its integration along a path gives the following relation :

$$N = N_0 \exp\left(\int_0^D \alpha(x)dx\right)$$

Even if  $\alpha(x)$  cannot be predicted, certain tendencies appear. Noble gases have a larger Townsend coefficient than more complex gases. Indeed, they have less degrees of freedom that can absorb energy.

However, the noble gases can emit photons by the recombination of electrons and ions with an energy high enough to ionize an other atom. This radiation must be absorbed by more complex gas called a quencher. This quencher prevents the formation of sustained avalanches which could damage the detector.

### 2.2.3 Drift

The drift speed of the electrons and positive ions has an important impact on the time resolution.

The drift velocity can be derived from the Maxwell-Boltzmann distribution :

$$\langle \epsilon \rangle = \frac{1}{2}m\langle v^2 \rangle = \frac{3}{2}kT$$

In presence of an electric and a magnetic field, the drift velocity is :

$$v_{drift} = \frac{\mu}{1 + \omega^2\tau^2} \left( \vec{E} + \frac{\vec{E} \times \vec{B}}{B} \omega\tau + \frac{(\vec{E} \cdot \vec{B}) \cdot \vec{B}}{B^2} \omega^2\tau^2 \right)$$

where  $\mu = \frac{e\tau}{m}$  is the particle mobility,  $\omega = \frac{eB}{m}$  is the cyclotron frequency and  $\tau$  is the average time between collisions. [26].

One can notice that the velocity is proportional to the electric field and the mobility. Henceforth the lighter the drifting particle is, the faster it is, as expected.

$\tau$  is function of the electron energy and cannot be computed. It has to be experimentally measured for each gas mixture.

In section 2.5, we will see that we need to choose a fast gas to reach a good time resolution.

## 2.3 Technologies currently used in CMS

Multiple gaseous detectors geometries and technologies have been developed to improve their characteristics :

- Increase the spatial resolution thanks to a higher granularity.
- Increase the time resolution by having faster avalanches.
- Improve the counting rate by collecting the positives ions faster.
- Increasing the gain to improve the efficiency.
- Reducing the risk of discharge.

As said in section 1.2.3, CMS currently uses three different technologies of gaseous detectors : the Drift Tubes (DT), the Cathode Strip Chambers (CSC) and the Resistive Plate Chambers (RPC).

### 2.3.1 The drift tubes

The Drift Tubes (DT) are tubes of section  $13 \text{ mm} \times 42 \text{ mm}$  for a length of 2.4 m. The anode is composed of a single wire stretched in the chamber length while the cathode is composed of two strips on two sides of the chamber as represented in the figure 2.3. The tube is filled with a gas mixture of 85%Ar and 15%CO<sub>2</sub>. The electric field of 1.5 kV/cm allows for a gas gain of  $10^5$ . The same electric field, flattened thanks to the top and bottom electrodes, produce the avalanche near the anode wire and limits the drift time to 380 ns.

In the CMS barrel, four layers of tubes are stacked with an offset of half a cell to form what is called a superlayer. Three (or two) superlayers are then assembled to form one DT chamber. In the three superlayers version, one of them is orthogonal to the two others to measure the Z coordinate.

The long deadtime associated to the size of the tubes limits the use of the DTs for low particle rate regions such as in the CMS barrel ( $\sim 10 \text{ Hz/cm}$ ). One chamber reaches a spatial resolution of  $100 \mu\text{m}$  for a time resolution of 5 ns.

### 2.3.2 The cathode strips chamber

The Cathode Strips Chambers (CSC) are multiwire proportional chambers optimized for the endcaps of CMS. They are composed of 6 layers of anode wires and 7 layers of cathodes strips (see figure 2.4a). The nominal gas mixture is 40%Ar + 50%CO<sub>2</sub> + 10%CF<sub>4</sub> allows for a gas gain of  $7 \times 10^4$  with an electric field of up to 3.9 kV/cm.

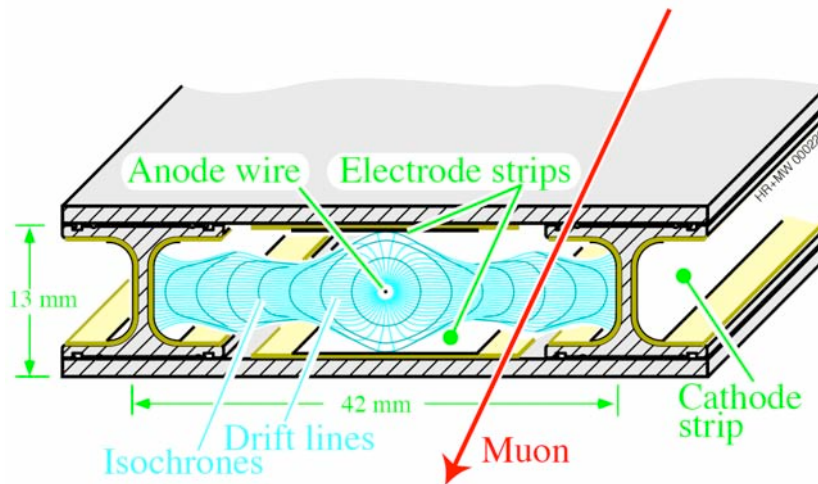


Figure 2.3 – Schematic of a drift tube. The cathode is formed by strips along the side of the tube whereas the anode is a wire stretched in the middle of the tube. [19]

One layer of anode contains about 1000 wires spaced by 3.2 mm. Each layer of cathode is made of about 80 strips orthogonal to the anode wire. The readout on both the anode and the cathode enables the extraction of the 2 coordinates (see figure 2.4b).

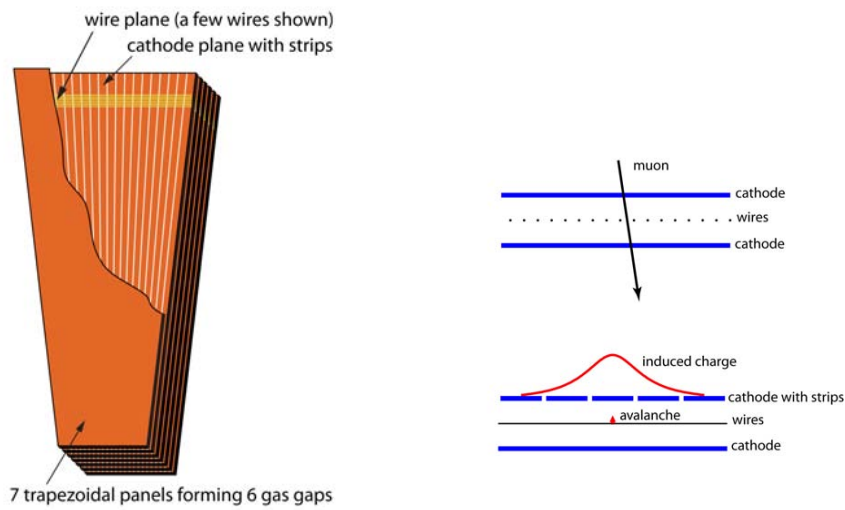
CSC are used in the endcaps where the particles rate can be as high as ( $\sim 1 \text{ kHz/cm}^2$ ). The reached spatial resolution can be as good as  $75 \mu\text{m}$ , depending on the position, with a time resolution of 5 ns.

### 2.3.3 The resistive plate chamber

[p] The Resistive Plate Chambers (RPC) are gaseous parallel-plate detectors having an excellent time resolution. Their main purpose in CMS is to unambiguously associate an event to the right bunch crossing.

Figure 2.5 represents the section of a 2 gaps RPC detector filled with a mixture of 96.2%  $\text{C}_2\text{H}_2\text{F}_4$ , 3.5%  $\text{iC}_4\text{H}_{10}$  and 0.3%  $\text{SF}_6$ . It consists of two chambers made of parallel electrodes coated with graphite and separated by only a few millimeters. The readout electrodes are protected by a resistive plate made of bakelite.

The very good time resolution of the RPCs is achieved by producing faster avalanches than the previous two detectors in smaller gaps. As a result, the time resolution is as small as 1 ns at the expense of a spatial resolution of 1 mm. To cope with the particle rate of the endcaps, the RPCs must be able to run at  $1 \text{ kHz/cm}^2$ .



(a) Geometry of a CSC chamber. The anode wires are stretched radially. The second coordinate is read by the cathode strips.

(b) Diagram explaining the 2D read-out process. Charge, induced of both the anode and the cathode, is read by in two perpendicular directions.

Figure 2.4 – Details of the CSCs. [19]

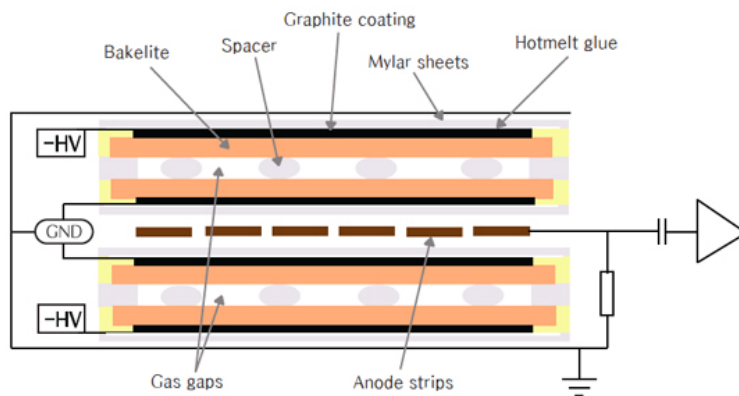


Figure 2.5 – Sectional view of a 2 gaps RPC detector. The readout strips (in brown) are sandwiched by the two gas volumes. The bakelite plates which protect the electrodes are colored in orange. [28]

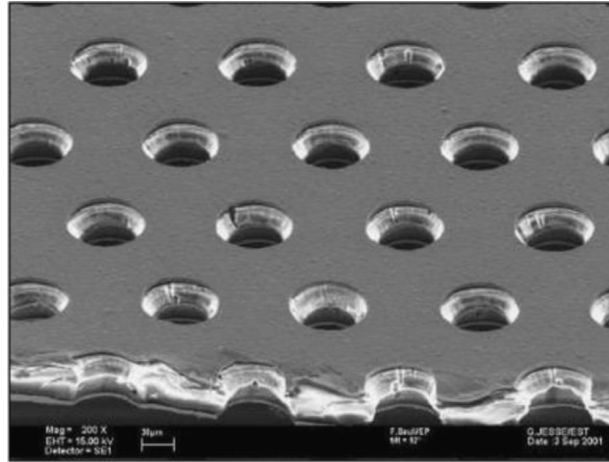


Figure 2.6 – Electron microscope picture of a GEM foil. The holes have a typical inner diameter of  $50\ \mu\text{m}$ , outer diameter of  $70\ \mu\text{m}$  with a pitch of  $140\ \mu\text{m}$ . [44]

## 2.4 Triple-GEM detectors

Gas Electron Multiplier (GEM) detectors were invented in 1997 at the CERN.

One GEM foil is composed of a foil of Kapton insulator, thick of  $50\ \mu\text{m}$ , coated with a  $5\ \mu\text{m}$  copper layer on each side. Photolithography processes are used to dig small regularly spaced holes in the foil. These holes have a typical inner diameter of  $50\ \mu\text{m}$ , outer diameter of  $70\ \mu\text{m}$  with a pitch of  $140\ \mu\text{m}$ . An electron microscope picture of a GEM foil is presented figure 2.6.

By applying a potential difference between the two sides of the GEM foil, one creates an electric field whose intensity is maximal within the holes. For foils of small size ( $\sim 10\ \text{cm} \times 10\ \text{cm}$ ) manufactured with a good quality, the field within the holes can reach hundreds of  $\text{kV}/\text{cm}$  for gas gains of  $10^3$ . The figure 2.7 shows some electric field lines around a GEM foil in red. In the picture, the GEM foil is enclosed between an anode and a cathode.

The space between the cathode and the GEM foil, called the drift gap, is where the primary and secondary ionizations take place. The electric field then guides the electrons to the foil where the amplification takes place. The gap between the GEM foil and the anode, where the readout electrodes are located, is called the induction gap.

An important characteristic of the GEM detectors is the speed of charge collection and signal formation. One can see on the figure 2.7, the electrons (in blue) and the ions (in red) drift paths.

As the signal is formed by the electrons, it is so faster than if it was formed by the ions (see section 2.2.3). This allows a better time resolution as we will see in the section 2.5. In addition, a large fraction of the ions are quickly collected by the ion trap of the top of the GEM foil. The quick collection of ions reduces the deadtime of the detector and hence increases its rate capability.

The high gain required for experiments would imply a very high voltage across the GEM foil. The problem raised with high voltages is the risk of discharges which would damage or destroy the detector and its electronics. In order to achieve these high gain while keeping the voltage sustainable, multiple GEM foils are stacked.

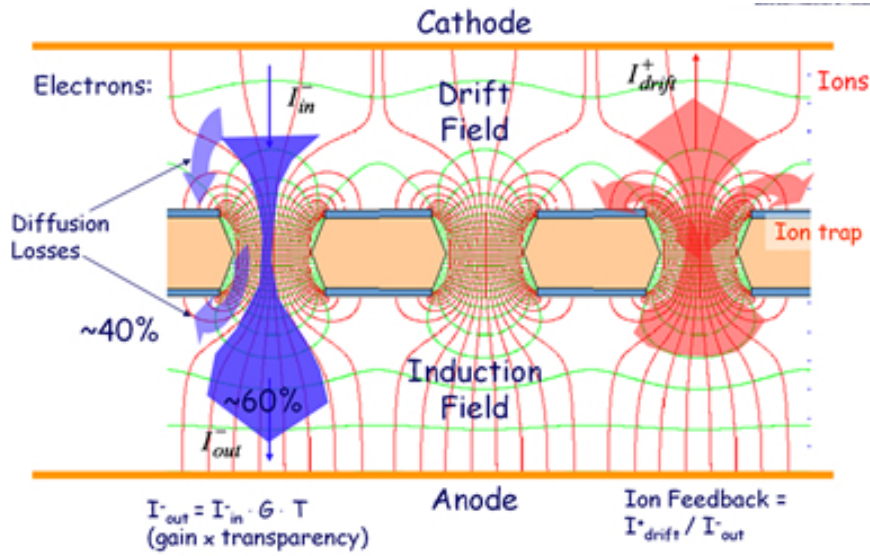


Figure 2.7 – Schematic of a GEM foil enclosure between a cathode and an anode. The electric field lines are colored in red. The drift paths of the electrons and the ions are represented in blue and in red respectively. [48]

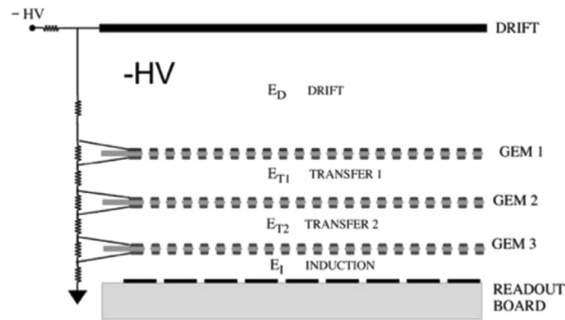


Figure 2.8 – Disposition of the three foils in a Triple-GEM detector. The multiple voltages are derived from a single high voltage (HV) source through a resistor divider. [44]

The triple-GEM detector is the use of three GEM foils separated by gas gaps, called transfer gaps. The figure 2.8 shows the configuration of the triple-GEM which will be used in CMS. The ionization takes place in the drift zone (3 mm thick) and is amplified by the first GEM foil. Between the 2 other GEM foils, the transfers gaps (2 and 1 mm) drive the electrons between the foils. The last gap (1 mm) is called the induction gap and guides the electrons to the anodes.

This geometry brings the right tradeoff between efficiency, spatial resolution, time resolution and discharge reduction. Section 3.1 describes in more details the dimensions of a full triple-GEM chamber for CMS.

## 2.5 Factors affecting the time resolution

The intrinsic time resolution of a gaseous detector depends on the gas mixture used and on the geometry of the detector.

The signal is formed by the successive electron avalanches produced by the multiple clusters created in the drift gap. Supposing that the cluster closest from the first electrode can create a strong enough signal, its drift time will determine the minimal time uncertainty.

The probability of creating the  $i$ -th cluster at distance  $x$  from the first GEM foil is given by :

$$P_n(i - th; x < X < x + dx) = P_n(i - 1; 0 < X < x) \cdot P_n(1; x < X < x + dx)$$

where  $n$  is the number of primary electrons. We know that the electrons are produced with a Poissonian probability (see equation 2.1) :

$$P_n(i - th; x < X < x + dx) = \frac{(nx)^{i-1}}{(j-1)!} e^{-nx} \cdot ndxe^{-ndx}$$

And so the distribution of the  $i$ -th cluster at distance  $x$  from the first GEM foil is given by :

$$p_n(i - th, x) = \frac{x^{i-1}}{(i-1)!} n^i e^{-nx}$$

We are interested in the position of the first cluster and more specifically by its drift time  $t_d = xv_d$  :

$$p_n(t_d) = nv_d \exp(-nv_d t_d)$$

Therefore the intrinsic time resolution is  $(nv_d)^{-1}$  [3]. It is immediate from this relation that a fast gas producing an high number of primary ionization improves the time resolution. As seen in section 2.2.3, increasing the electric field will also improve the time resolution.

This quick derivation assumes that the first cluster is always amplified and measured by the detector. In a real detector, a cluster could not be amplified or not amplified enough, this is called the transparency of the GEM foil. In this case, the second or even third, etc. cluster will produce the signal. This is the reason why the transparency plays an important role in the time resolution.

In addition to the intrinsic time resolution, the statistical nature of the processes in play in a gaseous detector can negatively impact the global time resolution. Indeed, the number and size of the clusters, the gain of the GEM foils and the transparency of the GEM foils create statistical variation in the amplitude of the induced signal for muons of the same energy.

When using a simple threshold discriminator, this amplitude fluctuation will create fluctuations in the time at which the threshold is crossed. This phenomenon, called time-walk, so degrades the measured time resolution of the detector (see section 3.4.1). By using a Constant Fraction Discriminator (CFD), the time-walk can be suppressed assuming that all signals have the same shape (see section 5.5.2).

More precise simulations have been made in [37] and confirm the influence of the parameters.

## Chapter 3

# The GE1/1 project

As explained in the section 1.2.5, the CMS muon subsystem needs to be upgraded to cope with the increased rate of particles that will be produced by the HL-LHC. The aim of the muon subsystem upgrade is to maintain the efficiency of the L1 muon trigger while improving the muon track reconstruction as well as increasing the redundancy in the most forward region. The new detectors will also need to be more radiation tolerant. To achieve these goals, new detectors will be added and the electronics of the existing detectors will be replaced by more recent and radiation tolerant technologies.

The new detectors will be slided in the area left vacant for the innermost layer of RPC detectors in the muon endcap. The installation of the RPCs was first staged for financial reasons at the start of the LHC, then it became clear that the standard RPCs could not sustain the particle rate ( $> 1 \text{ kHz/cm}^2$ ) in this region during HL-LHC. Consequently, alternatives were proposed like the glass-RPC (iRPC) and the GEM detectors. These technologies are shown in dark blue and in red respectively in figure 3.1 which represents the longitudinal view of one quadrant of the CMS detector.

This work focuses on the GE1/1 layer, the innermost layer of the first endcap disk that will be the first equipped with triple-GEM detectors.

After a quick overview, we explain the geometry of the GE1/1 project. We then detail the readout electronic which will be installed in CMS. The development electronics used in this master thesis is then explained along with a summary of its evolution.

### 3.1 Overview

In order to meet the physics objectives, the detector in this region of CMS should fulfill the following requirements :

**Geometry** The complete detector should not let any "blind" spots in its zone. Moreover, the maximum thickness for the new chambers is only 10 cm, the space left by the RPCs.

**Detection rate** Within the HL-LHC, the maximum hit rate is expected to reach  $5 \text{ kHz/cm}^2$ . With a safety factor of 2, the required rate capability must be  $10 \text{ kHz/cm}^2$  or better.

**Efficiency** An efficiency of 99.9% or more must be reached. A double layer of detection allows a minimum efficiency of 97% per chamber.

**Angular resolution** The angular resolution should be better than of  $300 \mu\text{rad}$  in  $\phi$  to reliably discriminate between low- $p_T$  and high- $p_T$  muons.

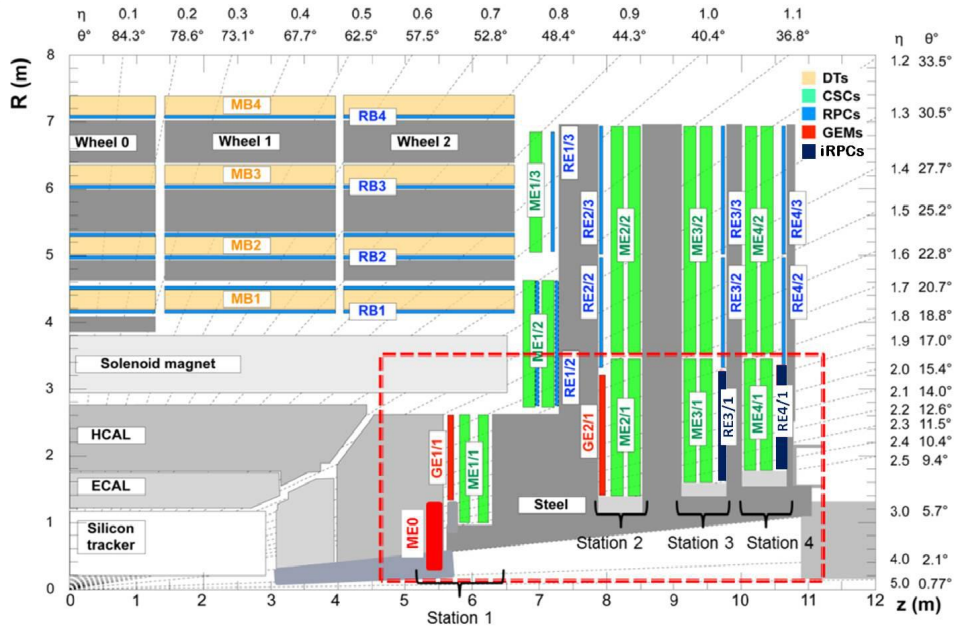


Figure 3.1 – Location of the detectors used in the muon system after upgrade for LHC Phase II. The triple-GEM based detectors are colored in red. [2]

**Timing resolution** A timing resolution better than 10 ns must be reached to provide a reliable trigger.

**Gain uniformity** The gain uniformity in the gaseous detectors must be 15% or better within a chamber as well as between the chambers.

**Radiation tolerance** The detector is expected to received an integrated charge of 100 mC/cm<sup>2</sup> after 20 years of operation in the HL-LHC. With a safety factor of 2, the detector must not suffer from any gain loss or other losses in response after 200 mC/cm<sup>2</sup> of integrated charge.

COMPASS, TOTEM and LHCb already use medium size (30x30 cm<sup>2</sup>) triple-GEM detectors with the required performances. These encouraging results showed that the technology could be used in the CMS muon subsystem. However, it was not clear at that time if building such large triple-GEM (1 m of length) was possible while meeting all these constraints.

After more than 5 years of R&D, CMS has shown that it was feasible. [thierry\_maerschalk\_study\_2016, 20, 27].

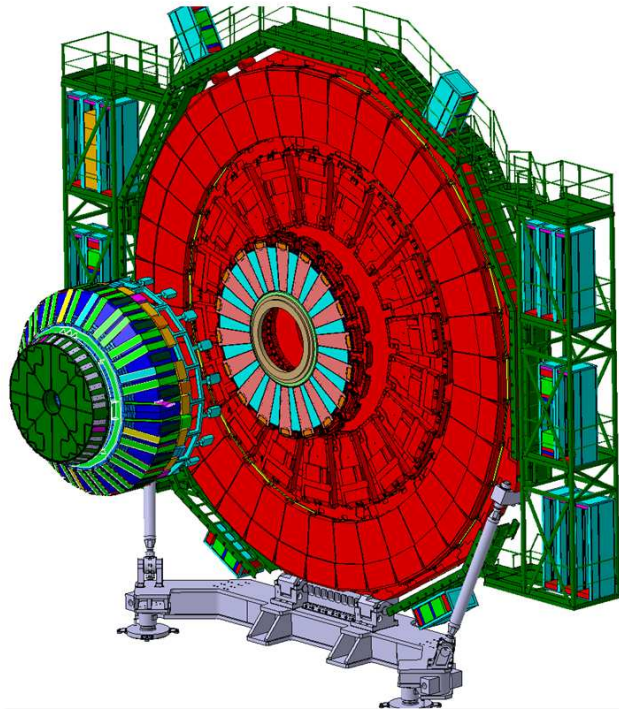


Figure 3.2 – The CMS endcap. The GE1/1 superchambers are highlighted in light red and cyan. [1]

### 3.2 GE1/1 chamber

The figure 3.2 shows a 3D drawing of the first disk of the CMS endcap. The GE1/1 superchambers are highlighted in light red and cyan. The 36 superchambers are trapezoidal sectors covering  $10^\circ$  in  $\phi$ . They are made from two triple-GEM chambers assembled back-to-back. That is, 144 chambers are required to complete the GE1/1 project.

The use of 2 chambers back-to-back allows an overall efficiency better than 99.9% for the L1 trigger by combining the two chambers with a logical OR.

The chambers are the elementary unit of the GE1/1 detector. Geometrical constraints require the use of alternating short and long versions to maximally cover the endcap. The small side of the trapeze is always 28.5 cm wide while the larger side is 48.4 cm (51.0 cm) wide and the length is of 113.5 cm (128.3 cm) for the short (long) version.

On figure 3.3, one can see an exploded view of one GE1/1 chamber. We can recognize the triple-GEM structure on the bottom : the drift electrode in light red, the GEM foils in cyan and the readout board in blue. The readout electronics is composed of (from bottom to top) : the VFAT3 chips in grey, the GEM Electronic Board (GEB) in red and the opto-hybrid (OH) in light brown. Those are detailed in the next section.

The readout board (in blue) is divided in 24 sectors : 3 along  $\phi$  and 8 along  $\eta$ . Each sector is further divided in 128 strips along its width for a total of 3072 strips per chamber. The chosen division ensures the required angular resolution of  $300 \mu\text{rad}$ .

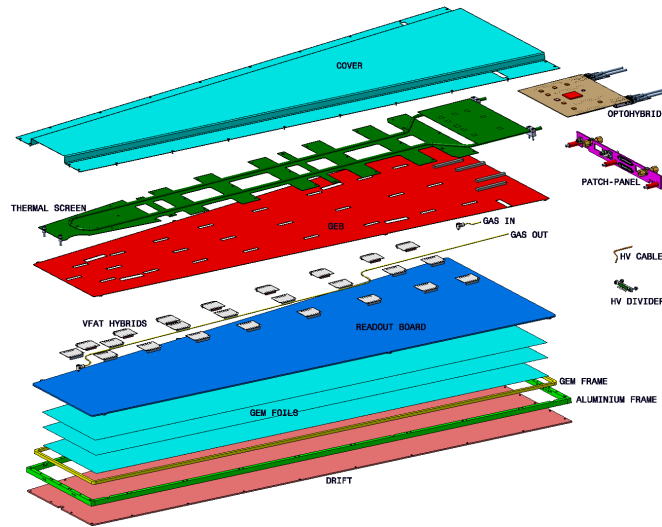


Figure 3.3 – Exploded view of a GE1/1 chamber. [1]

### 3.3 Readout electronics

The readout electronics overview can be seen on figure 3.4. It is composed of one front-end chip, called the VFAT3, for each sector of the readout board. The GEB ensures the connection between the VFAT3s and the opto-hybrid (in blue). The OH communicates to the off-detector electronics through 5 optical fibers : 4 to the GE1/1 backend electronics located inside the CMS Underground Service Cavern (USC) and 1 to the CSC trigger electronics (CSC TMB) located in the CMS balcony.

#### 3.3.1 The VFAT3

The VFAT3 [7] is the front-end ASIC used in the GE1/1 project. It is a 128 channels binary chip, each channel being connected to one detector anode strip. Each channel consists of one preamplifier, a shaper and a Constant Fraction Discriminator (CFD) which digitizes the signal. The binary signals are then synchronized with the LHC clock and duplicated in two path : the trigger path and the tracking data path.

**The trigger data path** The trigger data will be used by the L1 trigger. As explained in section 1.2.4, coarse granularity data are required to reach a low and fixed latency at L1. In the GE1/1, the VFAT3 chip is configured to make a logical OR of two adjacent channels. Those signals are transmitted on 8-bit wide bus along the GEB to the opto-hybrid at the frequency of 320 MHz using Time-Division Multiplexing (TDM). The VFAT3 trigger data are referred as S-bits.

**The tracking data path** The tracking data path is more complex. At each clock cycle, the full granularity data are stored within the SRAM1. This RAM is able to store events during 12.8  $\mu$ s before dumping them. This is the time that the L1 trigger has to accept an event at the HL-LHC. Once the VFAT3 is notified, the data corresponding to the event are stored within the SRAM2 along with the Bunch Crossing Number (BCN) and the Event Counter (EC). The BCN is a counter increased at each clock cycle while the EC is a

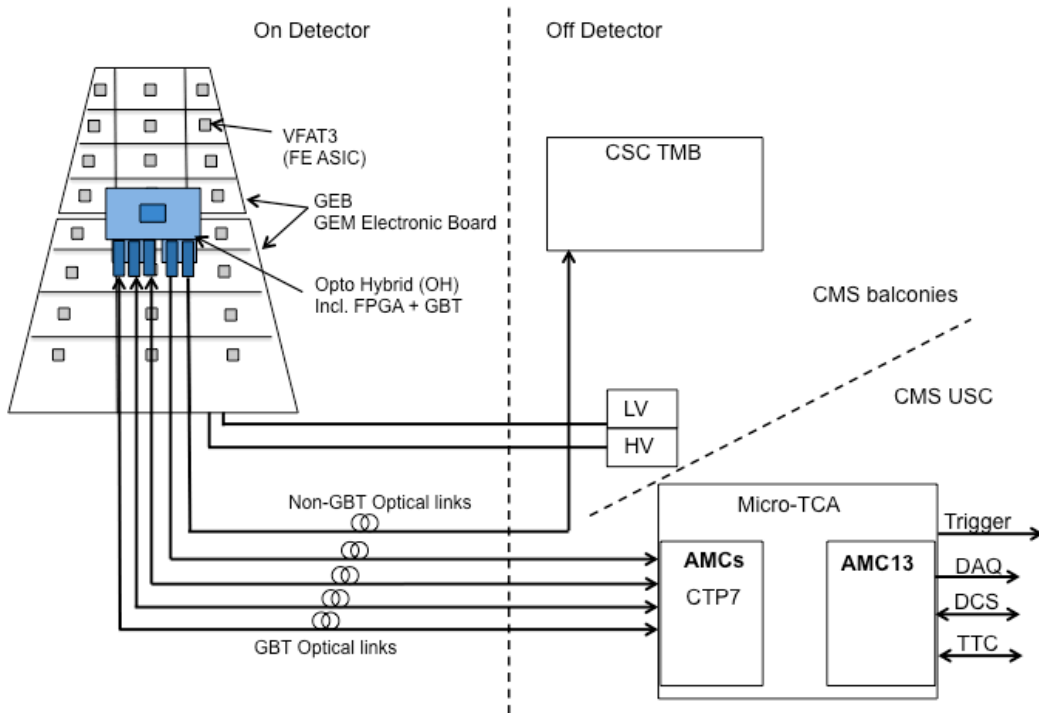


Figure 3.4 – Overview of the GE1/1 readout electronic. The opto-hybrid, in which the TDC will be implemented, is in blue. [31]

counter increased each time an event is accepted by the L1 trigger. The SRAM2 data are sent through the "e-port" to the opto-hybrid.

The e-port [42] of the VFAT3 is the main communication port of the VFAT3. The LHC clock is sent through that port as well as the fast controls (mainly the Level 1 Accept (L1A)). As said before, the tracking data are sent via the e-port. Finally, the e-port is used for the bidirectional slow controls communications. The slow controls include all the monitoring and configuring functionalities of the chip.

### 3.3.2 The GEB

The GEM Electronic Board (GEB) is an 8 layers Printed Circuit Board (PCB) connecting the different readout electronic components between themselves and with the triple-GEM. It has two main purposes : (1) connecting the VFATs to the opto-hybrid and preserving the signal integrity; (2) providing power to the VFATs and opto-hybrid. The PCB must then route a large number of tracks ( $\sim 500$  differential signals + power + ground) and support the DC-DC converters needed for powering. Moreover the GEB undergoes mechanical stress being the support layer of a number of connectors.

In its final version, the GEB is composed of two PCBs as seen on the picture 3.6. The central black connectors are connected to the opto-hybrid while the 24 white connectors spread over the boards are connected to the VFATs.

### 3.3.3 The opto-hybrid

The opto-hybrid (OH) is responsible for the communications between the chamber and the off-detector electronics. It can be divided in two parts :

**The FPGA concentrator** The OH uses a Virtex-6 FPGA (see section 4.1 for more details), a fully configurable digital chip. Its firmware compresses the S-bits received from the 24 VFAT3s of a chamber and then transmits these using an 8b/10b protocol through optical fibers to the off-detector GEM electronics, the CTP7, and the CSC TMBs. The FPGA does not handle the VFAT3 slow controls, fast controls and tracking data. The TDC (see chapter 4) we will be implemented in this device.

**The GBT communication** The GigaBit Transceiver (GBT) [39] is a protocol developed by the CERN to reliably transmit data through an optical fiber in presence of high radiation while maintaining a multi-gigabit transmission speed. Moreover, they developed an ASIC, called the GBTX, for applications in high radiation environments. Three GBTX are connected to the VFAT3 e-ports and carry clocks, slow controls, tracking data and trigger event from and to CTP7.

### 3.3.4 Off-detector electronics

Like many other CMS upgrades, the off-detector electronics of the GE1/1 project will be hosted in one  $\mu$ TCA crate. The  $\mu$ TCA is a standard introduced by the telecommunication industry which imposes the size of the pluggable boards as well as the communication lines between them.

In the GE1/1 project, the chosen data processing board is the CTP7 board which was designed for the CMS HCAL Trigger Upgrade. Within the  $\mu$ TCA crate, the CTP7 boards communicate through the carte backplane with a dedicated board, called the AMC13, which is the interface with the central CMS data acquisition system. The AMC13 is also responsible to broadcast the LHC clock as well as the L1A to the front-end electronics.

One CTP7 board can manage 12 OH so that the full GE1/1 off-detector electronics can be located in a single  $\mu$ TCA crate.

## 3.4 Readout electronics used in this master thesis

The multiple iterations of the GE1/1 detector lead to the creation of numerous prototype versions for both the chamber and its electronics [33].

Because of challenges in the production of the GEB, the first version of the electronics could only access 6 VFAT2s. Moreover, the opto-hybrid (OH) v1 was based on a Spartan-6 FPGA instead of the Virtex-6 used for all the subsequent versions.

The table 3.1 shows the versions which were used in test setups.

The version 2a was used in test beams of November 2015. It handles the 24 VFAT2s and can be connected with up to 12 optical links to the off-detector board. The LHC clock is recovered by standalone Phase-Locked Loops (PLL) soldered on the PCB.

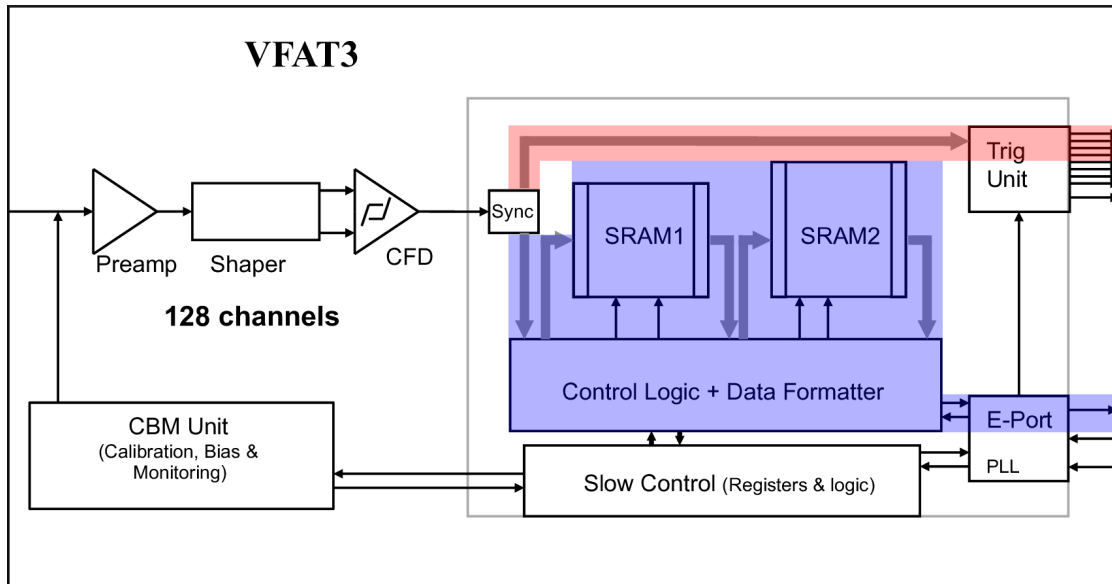


Figure 3.5 – Block diagram of the VFAT3. The trigger path is highlighted in red and the tracking data is in blue. [7]

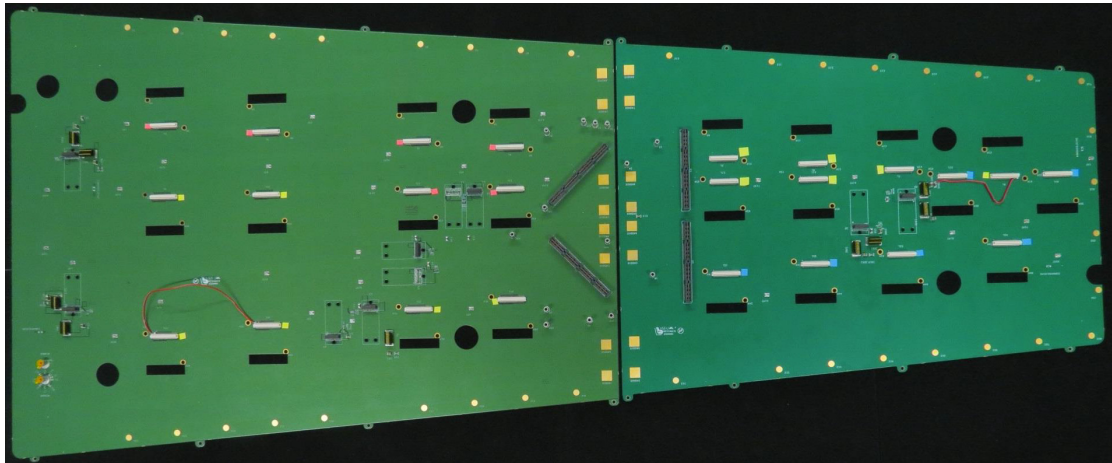


Figure 3.6 – Picture of a GEB3. [31]

<b>Prototype 2a</b> - 2015 Full size GEB (one piece) VFAT2 Opto-hybrid with Virtex-6, emulating GBT protocol Backend: GLIB board
<b>Prototype 2b</b> - 2016 Full size GEB (one piece) VFAT2 Opto-hybrid with Virtex-6 + 1 GBT + 1 SCA, VTTx and VTRx Backend: GLIB or CTP7 boards
<b>Prototype 3c</b> - Q2 2018 Full size GEB (two pieces) VFAT3b Opto-hybrid with Virtex-6 + 3 GBT + 1 SCA, VTTx and VTRx Backend: CTP7 boards

Table 3.1 – History of the GE1/1 prototypes used in tests. [31] The Slow Control Adapter (SCA) is a radiation hardened ASIC dedicated to the slow control functions. The VTTx and VTRx are radiation hardened optical transmitter and transceiver, respectively.

The version 2b was used in the slice test installed in CMS in January 2017. It is an update of the version 2a in order to accommodate the mechanical constraints of the GE1/1 chambers. The FPGA handles only 3 optical links, but a fourth optical link is connected to a GBTX chip which is in turn connected to the FPGA by e-links.

The version 3c is the latest version which should be installed in CMS during LS2. While the FPGA stays identical, the version 3 is total redesign. The communication is provided through three GBTX chips which control both the VFAT3s and the FPGA. As explained above, the FPGA in the v3 electronics is only used to compress the S-bits.

### 3.4.1 Electronics v2a

#### VFAT2

The VFAT2 is the front-end ASIC used in the prototypes of the GE1/1 project. It serves the same purposes as the VFAT3 front-end, that is amplifying and digitizing the signals of its 128 channels.

Its block diagram is shown on figure 3.7. The main difference with the VFAT3 lies in the communication protocol. Indeed, the electrical interface is composed of more signals. The slow controls are managed by an I2C bus whereas the fast controls and tracking data have dedicated LVDS lines. As a consequence, it is not possible to directly connect the VFAT2 to a GBTX chip; all the communications must pass through the opto-hybrid FPGA.

The trigger data are composed of 8 S-bits, each of them being the logical OR of 8 adjacent strips. These are transmitted through 8 LVDS lines without requiring any Time-Division Multiplexing (TDM).

One VFAT2 feature which is directly related to the time resolution of the triple-GEM detector is its simple threshold discriminator. The drawback of this method is that the crossing time

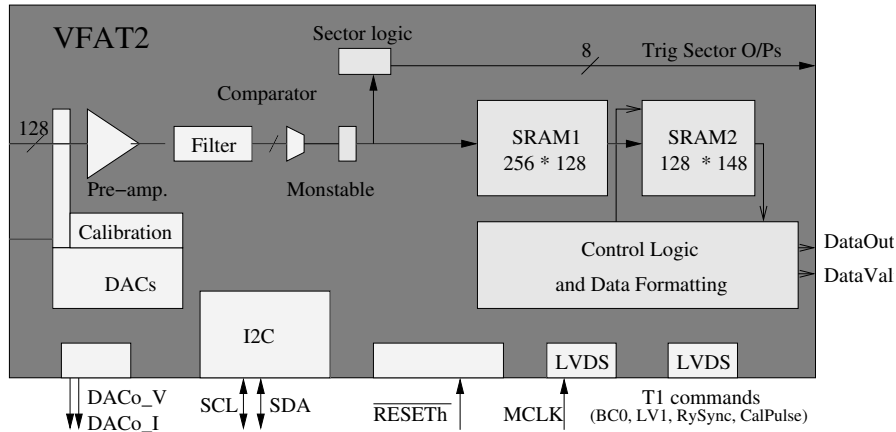


Figure 3.7 – Block diagram of the VFAT2. [6]

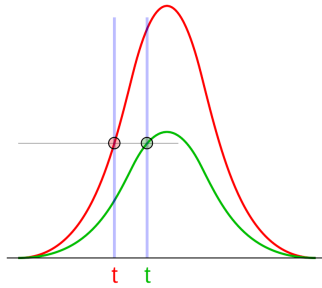


Figure 3.8 – Time-walk induced by a simple threshold discriminator. The two signals have the same shape, but the red one passes the threshold before the green one only because of its bigger amplitude. [24]

depends on the amplitude of the signal. This is clearly observable on the figure 3.8 where the red signal passes the threshold before the green signal although they share the same shape.

Because the induced signal on the electrode can have amplitude fluctuations for muons of identical energies (see section 2.5), the crossing time also suffers from time fluctuations.

### Opto-hybrid v2a

The opto-hybrid v2a was used in the test in beams. It is designed around the same FGPA as the OH v3, but the communications are managed differently.

The FPGA is connected to all the VFAT2 signals via the GEB. Its firmware manages the communication protocol with the VFAT2s and provides a simpler interface to the off-detector board. The communication with the off-detector is done through an optical fiber using a custom protocol based on the 8b/10b encoding.

One HDMI connector is also present on the OH. It serves for debugging purposes and external measurements.

Two lines are used to receive an optional external clock and an optional external trigger. The six other lines are used to output the S-bits of configured GEM sectors.

More than a concentrator, the OH v2a firmware is able to perform different tests on the VFAT2s and the detector. Among these tests, the threshold scan and the S-Curve scan were thoroughly used for optimizing the time resolution measurement setup. Detailed explanations are given on section 5.5.

Performing the scans on the OH is faster than retrieving all the data to the DAQ computer. [33] Indeed, the FPGA can operate at line rate whereas the communication with the DAQ computer is limited at 1 Gbps.

### **GLIB**

The Gigabit Link Interface Board (GLIB) is the gateway between the DAQ computer and the OH.

The GLIB encodes and decodes the data of the optical fiber connected to the opto-hybrid. The communication with the DAQ computer is done with the IPBus protocol.

### **WebDAQ**

The basics functions of the DAQ system were made available via a web application, called the WebDAQ. [33] More complex operations are scripted in Python via an IPBus library.

## Chapter 4

# Implementation of the TDC

A Time-to-Digital Converter (TDC) is a device dedicated to the digitization of time at which events occur. As examples, we can name the measure of time interval between two events or the time a signal stays over a defined threshold.

We can distinguish different methods for implementing such a device :

- The simplest method is the use of a **counter** which is reset by the start event and stopped by the end event. The main drawback is the required clock frequency needed to achieve high precision. For example, the counter must run at 1 GHz for a 1 ns precision.
- When a counter cannot be used and the time intervals are small enough, an analog technology is usable. In this case, a charge is collected in a **capacitor** during the time interval of interest. At the end event, one must use an ADC<sup>1</sup> to extract a numeric value.
- The last and most versatile method is the use of a **delay line**. It is based on the propagation delay of the hit information and can easily be combined with the counter method to obtain large interval measurements.

The technology adopted for this project (an FPGA) prevents the use of both analog and fast counter methods. However, the implementation of the delay line method within an FPGA can achieve time resolution of up to 10 ps as shown by [50, 25, 36].

In this chapter, we first briefly introduce the internals of an FPGA in section 4.1. The section 4.2 describes the working principle of a tapped delay line. Sections 4.3 and 4.4 detail the implementation of the TDC within the FPGA and the achieved performances. Finally, we optimize the implementation for the GE1/1 project in section 4.5.

---

<sup>1</sup>An Analog-to-Digital Converter is a device whose function is to digitize a voltage.

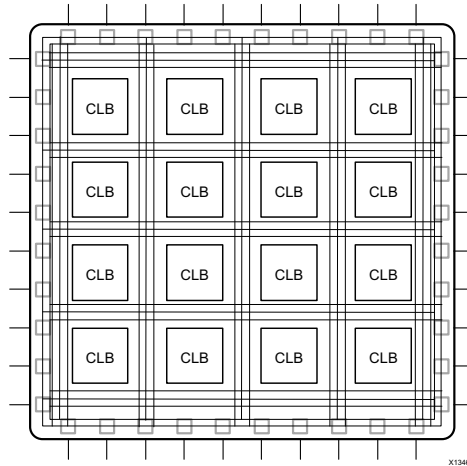


Figure 4.1 – The basic structure of an FPGA. We can see the CLBs matrix connected by the routing resources. On the edges, one can identify the IOs. [51]

#### 4.1 What is an FPGA ?

*Warning: While the description below is fairly general, some parts and particularly the terminology are only applicable to Xilinx FPGAs, especially the Virtex-6 family.*

An Field-Programmable Gate Array (FPGA) is a semiconductor device which is fully configurable and can be used to implement the design we need after fabrication. [51] It is opposed to Application-Specific Integrated Circuit (ASIC) which cannot be modified once manufactured. In this project, we used this versatility to implement the TDC in the opto-hybrid 3.3.3.

An FPGA is composed of different building blocks :

- The Configurable Logic Blocks (CLB) are the basic structures used to implement the logic needed by the design.
- Routing resources are used to connected the multiple CLBs as required.
- Input/Output (I/O) pads are used to communicate with the external components.
- A variety of more specialized resources : clocks used for implementing synchronous circuits, high-speed transceivers for fast communication, Block-RAM to store bigger amount of data than it is possible in CLBs, ...

Among these elements, the CLBs are the most common and those in which the TDC is implemented. They are organised following a matrix pattern as represented figure 4.1. The CLBs are themselves composed of simpler components : Look-Up Tables (LUTs), flips-flops and carry logic.

The configuration of all these resources is not done by hand. Description languages, in this master thesis VHDL (VHSIC Hardware Description Language), are used to describe the expected operation of the FPGA in a more abstract way. Software tools then convert this description in *bitstream* which configures the FPGA.

clk	rst	D	Q
x	x	x	Q
↑	1	x	0
↑	0	x	D

Table 4.1 – Truth table of a D flip-flop.



Figure 4.2 – Symbol of a D flip-flop

#### 4.1.1 LUTs

Digital devices process signals which have a discrete number of values, in this case two, represented by 0 and 1. As FPGAs are universal devices, they must be able to implement any boolean function.

This is the function of the LUTs. Each LUT with  $N$  inputs can implement any of the  $2^{2^N}$  possible boolean functions where  $N = 6$  in the FPGA family we use. By combining a large number of these building blocks, one is able to implement any combinatorial function.

#### 4.1.2 Clocks and flip-flops

It is not possible to create sequential function with the use of LUTs only. To achieve such operation, one needs some kind of memory, that is flip-flops. Moreover, the use of synchronous circuits makes easier the conception of a digital circuit. Indeed, the fabrication processes cannot guarantee perfect delays for the signals. As the signals propagate asynchronously, they cannot be time aligned in huge devices in order to achieve a predictable result. The idea behind the use of synchronous circuit is to split the processing tasks in little steps which are easily converted into hardware. The result of each of these steps being stored long enough for the next step.

The way of synchronizing a circuit is to use a square signal called a clock. The clock has two characteristics which are important in the project : the frequency and the jitter. The jitter is the fluctuation of the periodicity of the clock and is part of every system. It has direct impact on the performances of the implemented TDC.

FPGAs have specialized resources to create and distribute clocks throughout the silicon die. The specialized distribution network is needed to achieve a low jitter. This also provides a low skew which is the difference in arrival time of the same clock to different components.

A *D flip-flop* is an elementary storage unit able to store a single bit and controlled by a clock signal. It is symbolized by the symbol 4.2 with the truth table 4.1 where  $>$  or *clk* is the clock signal, *rst* the reset signal and *D* and *Q* respectively the input and the output. At the rising edge of the clock, symbolized by  $\uparrow$ , the input *D* is sampled and reproduced on the output *Q* if the reset signal is not asserted. If the reset signal is asserted, the output *Q* is set to 0. In any other case, symbolized by *x*, the output remains stable.

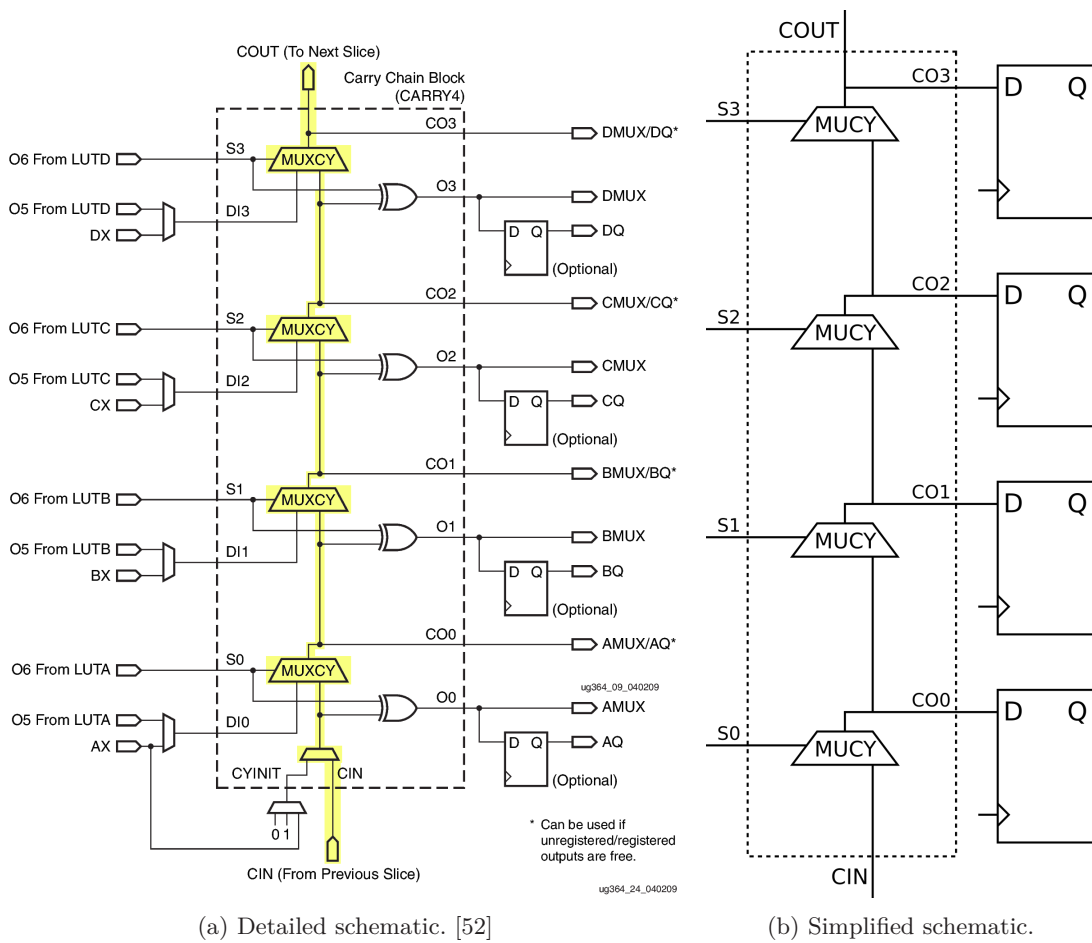


Figure 4.3 – Schematics of the CARRY4 primitive. The path which will be used as the delay line is highlighted in yellow.

We could mention that there are other modes of operations for the flip-flops in an FPGA, but they were not used in this project.

### 4.1.3 Carry logic

The last component of the CLBs is the carry logic. Its original use is the implementation of fast binary adders or multipliers. The carry logic is split in elements, called the CARRY4, which are placed in columns and can be chained on the full height of the FPGA.

Figure 4.3a represents the schematic of one CARRY4 primitive. On the left inputs are named  $DI_i$  and  $S_j$  while the outputs on the right side are  $O_k$  and  $CO_l$ . The chaining is assured by the  $CINT$  output which can be connected to the  $CIN$  input of the following CARRY4 using dedicated routing resources. Its internals are composed of the multiplexers  $MUCY$  and XOR logic gates.

With a properly configured carry logic, a signal can propagate an entire FPGA column through the CARRY4s. The path within a CARRY4 is highlighted in yellow.

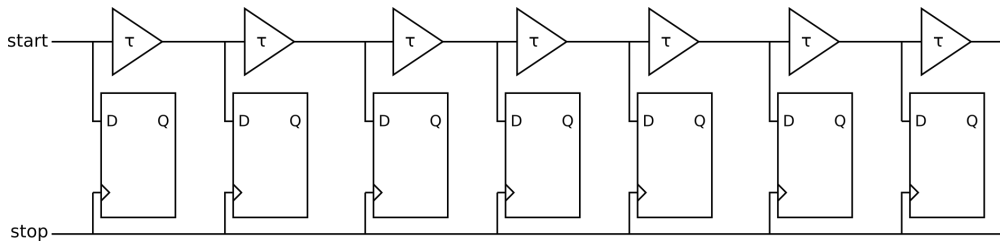


Figure 4.4 – Schematic of an ideal tapped delay line.

## 4.2 Tapped delay line

Depending on the required precision and stability, but also the available technology, there are variations of the delay line. As the available logic is limited and the required precision is not extreme (see simulations in section 5.3), one basic variant has been chosen : the **tapped delay line**.

The diagram 4.4 shows a series of flip-flops fed by a progressively delayed start signal. The stop signal drives the clock input of the flip-flops. When the stop signal reaches the flip-flops the progression of the hit information in the chain of delays is sampled, stored and available on the outputs Q. The time interval between the start signal and stop signal is proportional to this progression.

The tapped delay line method can be associated with a coarse counter in order to measure intervals longer than the delay line. In this configuration, the stop signal is replaced by a sampling clock. Henceforth, one gets the timestamp of each hit event, that is the coarse counter minus the time spent in the delay line.

Knowing the timestamp of multiple events (which may have been sampled by different delay lines in multi-channel TDC) allows the computation of time intervals.

## 4.3 Implementation of the TDC

In each channel of the implemented TDC, the hit signal first reaches a launcher. The launcher cleans the hit signal and sends a known pattern in the delay line.

The simplest version of a launcher is shown in red in the figure 4.5b. The hit signal drives the clock input a D flip-flop whose input D is tied to 1. The D flip-flop has its output Q reset to 0 in the initial state. This launcher is only sensitive to the rising edge of the hit signal and sends a single transition from 0 to 1 in the delay line.

The advantages of the CARRY4 make it an obvious choice to implement the delay line within an FPGA. Indeed, the routing between different primitives is dedicated while the multiplexers can form small delays.

One can also notice the similarity between the tapped delay line, figure 4.4, and the simplified schematic of the CARRY4, figure 4.3b. By chaining multiple CARRY4, one gets all the delay elements of the tapped delay line. After each delay the signals can be sampled in D flip-flops.

In order to improve the range of the TDC while limiting the FPGA ressources usage, we will associate the delay line with a coarse counter. The stop signal will so be the clock which drives

the counter. In this case, we can note that the chain must be longer than the sampling clock period otherwise we could not measure a progression past the delay chain duration.

Once the signals are sampled by the rising edge of the sampling clock, the hit information progression is available on the outputs of the flip-flops. As the launcher sends a clean transition from 0 to 1, the sampled vector will be of the form : 111111110000. Figure 4.7a shows the time diagram of the signals in the delay line after being sent with the simple launcher. At  $t_0$  the hit information is launched and at  $t_1$  the signals are sampled by a perfect clock (in blue). Finally, the delay chain is reset.

This thermometer code is converted into one-hot binary encoding and then to a binary number by the logic implemented in the FPGA. The higher the number, the earlier the hit signal arrived before the sampling clock rising edge.

From figure 4.3a, we see that the structure of the tapped delay line is more complex than the ideal one presented figure 4.4. In an FPGA, the tapped delay line is composed of delay elements with different durations,  $\tau_1, \tau_2, \tau_3, \dots$ , as shown figure 4.5a. Moreover, the delays will vary with fabrication process, voltage and temperature factors (commonly called PVT factors). This is why an online calibration needs to be frequently run.

By implementing multiple channels, we can measure time intervals between signals. Indeed we know the timestamp of each event by combining the coarse counter with the delay line :

$$t = P * c - \text{calib}(p)$$

where  $P$  is the sampling period,  $c$  a free counter running at the sampling period frequency and  $\text{calib}(p)$  the calibration function which convert the progression  $p$  into a time.

As the implementation of the delay line requires manual placement and is very sensitive, we have joined its VHDL code in appendix A.

### 4.3.1 Calibration

The calibration is needed for each channel as they do not share the same placement on the FPGA. Calibrating the TDC requires events uncorrelated to the sampling clock. The sampling clock is generated from the external 40 MHz while the calibration events are generated by the ring oscillator present in the FPGA.

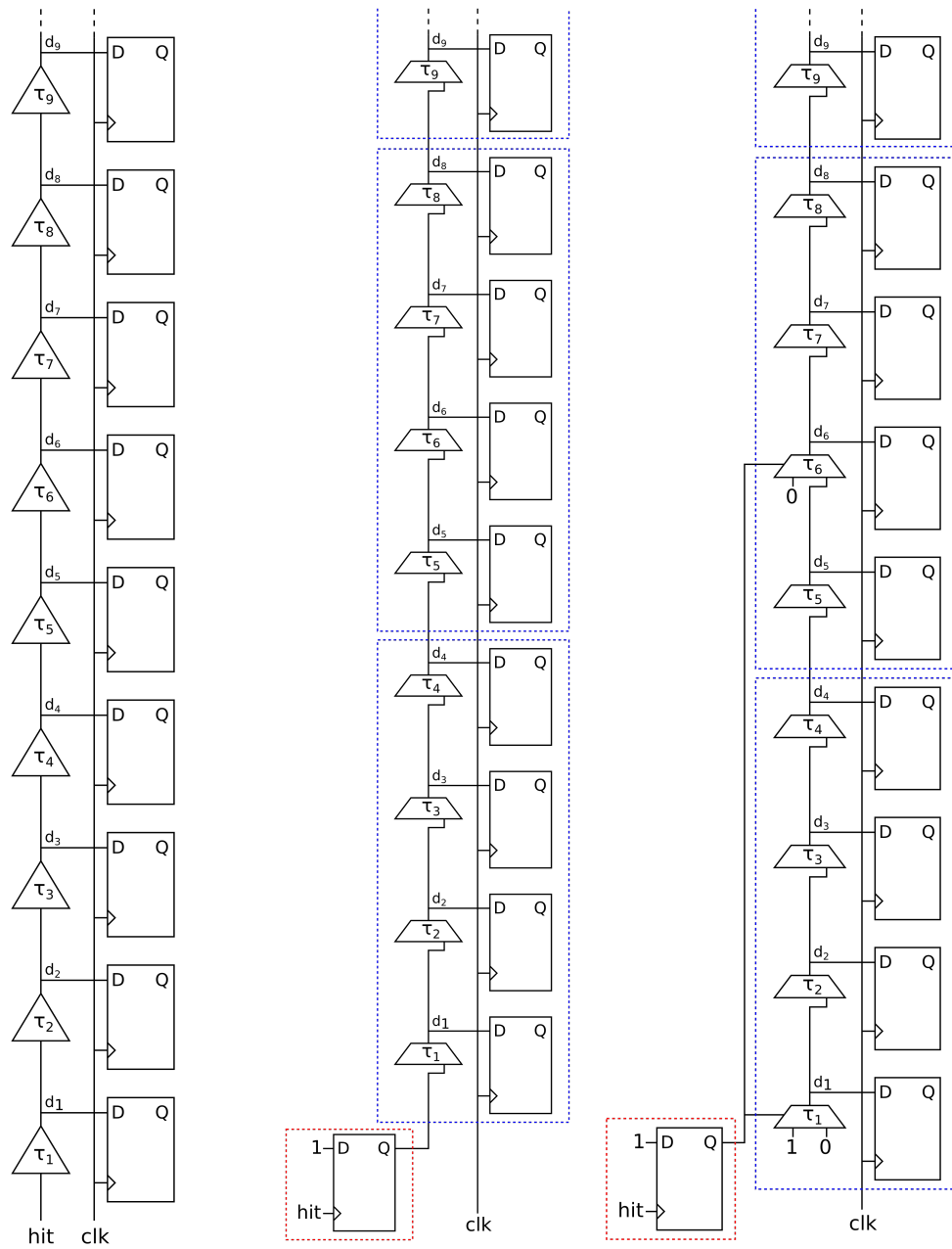
By sending these events to a TDC channel, one can build an histogram of the pattern progression in the delay line and correctly scale it to get the duration of each delay. Indeed, the longer the delay, the more events will be in the bin :

$$d_i = N_i * \frac{P}{N_{tot}}$$

where  $N_i$  is the number of events in the bin  $i$  and  $N_{tot}$  the total number of calibration events.

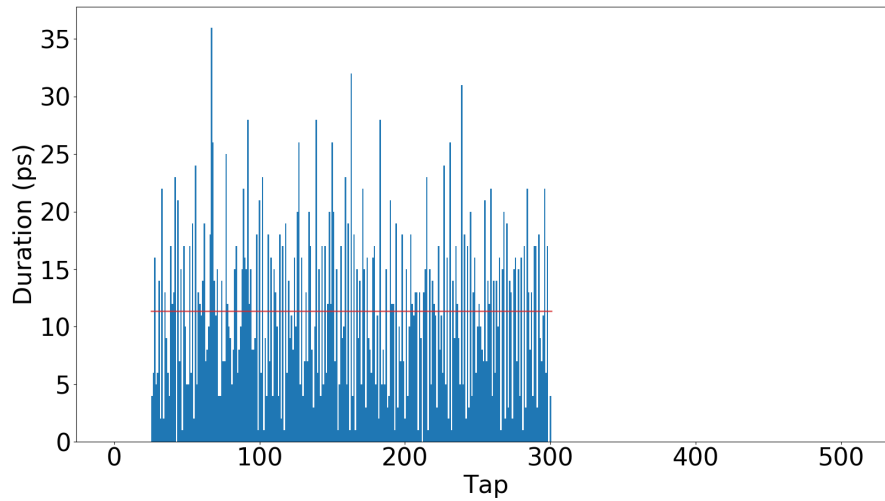
An example of such histogram is viewable figure 4.6a which represents the duration of a delay as a function of the progression of the hit information in the delay line for the final version of the TDC.

An integrated calibration unit triggered by software as needed was developed. Since the calibration requires a significant number of events (25 000 in our implementation) to be precise, the internal calibration was also a way to make it very fast ( $< 10$  ms).

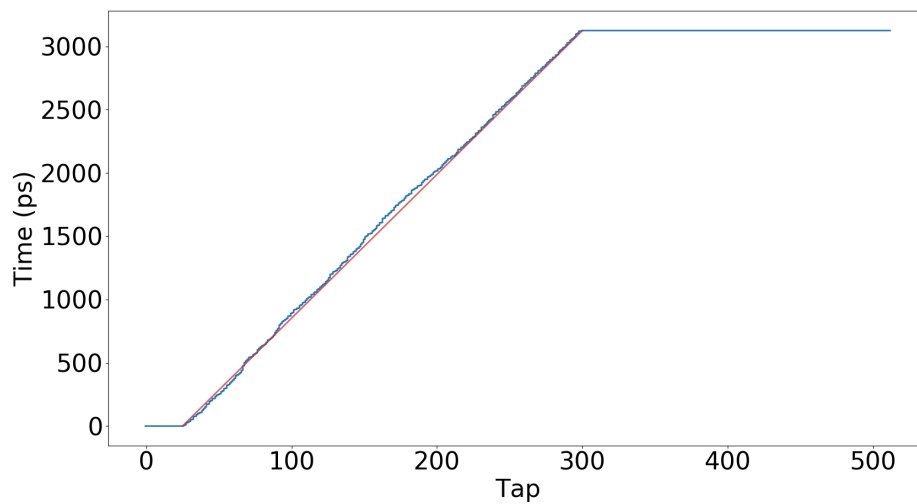


(a) Tapped delay line without launcher (b) FPGA tapped delay line (c) FPGA tapped delay line with Wave Union launcher

Figure 4.5 – From left to right, more advanced versions of a tapped delay line. The red boxes are the launchers. Each CARRY4 with its flip-flops is in blue.



(a) Calibration histogram for two channels.



(b) Calibration lookup table for two channels.

Figure 4.6 – Calibration graphics for the FPGA TDC. The data are in blue while the red lines represent the ideal case.

The integration of the histogram leads to the creation of a calibration lookup table. The result of the implemented FPGA can be seen figure 4.6b which shows the time spent in the delay line before the rising edge of the sampling clock as a function of the progression of the hit information in the delay line.

### 4.3.2 Wave Union A

During development stages, large variability in the delays (150 ps) was seen. These "ultra-wide bins" are mainly due to routing between CARRY4 primitives and clock skew.

This lead us to implement what was called by its creators, a "Wave Union-A" launcher [50] to subdivide these "ultra-wide bins". This more sophisticated launcher consists in the launch of a pulse in the delay chain rather than a single edge. The pulse has thus two levels transitions to be sampled. If the pulse length is wisely chosen, the probability of always having one edge in a short delay is high. The only drawback was the need of detecting the two edges and convert them into integers.

The figure 4.7b shows the timing diagram of the  $d_i$  signals of the schematic 4.5c with a Wave Union-A launcher. At  $t_0$  the hit signal reaches the launcher and the pulse is released. At  $t_1$ , the signals are sampled by a perfect clock (in blue). Once the signal is sampled, the output vector of the flip-flops is of the form : 00000111110000. The logic next finds the edges, converts their positions to integers and sum them.

With a Wave Union-A launcher, the longest delay is now  $< 40$  ps as the figure 4.6a shows.

### 4.3.3 Bubbles

The other problem related to FPGAs is the apparition on "bubbles" in the sampled signal, because of a race condition between the data - the signal propagating through the delay chain - and the clock - the stop signal. Indeed, a small skew in the clock distribution network can flip bits in the output vector.

The situation is represented figure 4.7b for a Wave-Union A launcher, but also exists for a simple launcher (see figure 4.7a). If the sampling clock has skew, it will sample the signals at different times and not at the nominal time  $t_1$  (in red). That is, the sampled signal will look like : 0000011101000.

The bubble (in red) can appear both in the front or the back of the pulse while its distance from the edges (in blue) can be bigger than one.

Experience has shown that the small "pulse" (in blue) separated from the main pulse (in green) by the bubble (in red) is never longer than 3. Henceforth, a new layer of logic was added to only detect the part of the pulse which has a length superior to 4 flip-flops, that is the main pulse.

## 4.4 Performances

The FPGA TDC resolution was tested with a commercial function generator (Tektronix AFG3252C) and compared to a commercial TDC (CAEN Mod. V1290 [13]).

The integrated TDC version under test was build around two channels each with a calibration unit. The function generator sent one pulse on each of its two channels with a phase between them. The TDC had to reconstruct the time difference between these two pulses.

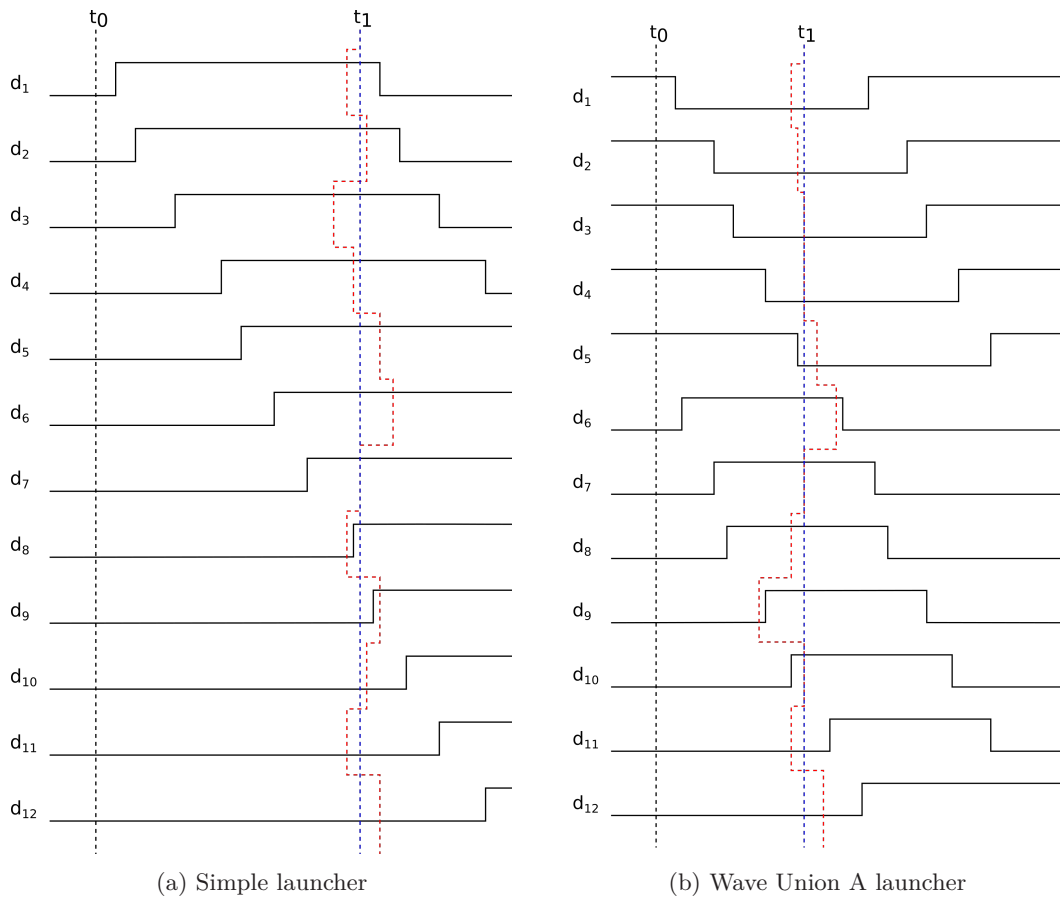


Figure 4.7 – Time diagram of the signals in the tapped delay line for different launchers. The pulse is released at  $t_0$  while it is sampled at  $t_1$  by a perfect clock (in blue) or a clock with some skew (in red).

The figure 4.8 shows the distribution of the measurements of a time interval fixed to 200 ns between two signals produced by the function generator and measured with our FPGA TDC implementation. As we can see, the result is Gaussian with a standard deviation of  $64.3 \pm 0.5$  ps. The average is shifted between the generated interval and the measured value. This can be explained by the difference in the propagation delays of the two signals. Indeed, the cables and FPGA internal routing before reaching the beginning of the delay line is slightly different. This bias can be measured and then corrected. As it has no consequences on the time resolution, the correction was not done.

The figure 4.9 shows the evolution of the time resolution  $\sigma$  for increasing time intervals for our FPGA TDC (in blue) and for a commercial TDC (in red). The range of tested time intervals between two signals has been chosen as the maximal range between the S-bits and the external trigger. In our implementation the resolution degrades to reach a plateau under 150 ps. The most probable explanation is the jitter in the sampling the clock. [25] The bias was also measured at  $343 \pm 19$  ps for the different time intervals.

Finally, the table 4.2 summarizes the TDC characteristics. Note that the deadtime is here

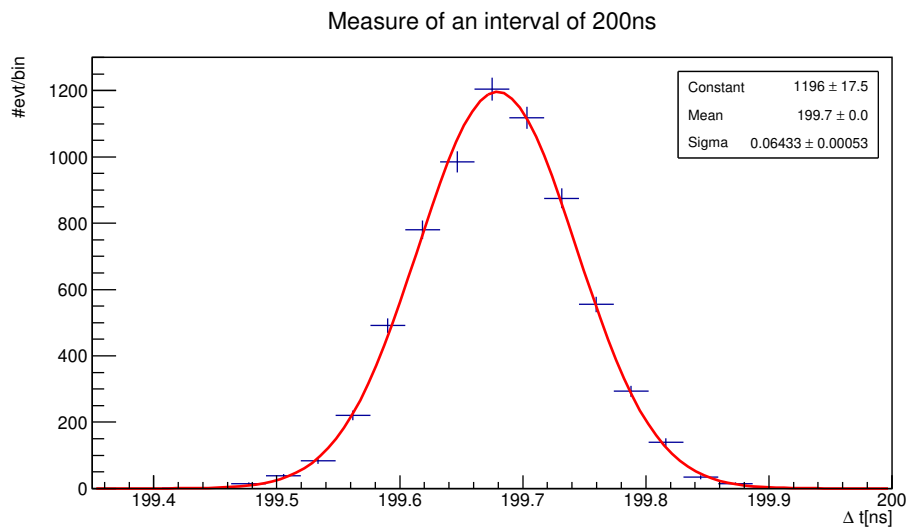


Figure 4.8 – Time distribution measured by the FPGA TDC for a generated interval of 200 ns.

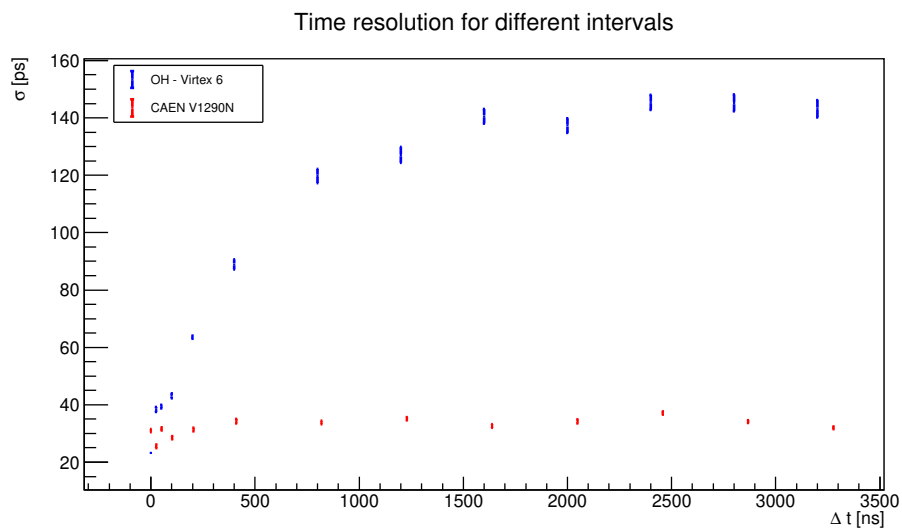


Figure 4.9 – Evolution of the time resolution for increasing generated time interval between two channels. The commercial TDC is in red while the FPGA TDC is in blue.

defined as the duration during which a channel is not sensitive to new events after having been triggered. The latency is defined as the number of clock cycles between the clock edge which sampled the progression in the delay line and the clock edge where the measurement is available for further processing.

Frequency	320 MHz
Delay line length	256 delay elements (64 CARRY4)
Latency	6 clock cycles + 1 40 MHz clock cycle
Dead-time	< 4 clock cycles
Precision	< 150 ps

Table 4.2 – Characteristics of the implemented TDC.

#### 4.5 Implementation in the GE1/1 opto-hybrid

In a naive use in the opto-hybrid, one would need 25 channels (1 for the external trigger and 24 for the VFAT2s) for each GE1/1 detector. Using a complete TDC channel for the VFAT2s is however unnecessary and requires multiple carry chains and calibration units. Using the fact that the VFAT2s send synchronous signals at 40 MHz, we can optimize our implementation of the FPGA TDC.

In the optimized implementation, the external trigger remains measured by a channel of the TDC previously developed because it is asynchronous.

However, the S-bits of each VFAT2 are now sent to a shift register - a chain of D flip-flops - of 256 elements where their logical OR are stored. That is, the hit signal from the VFAT2s are shifted of one flip-flop at each 40 MHz clock cycle. When an external trigger is received, a priority encoder finds the oldest S-bit and returns its position within the shift register. The block diagram of that optimized TDC module is shown in the figure 4.10.

As we know the position of the oldest S-bit and the time of arrival of the external trigger, we can compute the time interval  $I$  :

$$I = P * v + P/8 * c - calib(p)$$

where  $P$  is the period of the VFAT2 clock, 25 ns,  $v$  is the position of the oldest S-bit and  $c$  the number of 320 MHz clock cycles from the last rising edge of the 40 MHz clock.

With our optimized TDC, we then only need one tapped delay line along with one calibration unit. The complete TDC uses 8268 LUTs, 8699 flip-flops and 128 CARRY4.

The number of CARRY4 is doubled compared to table 4.2 in order to improve the reliability of the delay line without impacting its resources usage. Indeed, as said before, the length of the delay line must be longer than the sampling period. As 64 CARRY4 were close to the limit, the length of the delay line was doubled.

However, in order to avoid using more FPGA resources, the rest of the logic remained identical by only using one flip-flop out of two in the delay line. While the delays should theoretically have doubled, the time resolution was not impacted. Indeed, the race conditions

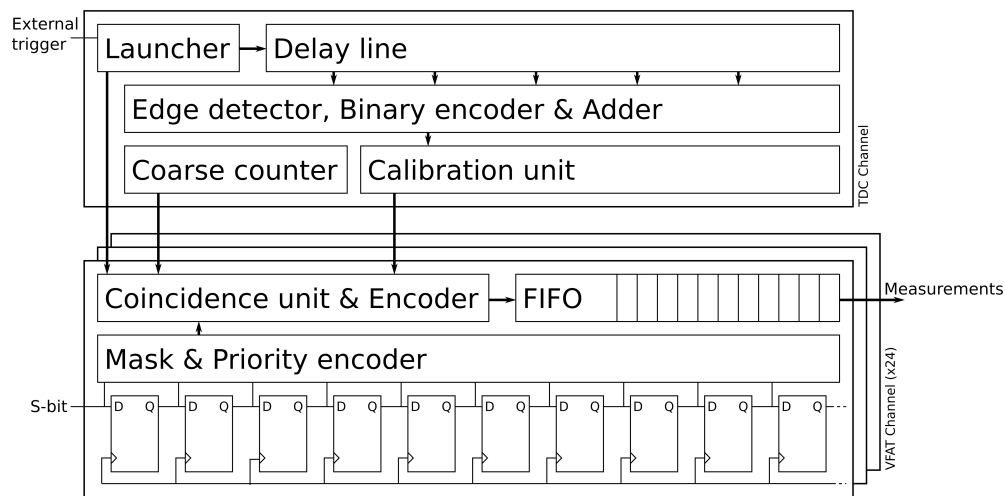


Figure 4.10 – Block diagram of the TDC implemented within the GE1/1 opto-hybrid.

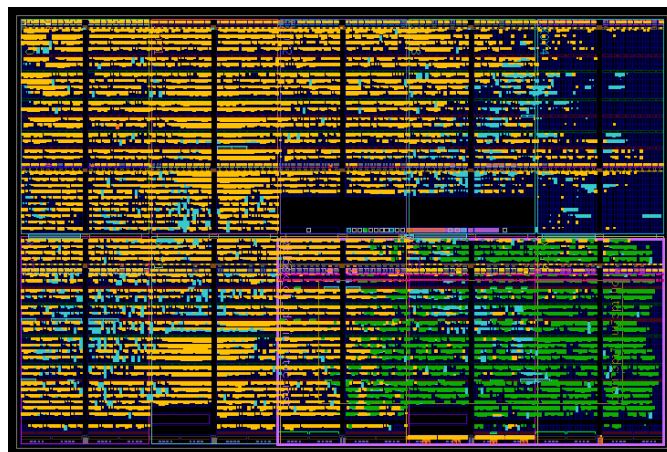


Figure 4.11 – Floorplan of the FPGA firmware. The TDC module is in green with the delay chain emphasized in pink. The S-bits cluster packer is in orange. All the others elements are colored in cyan.

made one bin out of two empty in the calibration LUT. The average of the delays so remained identical.

The floorplan of the complete implemented firmware is show on figure 4.1. The TDC module is colored in green with the delay chain emphasized in pink. The majority of the FPGA area is occupied by the S-bits cluster packer, the module which compresses the S-bits before sending them to the optical links. The remaining elements are colored in cyan.



## Chapter 5

# Measurements and analysis

With the TDC implemented as described in the previous section, we are now able to measure the time resolution of the CMS GEM detector in a fully integrated way.

During the prototyping stages, the time resolution was previously measured around 8 ns for drift fields between 2 kV/cm and 3 kV/cm with a gas mixture of 70%Ar+30%CO<sub>2</sub>. [27] This is the value we try to reproduce with the TDC embedded within the opto-hybrid FPGA. It is important to mention that most of the previous measurements of the time resolution have been done with small 10 cm × 10 cm prototypes, often with other gas mixtures or gas gap geometries, and with a different electronics. Very few results on the time resolution exist for full-size GE1/1 detectors and with 70%Ar+30%CO<sub>2</sub> gas mixture. It is therefore crucial for the CMS trigger application to repeat this measurement and validate this parameter.

This chapter begins by explaining the measurement principle. The section 5.2 describes the setup we used and the different sources of uncertainties. Simulations based on the measurement principle are made in section 5.3. In section 5.4, the embedded TDC measurements are compared with a commercial TDC as a cross-check. The section 5.5 describes all the optimizations made to reduce the uncertainties and improve the measured time resolution of the GEM detector. The chapter ends with the final results and the study of the influence of the drift field and the particle incidence angle, on the time resolution.

### 5.1 Measurement principle

The goal of this study is to measure the time difference between the passage of the incident muon through the GEM detector and the S-bit signal sent out by the VFAT2 chip. Assuming Gaussian fluctuations, the time resolution is defined as the standard deviation of the distribution of this time difference.

As it will be explained in details in the following, there are two caveats to this measurement : (1) the incident particle being cosmic muons, their arrival time is asynchronous with respect to the detector electronics which works with a reference clock typically running at 40 MHz. (2) The exact time at which the incident muon crosses the GEM detector is unknown and must be provided by an external trigger system which serves as the time reference. The second caveat makes impossible to measure the actual time resolution of the GEM detector. Indeed, it is only possible to measure the "relative time resolution" of the detector compared to the time of reference.

The measurement is done as presented on the time diagram 5.1. At  $t_0$  the muon passes through the setup. After some time  $t_1$ , the signal at the output of the front-end amplifier

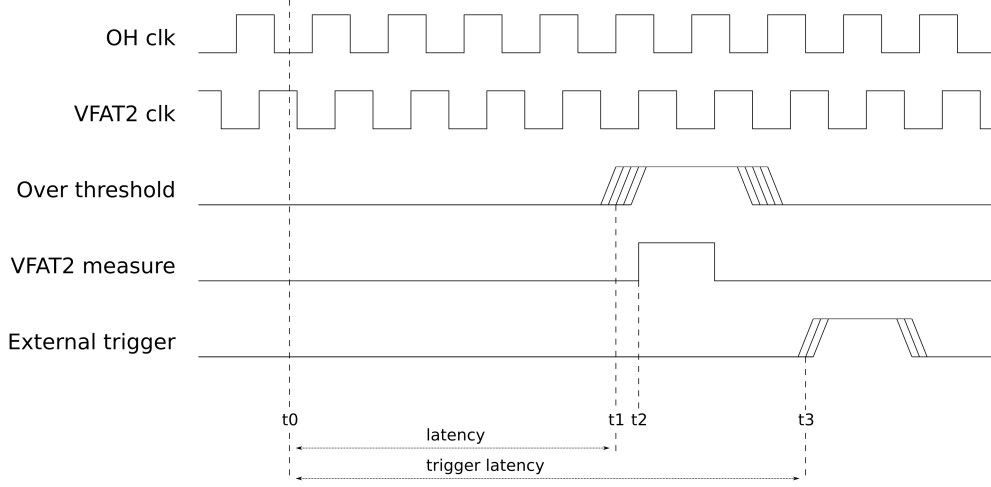


Figure 5.1 – Timing diagram of the measurement. At  $t_0$  the particle passes through the setup. The signal is over threshold at  $t_1$ , but only sampled by the VFAT2 at  $t_2$ . The trigger is asynchronously sent at  $t_3$ .

passes the threshold of the VFAT2 discriminator. This binary signal is then synchronized by the monostable on the next clock cycle at time  $t_2$ .

The time reference is sent by an asynchronous trigger at  $t_3$ . The trigger must come later than the GEM signal. This constraint is due to the working principle of the embedded TDC and is related to how the detector will operate in CMS<sup>1</sup>.

In order to retrieve the original time distribution,  $t_3 - t_1$ , we need to take into account the effect of the synchronizer. The time distribution,  $t_3 - t_2$ , actually measured is therefore the convolution between the original distribution and an uniform distribution over the clock period of the synchronizer. Indeed, the asynchronous GEM signal arrives at any time during the clock cycle preceding the sampling edge while the trigger is asynchronous.

Assuming the original time distribution is Gaussian, the convoluted time distribution takes the following form [27] :

$$\begin{aligned}
 s(t) &= (g * u)(t) = \int_{-\infty}^{\infty} A e^{-\frac{(t-\tau-\mu)^2}{2\sigma^2}} g(\tau) d\tau \\
 &= A \int_{-P/2}^{P/2} e^{-\frac{(t-\tau-\mu)^2}{2\sigma^2}} d\tau \\
 &= A\sigma\sqrt{\frac{\pi}{2}} \left( \operatorname{erf}\left(\frac{\mu + P/2 - t}{\sqrt{2}\sigma}\right) - \operatorname{erf}\left(\frac{\mu - P/2 - t}{\sqrt{2}\sigma}\right) \right) \quad (5.1)
 \end{aligned}$$

where  $A$  is a normalization constant,  $\sigma$  is the time resolution of the  $t_3 - t_1$  distribution we are trying to extract,  $P$  is the sampling period and  $\mu$  is the average of the distribution. This is the function which is used for all the subsequent fits.

<sup>1</sup>In CMS the trigger signal arrives exactly 3.2  $\mu\text{s}$  after the corresponding bunch crossing (see section 1.2.4).

## 5.2 The experimental setup

The experimental setup was designed to measure the time resolution of a single sector of the GEM detector which is the granularity of the embedded TDC.

The setup, whose schematic is drawn on the figure 5.2, is composed of different elements :

**A GEM detector and its electronics** The GEM detector under test is a GEM chamber version III with its v2a electronics. The data acquisition system (DAQ) is composed of a GLIB and a computer (see section 3.4.1).

**Four scintillators and their PMTs** These are used to provide the trigger and the time reference  $t_3$ .

On the top of the detector, a small scintillator ( $4.5 \text{ cm} \times 4.5 \text{ cm}$ ) is centered on the sector under test. Its small size, compared to the sector size, increases the geometrical acceptance.

Two scintillators, slightly bigger than a sector, are placed under the GEM chamber. They are used to provide the coincidence with the small scintillator.

A supplementary scintillator of  $8 \text{ cm} \times 15 \text{ cm}$  was placed 48 cm under the detector in order to optionally select the muons coming perpendicularly to the detector.

These 4 scintillators/PMTs will be called, respectively : *small PM*, *PM3*, *PM4* and *PM5*.

**A NIM crate with some logic modules** Discriminators and Constant Fraction Discriminators (CFD, see section 5.2) (Canberra Model 454 [14]) digitize the PMT signals. The signals of two of the four PMTs are sent to the coincidence unit where a logical AND is applied to produce the trigger. Before being sent to the opto-hybrid, the trigger is delayed and converted from the NIM electrical standard to TTL electrical standard.

**A commercial VME TDC** Besides the embedded TDC, a commercial TDC (CAEN Mod. V1290 [13]) is available in a VME crate connected to the DAQ computer. This TDC is used for crosschecking the results.

### 5.2.1 Sources of uncertainties

The block diagram on figure 5.3 shows the signal and data paths from the GEM detector and the PMTs to the opto-hybrid TDC. Each component is prone to produce some fluctuation on the signal timing. We can identify the following elements :

**GE1/1 chamber + VFAT2 (analog)** This is the uncertainty we want to measure. It is listed in the sources of uncertainties because parameters can be tweaked to improve the time resolution.

**VFAT2 (synchronizer)** It introduces the convolution with the rectangular function as explained in section 5.1.

**S-bits on the GEB** The S-bits are transmitted in copper tracks which could have mismatches in length as well as in speed of the signal propagation.

**PMTs** The scintillators and their PMTs have their own time resolution.

**NIM electronics** The NIM electronics can add some jitter.

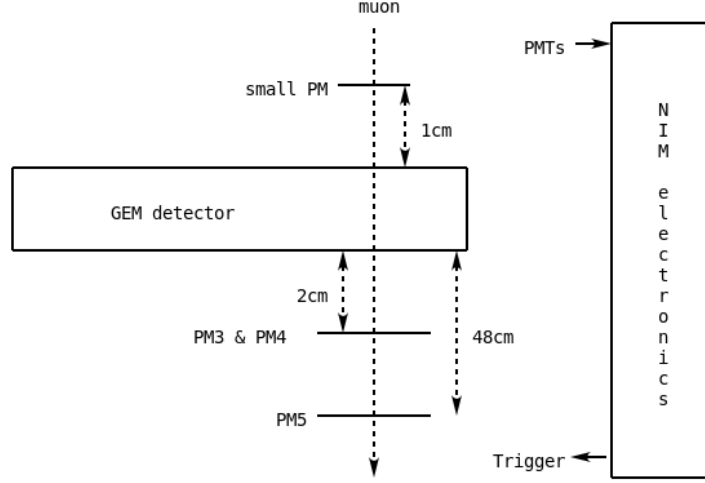


Figure 5.2 – The experimental setup used for the measurements. It is composed of a GEM detector and its electronics, four scintillators and the electronics required to produce the external trigger.

**TDC** The TDCs, both embedded and commercial, have their own time resolution which is known.

The above sources of fluctuation have been studied in this work and we have tried to mitigate them as much as possible (see section 5.5).

### 5.3 Simulations

Before taking data, simulations of the measurement principle were made in C++ using the ROOT framework [11]. It had two purposes : checking fit procedure (see equation 5.1) and computing the uncertainty on the estimation for different GEM time resolutions and setup precisions.

For each simulation, 50 000 events were generated. Each event was simulated with the following procedure (using the same notations as in the figure 5.1) :

1. At  $t_0 = 0$ , the muon passes through the detectors.
2. The GEM signal passes the threshold of the VFAT2 discriminator at  $t_1$ , distributed as  $\sim \mathcal{N}(\mu_{det}, \sigma_{det})$ . In this simulation,  $\sigma_{ref}$  embeds the fluctuations due to the PMTs, the NIM electronics and the TDC).
3. This time is rounded up to the next multiple of 25 ns, which is called  $t_2$ .
4. The time reference signal,  $t_3$ , is distributed as  $\sim \mathcal{N}(\mu_{ref}, \sigma_{ref})$ . In order to properly simulate the working principle constraints,  $\mu_{ref}$  must be bigger than  $\mu_{det}$ .
5. The difference  $t_3 - t_2$  is then stored into an histogram.

Finally, the histogram is fitted by the function 5.1 to extract the original time resolution.

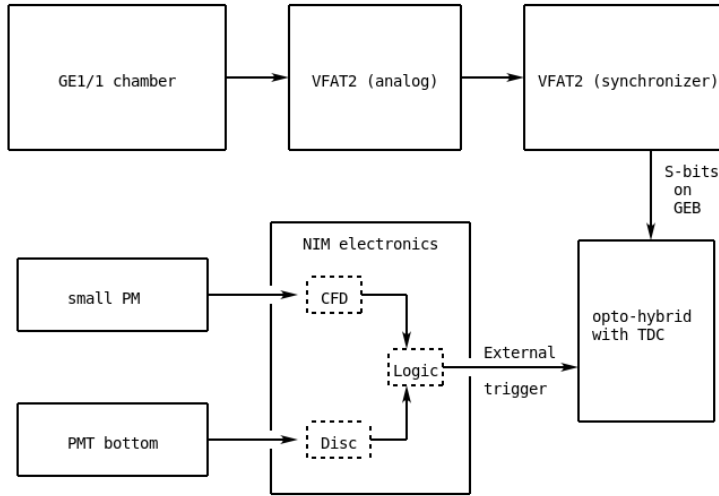


Figure 5.3 – Signal and data paths from the GEM detector and the PMTs to the OH TDC. Each element on the signal paths may produce fluctuations on the signal timings.

The figure 5.4 shows the simulation for a GEM detector having a time resolution,  $\sigma_{det}$ , of 8 ns and a setup having an uncertainty,  $\sigma_{ref}$ , of 2.5 ns. The time resolution from the fit amounts to  $8.278 \pm 0.042$  ns. The slight overestimation of the time resolution is attributed to the fact that the fluctuations due to the setup (PMTs, NIM electronics and TDC) are not taken into account in the fit function. These supplementary fluctuations (assumed Gaussian) smear the time distribution  $t_3 - t_2$ .

By running the simulation for different values of the GEM time resolution and for different setup uncertainties, one can compute the evolution of the overestimation of the recovered time resolution. The result can be seen on figure 5.5. The colormap shows the overestimation in percent for GEM time resolutions between 2 ns and 20 ns and for setup time resolution between 0 ns and 7 ns.

## 5.4 Crosscheck of the embedded TDC

As a first step, the embedded TDC was compared to the commercial TDC to crosscheck the OH TDC implementation. For this purpose the same events were recorded by the two TDCs.

The trigger was sent to the commercial TDC and one copy to the opto-hybrid. The logical OR of the S-bits of one VFAT2 are received by the OH and one copy is sent through its HDMI debug connector to the commercial TDC.

The distributions of the time differences between the S-bits and the external trigger are shown on the figure 5.6a for the embedded TDC and on the figure 5.6b for the commercial TDC.

Issues in the commercial TDC acquisition software caused the drop of some events. It was then impossible to compare the time differences event per event. Because of differences in cable lengths of the copied signals, the averages of the two distributions are also shifted.

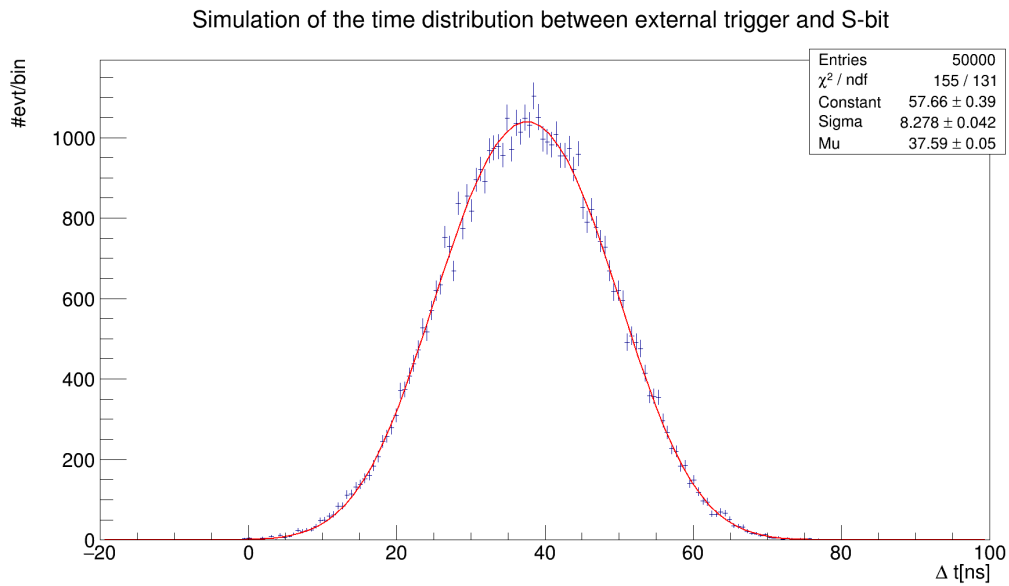


Figure 5.4 – Simulation of a GEM detector having a time resolution of 8 ns for a setup having an uncertainty of 2.5 ns.

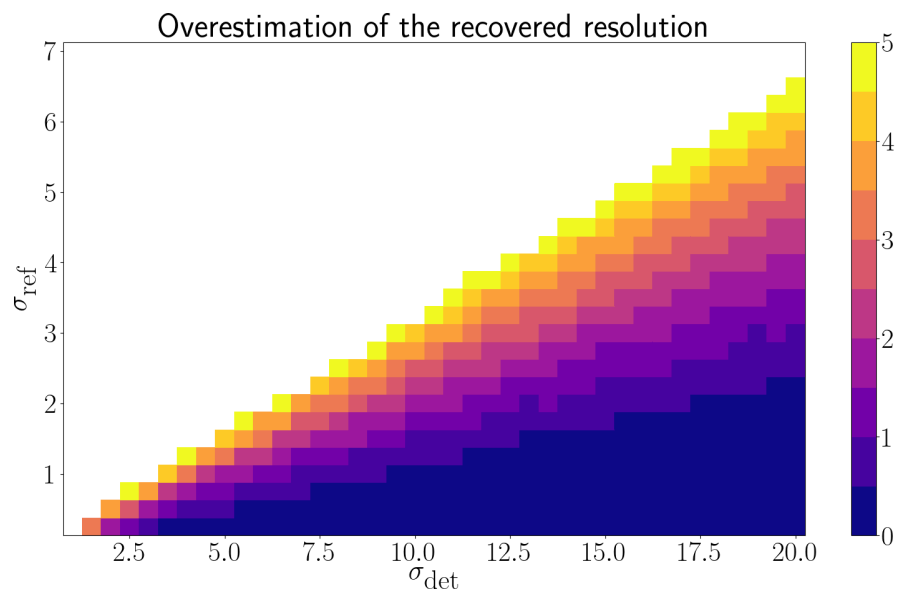


Figure 5.5 – Overestimation in percent for different value of the GEM time resolution,  $\sigma_{det}$ , and setup uncertainties,  $\sigma_{ref}$ .

Moreover, the figure 5.7 shows the overlay of the two distributions obtained with the embedded TDC and the commercial TDC. In order to solve the aforementioned issues, the distributions have been centered around 0 ns and scaled to contain the same number of events.

The similarities confirm that the embedded TDC is indeed able to reproduce the raw results of the commercial TDC. The differences in the signal routes also cause small differences in the uncertainties and so the measured data.

## 5.5 Optimized setup

From figures 5.6, we can clearly see that these first measurements lead to distributions which are too wide and asymmetric compared to what was expected (a time resolution better than 10 ns, see figure 5.4 for example). By applying the fit procedure to the distribution 5.6a, one extracts a time resolution of  $12.39 \pm 0.27$  ns.

In order to understand these distributions and hopefully to improved the measured time resolution, the influence of various setup parameters have been studied and optimized. To do so the possible sources of fluctuation on the time measurement have been factorized into two categories: (1) the effects related to the GEM detector and its front-end electronics, (2) the detectors and the electronics taking part in the creation of the trigger signal.

### 5.5.1 GEM detector optimizations

#### Position on the GEM chamber

As the GEM chamber at ULB could suffer from aging, its electrodes and GEM foils could be bent. This bending causes non-uniformities in the chamber which have two main consequences. First, the electric field cannot be increased as much as in a perfect chamber because of the increased risk of discharges. Second, the time resolution will directly be affected by the imperfections if the electric fields.

By selecting a proper position on the GEM, the second consequence can be minimized. Indeed, a smaller GEM sector closer to the sides of the detector is less subject to deformations. This is why we used the central sector of the second smallest eta row.

#### MSP setting

For easier calibration, the VFAT2 monostable can be configured to smear the threshold crossing from 1 clock cycle to 8 clock cycles. It allows for an easier calibration. Despite it should not impact the time resolution - the TDC only senses the rising edge of the monostable output - it was decided to set the parameter to 1 clock cycle.

#### S-bits lines

At some point, it was thought that the measured distribution was the sum of two of the expected distributions shifted of 25 ns from each other. Indeed, the VFAT2 sends its 8 S-bits through 8 independent tracks which could have different lengths along the GEB. The firmware version which was used does not correct for such effects. Hence, 2 S-bits corresponding to the same bunch crossing and sent at the same time could be sampled at different clock cycles by the FPGA.

The issue was solved by configuring the VFAT2 to send the logical OR of its 128 channels on a single track.

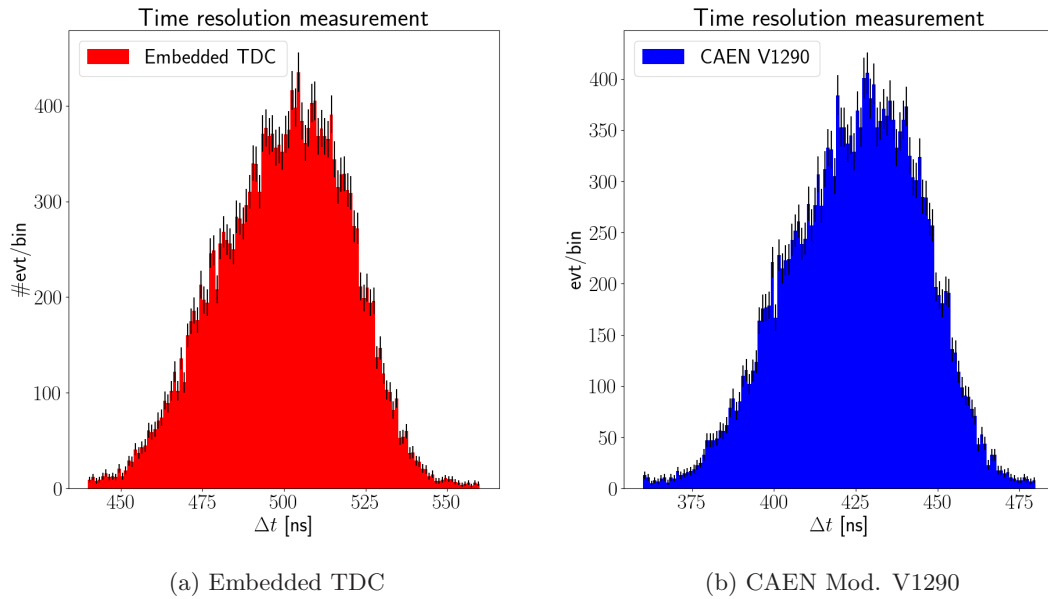


Figure 5.6 – Time distributions with two different TDCs.

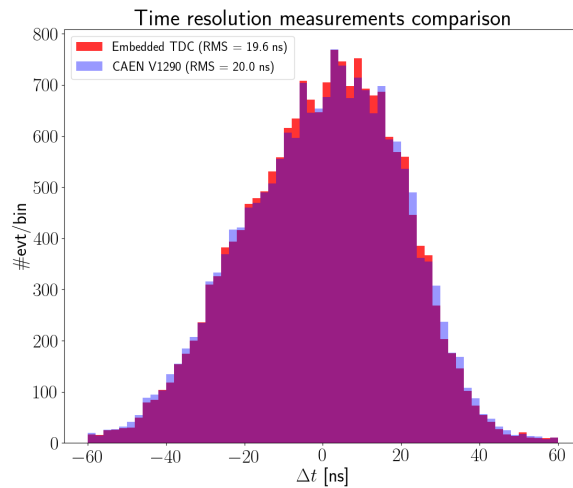


Figure 5.7 – Overlay of the two distributions obtained with the embedded TDC and the commercial TDC. The distributions have been centered around 0 ns and scaled to contain the same number of events.

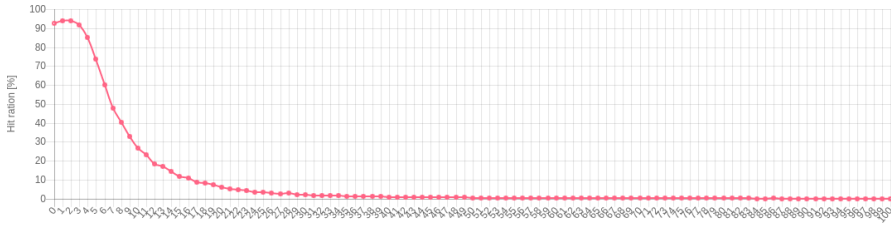


Figure 5.8 – Example of a threshold scan. It shows the passing ratio as a function of the threshold in VFAT units.

### Noise

When acquiring events, one wants to reduce the noise which will degrade the measured time distribution.

Nonetheless, the time resolution measurement can tolerate an higher noise ( $\sim 1\%$ ) than the one which will be used in CMS. Indeed, the timing data is only acquired with the coincidence of 3 detectors, two scintillators and the GEM; the GEM detector has no role in the trigger system. The advantage of accepting an higher noise is the reduction of the threshold and the increase of the efficiency.

In order to correctly set the threshold, one tool called the threshold scan has been developed to measure of the noise on a VFAT2 level.

This scan, implemented in the OH FPGA firmware, computes the ratio of passing events. In absence of signal corresponding the passage of muons, the hits are only caused by noise.

The figure 5.8 shows an example of threshold scan. One can see the evolution of the passing events ratio for an increasing threshold in VFAT units.

For example, the chosen threshold of our setup was 50 VFAT units.

### VFAT2 Signal-to-Noise uniformity

Because of variability in the fabrication processes, the response to a signal can slightly vary from one channel to another. To mitigate that defect and to provide a more uniform Signal-to-Noise Ratio (SNR) response within a single VFAT2 chip, the threshold can be trimmed independently for each channel in a limited range.

The procedure, called *trimmig*, configures each channel after having characterized the VFAT2 by using a procedure called the S-Curves.

The S-Curves are a way of characterising the noise and the sensibility of each VFAT channel individually [22]. The scan is implemented in the OH firmware with the help of the VFAT.

In each VFAT integrates a Digital-To-Analog (DAC) converter that can send pulses of known amplitude to the inputs of the VFAT channels. One can measure the ratio of passing events for signals of increased amplitude at a given threshold.

One exemple of the step part of a S-Curve for the channel 14 of the VFAT used in the setup is represented figure 5.9. The passing ratio increases with the increase of generated signals (in VFAT units).

To increase the efficiency of the calibration, the operation is run at the operating threshold.

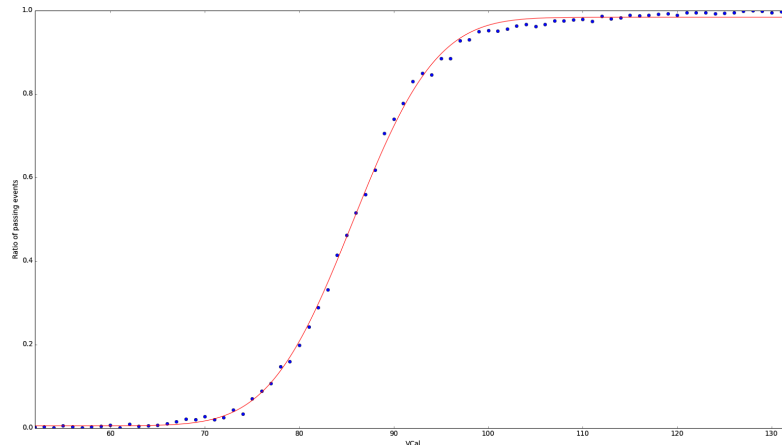


Figure 5.9 – Detail of the step part of a S-Curve. The X axis is graduated in VFAT units whereas the Y axis shows the passing ratio.

Figure 5.10a shows the S-Curves for the 128 channels before trimming as a colormap. Figure 5.10b shows the same information after trimming. One can clearly see the improvement of the uniformity between the channels after the calibration.

### VFAT choice

With the threshold scan and the S-Curves, we are able to select the best VFAT2s, that is the ones which have the less noise and the most uniform response between its channels.

### 5.5.2 Trigger optimizations

The previous section described the improvements which are related the time resolution of the GEM detector and its analog front-end. The figure 5.5 shows that fluctuations of the time reference signal,  $\sigma_{ref}$ , of less than 3 ns could lead to an overestimation of the GEM time resolution,  $\sigma_{det}$  of more than 5% if its time resolution is less than 10 ns.

In order to reduce the overestimation of the time resolution, we optimized and characterized every element composing the trigger.

### Scintillators and photomultipliers

In order to characterize the time response of the PMTs, we measured the time difference between the signal sent by the PMT under under test (PUT) and a reference signal. A Sr90 electron source we used to speed up the process is equipped with two scintillators and PMTs as time reference.

The setup shown on the figure 5.11 was built. It is composed of a Sr90 electron source whose 0.546 MeV electrons are focused to a stack of 3 scintillators. The first two scintillators, called *PM up* and *PM down*, are used as reference while the last one is the PMT under test.

The analog signals of the reference scintillators are fed to simple discriminators whose outputs are sent to a logical AND to produce the reference signal. The PUT was, depending of the test, connected to a simple discriminator or a Constant Fraction Discriminator (CFD).

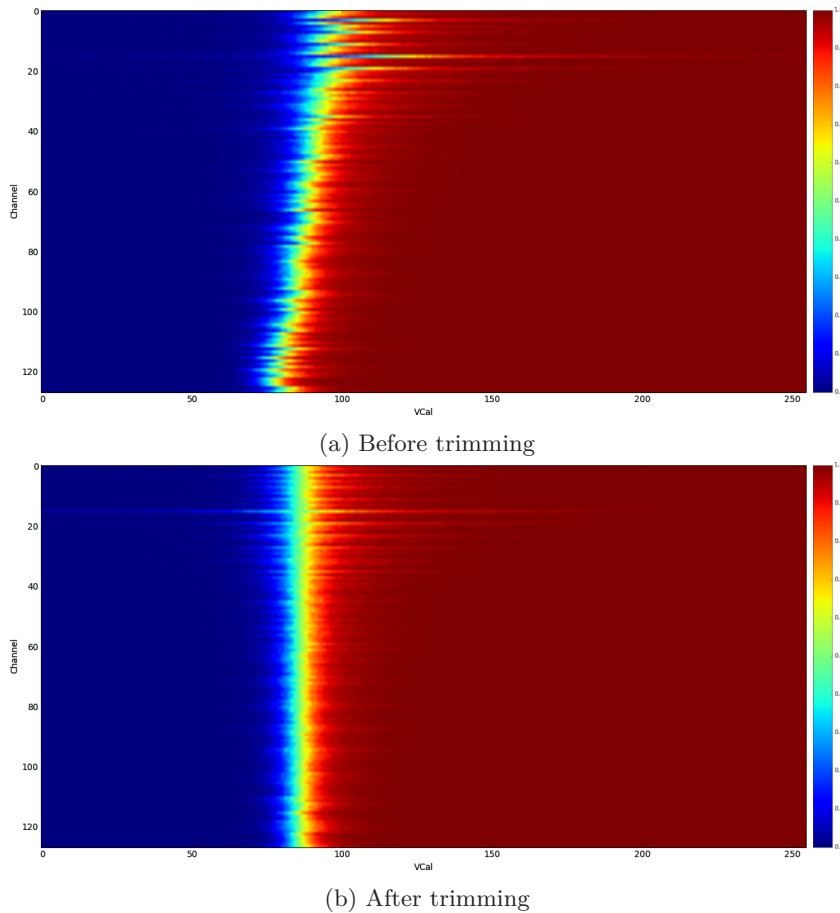


Figure 5.10 – Colormap of the S-Curves for the 128 channels of a VFAT2.

Finally, the time difference between the reference signal and the PUT was measured by a commercial TDC.

We emphasize that the measured time distribution will not provide the time resolution of the PUT. It is only possible to measure the "relative time resolution" between the scintillator-PMTs. However it gives an upper bound on the intrinsic time resolution of the scintillator-PMT.

The figure 5.12 shows the time distribution for the *small PM* and a fit of the sum of two Gaussians with the same mean. These Gaussians have a standard deviation of respectively  $8.4 \pm 0.4$  ns and  $2.5 \pm 0.1$  ns.

After some discussions, the electron sources came out to be very challenging, because of two main factors [23] :

1. The emitted electron can emit a photon via bremsstrahlung in the scintillators or any crossing medium. This photon can be detected by either the PUT or the reference PMTs.
2. The produced photon can produce secondary ionizations in the media which could also be detected by the PUT or the reference PMTs.

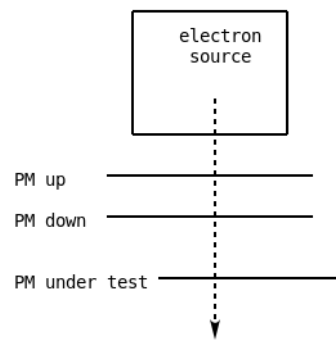
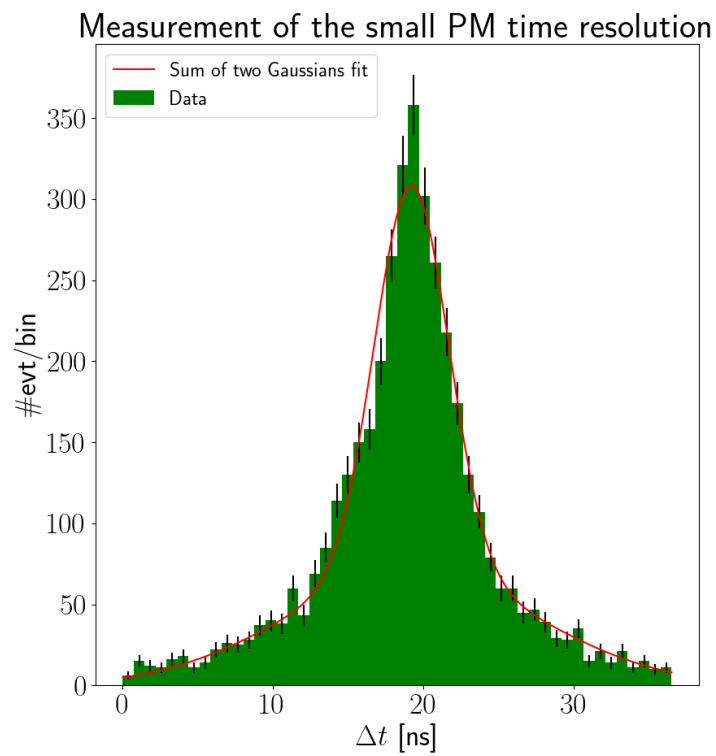


Figure 5.11 – PMTs measurement setup.

Figure 5.12 – Relative time distribution of the *small PM*.

The TDC could then measure events which do not correspond to the original electron :

- The reference time could be early if the reference PMTs detect the bremsstrahlung photon instead of the original electron.
- The reference time could be late if the reference PMTs detect a secondary electron emitted by the photon.
- Even if the reference time corresponds to the original electron from Sr90, the DUT could detect either the bremsstrahlung photon or the secondary electron.

The fit was so done with the sum of two Gaussians : the narrow Gaussian corresponds to the events generated by real electron from the Sr90 while the wider Gaussian corresponds to all the mismatched cases. As said before, the *small PM* with a simple threshold discriminator lead to a narrow Gaussian of  $2.5 \pm 0.1$  ns and a wide Gaussian of  $8.4 \pm 0.4$  ns.

### Constant Fraction Discriminator

In order to improve the time resolution, a Constant Fraction Discriminator (CFD) has been used on the PUT.

The CFD is an electronic processing device which reduces the time walk (and hence improve the time resolution) induced by a simple threshold discriminator. In a simple threshold discriminator, two signals arriving at the same time, but with different amplitudes will cross the threshold at different times as explained in the section 3.4.1.

The CFD method works as follow : the original signal is copied twice. The first copy is delayed by some time  $t_{delay}$ , generally chosen as 80% of the rising time. The second copy is inverted and multiplied by a constant factor  $1/k$ . The sum of these two copies will cross the zero point at the same time for signals of different amplitudes but with the same shape. An example for a GEM signal is given on the figure 5.13.

We tested this method by replacing the PUT by the *PM5*, with or without the CFD. With a simple discriminator, the fitted Gaussians have a standard deviations of  $3.8 \pm 0.8$  ns and  $1.7 \pm 0.4$  ns. With the CFD, the Gaussians have standard deviations of  $4.8 \pm 0.2$  ns and  $1.6 \pm 0.2$  ns. The distributions are shown of figure 5.14a and figure 5.14b for, respectively, with and without the CFD.

The asymmetry in the distribution 5.14b could be explained by an improper configuration of the CFD because of a missing manual. Later on the project, a new CFD was used and properly configured even though it was not individually tested.

### Trigger logic

By properly configuring the coincidence logic, one can reduce the influence of the scintillators timing fluctuations.

The figure 5.15 shows the screenshot a scope screen of the signals involved in the coincidence logic. The magenta signal comes from a simple discriminator connected to one of the bottom PMTs (i.e. one of the *PM3*, *PM4* or *PM5* depending of the measurement in progress). The cyan signal comes from the *small PM* connected to the CFD. The yellow signal is the logical AND of the two other signal and is so the trigger.

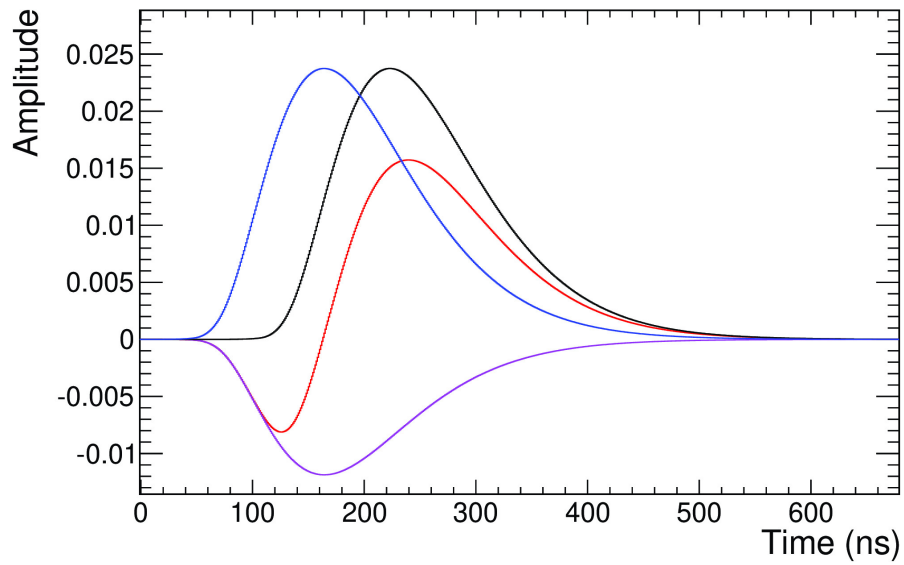


Figure 5.13 – CFD working principle. The original signal is shown blue. The delayed copy is in black while the purple curve is the copy multiplied by  $-1/k$ . The sum of the black and purple signals is shown in red. [thierry\_maerschalk\_study\_2016]

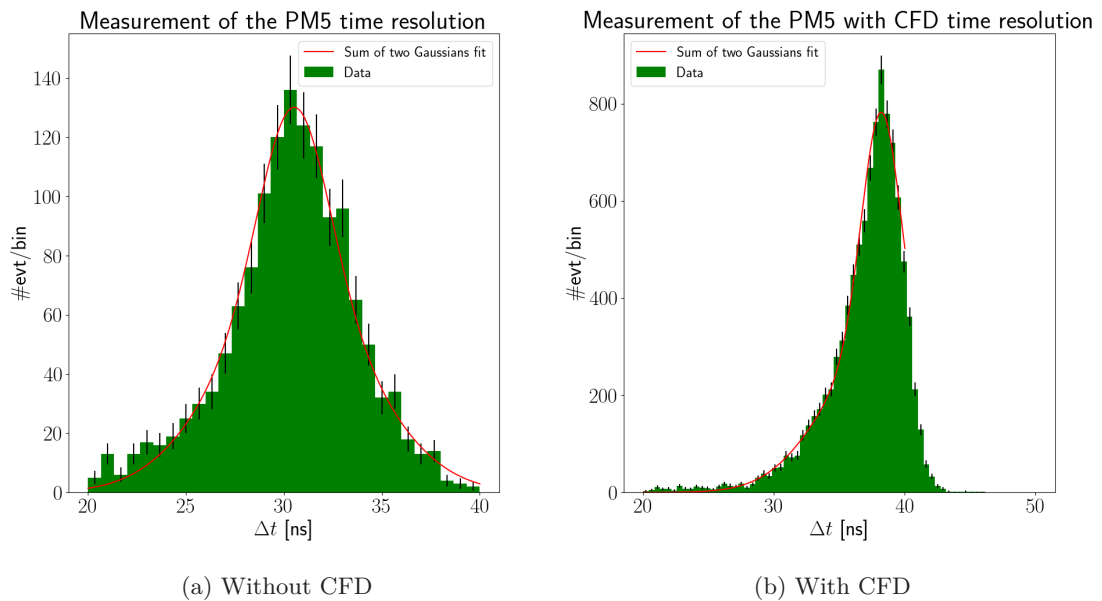


Figure 5.14 – Relative time distributions for the PM5 with a single threshold discriminator (a) and with a CFD (b).

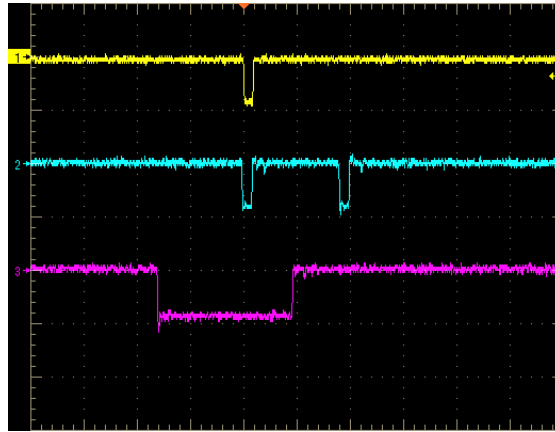


Figure 5.15 – Screenshot of a scope screen measuring the signals involved in the coincidence logic. The yellow signal is the trigger, the cyan signal is the output of the small PM connected to a CFD and the magenta signal is the output of one bottom PMT connected to a simple discriminator. The signals have an amplitude of 800 mV. The horizontal scale is 80 ns/div.

One can see that because the CFD signal is delayed to be more or less in the center of the large window opened by the discriminator, the influence of the jitter in the discriminator is suppressed in the trigger signal. The trigger is only affected by the time resolution of the *small PM* connected to the CFD.

### NIM electronics

The last block to characterize in the block diagram, figure 5.3, is the NIM electronics. Since it is made of commercial modules, we cannot improve this part of the setup, but any induced jitter is easily measurable with a function generator and a TDC.

A function generator was used to send square signals to the inputs of the previously described NIM logic, that is one CFD and one discriminator. The output of the logic, that is the trigger, was connected to one of the commercial TDC. A third copy of the original signals was sent directly to a second input of the commercial TDC.

The measured time distribution between the two inputs of the TDC is represented in figure 5.16. By fitting a Gaussian, one extracts an uncertainty of  $49.3 \pm 0.8$  ps due to the electronics.

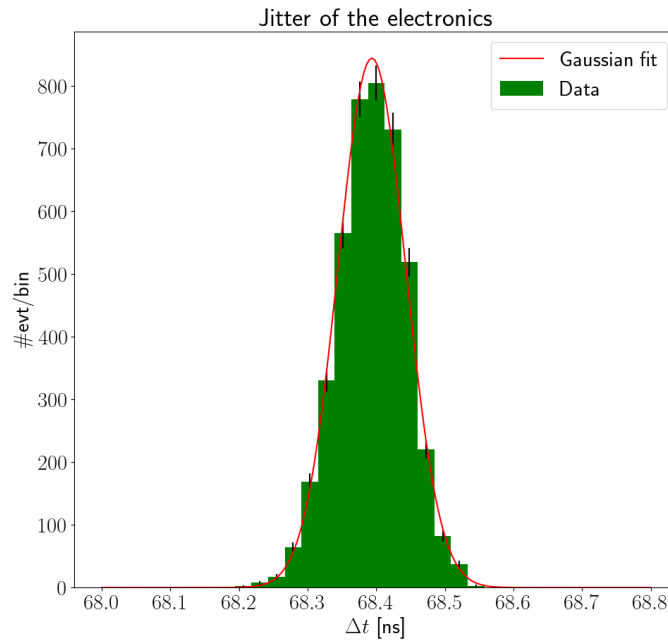


Figure 5.16 – Time distribution of the NIM electronic jitter.

### 5.5.3 Summary

The table 5.1 shows a summary of the uncertainty values previously measured. Assuming the fluctuations are Gaussians, one gets a total uncertainty due to the trigger setup of less than 2.51 ns.

Source of uncertainty	Uncertainty after optimization
S-bits line	0 ns
Small PM	$< 2.5 \pm 0.1$ ns
NIM electronics	$49.3 \pm 0.8$ ns
TDC	$< 150$ ns

Table 5.1 – Summary of the sources of uncertainties and their measured values.

## 5.6 Results

After these various optimisations the measurement of the time resolution is shown in figure 5.17 using the same methodology as previously explained in the section 5.4. The distribution still presents its large asymmetry, caused by late events. Indeed, the late GEM events - compared to the real muon passage  $t_0$  - have smaller time differences than the early events and so appear at the left of the histogram.

By fitting the function 5.1 outside the tail region, one extracts a time resolution of  $12.37 \pm 0.24$  ns, higher than expected. The noise was taken into account by fitting a constant outside the range shown on the figure 5.17.

### 5.6.1 Influence of the drift field

The late events suggested a low drift field in the GEM detector. We increased the high voltage applied to the resistor divider from 3580 V to 3740 V and then to 3860 V.

A summary of the results is shown on table 5.2. Note that the measured time resolution at a drift field of 2.89 kV/cm meets the required CMS GEM specification of better than 10 ns. The time distributions corresponding the 3740 V and 3860 V applied voltage are respectively shown on the figures 5.18 and 5.19.

Beside the improvement of time resolution, the tail of the distribution has clearly diminished.

One can also observe the increase of the mean of distributions. While this phenomenon is not relevant for the time distribution, it is a proof that the gas velocity is increasing with the drift field. Indeed, if the gas velocity increases, the signal is formed earlier as well as the S-bits whereas the external trigger has its fixed latency.

### 5.6.2 Geometrical selection

In order to further improve the time resolution, the measurement was restricted to muons coming perpendicularly to the GEM detector. These conditions are close to those found in CMS.

By using the *PM5* (instead of the *PM3*), located 52 cm under the *small PM*, the muons were selected in a solid angle of about 0.044 sr.

The figure 5.20 shows the produced time distribution. After 12 days of acquisition, only 7895 events were acquired with a drift field of 2.81 kV/cm an efficiency of 80.6%. For its part, the time resolution degrades at  $13.37 \pm 0.21$  ns.

Our hypothesis for explaining this degradation is the variation of the atmospheric pressure and the temperature. During the acquisition period, the atmospheric pressure and the temperature could have significantly changed and, because the gas system is neither controlled in pressure nor in pressure, the pressure and temperature within the detector could have changed as well. As different gas pressures and temperatures imply different gas velocities, the measured distribution is then smeared.

In order to test the hypothesis, we tried to separate the events on time windows spanning from 1 hours to several days and search for improvements. However, the acquisition rate was so slow  $\sim 30$  evt/hour that statistics could not be collected without using the larger time windows, causing the same issue.

### 5.6.3 Conclusions

In this chapter we report on the measurement of the time resolution of a full size CMS GE1/1 (generation III with the v2a electronics) detector filled with 70%Ar+30%CO<sub>2</sub> performed with our TDC implementation embedded in the opto-hybrid FPGA. Our first measurements were quite disappointing with a time resolution of the order of 12 ns while we expected slightly better than 10 ns with these operating conditions.

We have therefore studied, in details, one by one, every components of the experimental setup, trying to find the potential sources of fluctuations spoiling the detector time resolution: different positions along the detector and different VFAT2 chips have been tried, electronics noise and SNR have been optimized, we have mitigated potential time delays in the S-bits transmission along the GEB, we have also scrutinized every components participating in the trigger signal formation, including another source of particles and the influence of a CFD.

At the end the dominant factor leading to a significant improvement of the time resolution is the increase of the electric fields applied to the detector. Indeed increasing the electric field increases the electron drift velocity in the gas and reduces the fluctuations on the arrival time of the electron signal. However the need for the increase of the electric fields in the chamber was not anticipated (according to previous measurements and discussions with experts). One explanation could be that over time the GEM foils are sagging and that the induction gap is actually wider resulting in a lower electric field and lower electron drift velocity.

The sagging in our setup is probable for two reasons: it is an older version of CMS GE1/1 prototype with less efficient GEM foil stretching mechanisms and in our setup the detector is upside-down that is gravity could pull away the GEM foils from the detector electrodes. Anyway despite these complications, at the end we have demonstrated that the CMS GE1/1 detector filled with 70%Ar+30%CO<sub>2</sub> can meet the required 10 ns time resolution if proper electric field configuration is applied to the detector.

Drift field	Time resolution	Tail
2.65 kV/cm	$12.37 \pm 0.24$ ns	✓
2.81 kV/cm	$10.8 \pm 0.1$ ns	×
2.89 kV/cm	$9.91 \pm 0.08$ ns	×

Table 5.2 – Results of the measurements for different drift fields and without selection on the angle of incidence of the muons.

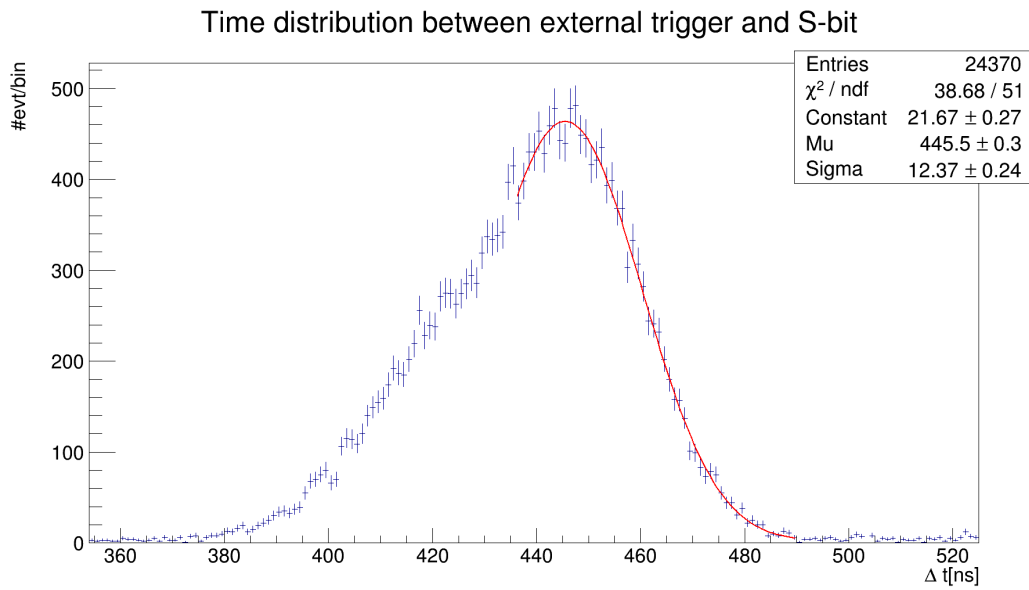


Figure 5.17 – Time distribution for an optimized setup with a drift field of 2.65 kV/cm.

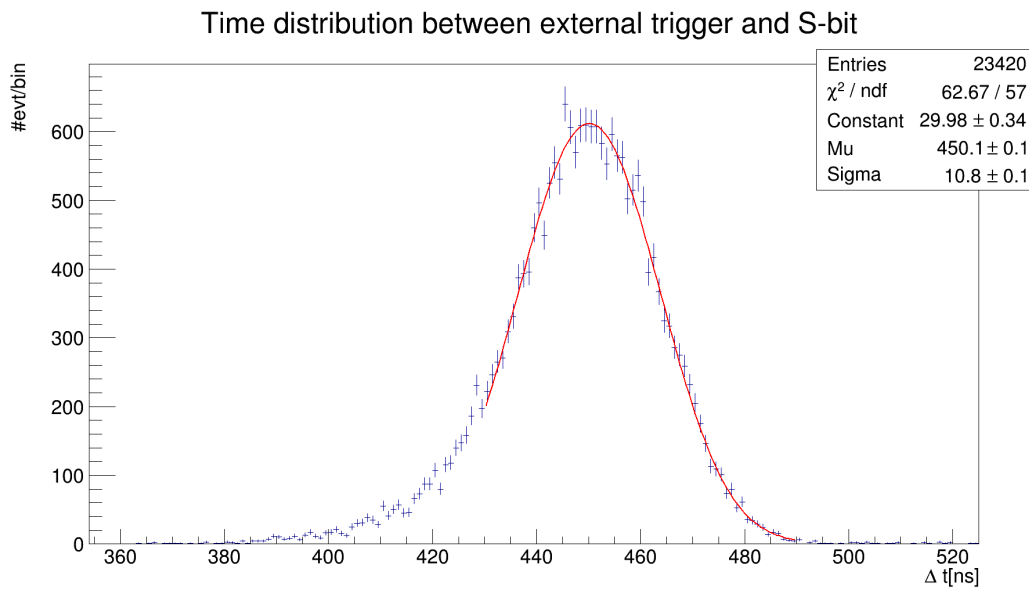


Figure 5.18 – Time distribution for an optimized setup with a drift field of 2.81 kV/cm.

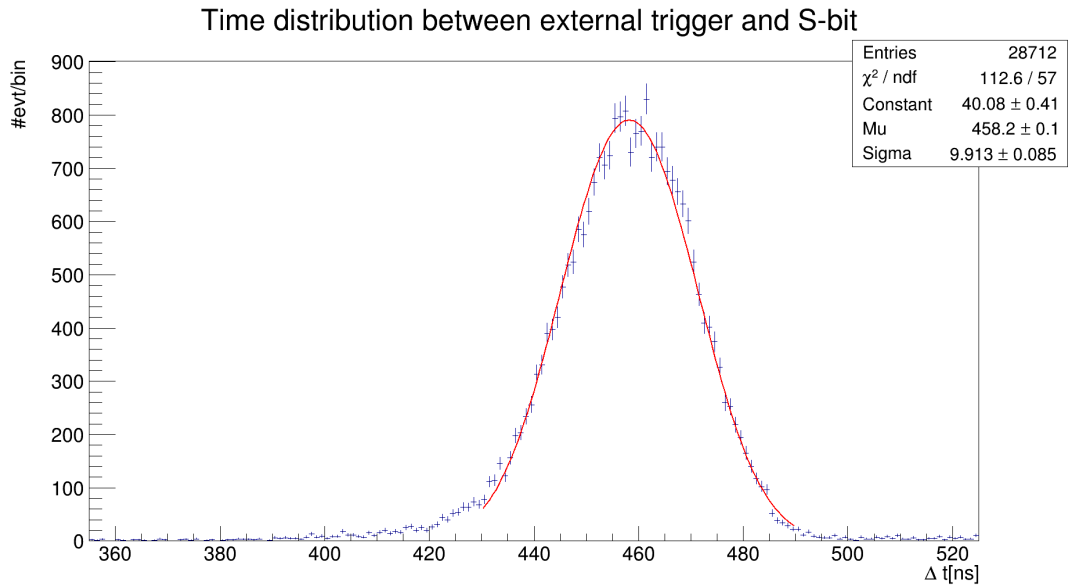


Figure 5.19 – Time distribution for an optimized setup with a drift field of 2.89 kV/cm.

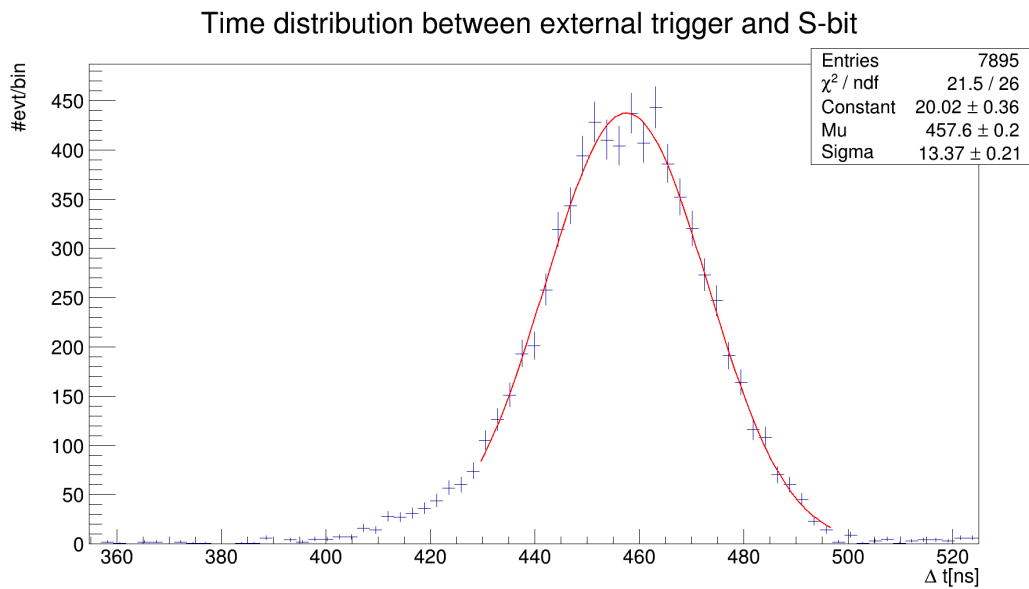


Figure 5.20 – Time distribution for an optimized setup with an higher drift field and a selection on the angles at a drift field of 2.81 kV/cm.

# Conclusion

This master thesis aimed at measuring the time resolution of the triple-GEM detectors with a TDC integrated within a FPGA.

After the LS3 (2024-2026), the HL-LHC should deliver an instantaneous luminosity of up to  $10 \times 10^{34} \text{ cm}^{-2}\text{s}^{-1}$ . As consequence, the CMS experiment will have to cope with higher radiation doses and higher rate of particles, particularly in the endcap regions. The muon subsystem upgrade is designed to maintain the efficiency of the L1 muon trigger while improving the muon track reconstruction as well as increasing the redundancy in the most forward regions.

In this context, the GEM Collaboration has proposed to install an gaseous original detector technology for CMS, called the triple-GEM, in the area left vacant for the innermost layers of RPC detectors in the muon endcap. The first layer of triple-GEM, the GE1/1 project, is planned to be installed in CMS during the LS2 (2019-2020).

Previous studies have proven the ability of the triple-GEM technology to operate in such conditions of radiation and particle rate. All the requirements have been met : among others, the efficiency is above 97%, angular resolution is better than  $300 \mu\text{rad}$  in  $\phi$  and time resolution is better than 10 ns.

Before the commissioning of the detectors in CMS, each GE1/1 chamber will have to be individually tested. In this context, the time resolution must be measured. As the previous solution of using external TDCs does not scale well enough to be used in the quality control steps, we proposed to implement the TDC within the detector electronics in order to automate the measurement.

The development and integration of the TDC within the opto-hybrid v2a firmware was successfully achieved. The diverted use of the FPGA brought complications in the implementation of the delay line. The delays can have strong variations of duration depending of the fabrication process, voltage and temperature. Moreover, race conditions appear between the clock and the data and create bubbles in the sampled vector.

In order to solve these issues and improve the performances of the TDC, the Wave Union-A launcher was implemented as well as a calibration unit. After calibration, we have the longest delay has a duration inferior to 40 ps. When the embedded calibration runs each minute, the TDC achieves a time resolution better than 150 ps in the planned range of operation of  $3.2 \mu\text{s}$ . The complete TDC with 24 synchronous channels and 1 asynchronous channel uses 8268 LUTs, 8699 flip-flops and 128 CARRY4 within the FPGA.

The results of the embedded TDC have been successfully compared with those from a commercial TDC. However, the measured time resolution showed an unexpected asymmetry and an unexpected width compared to the simulations and previous measurements.

In order to improve the results, the detector has been tweaked : the position on the GEM chamber has been optimized, the VFAT2 has been calibrated with the S-Curves methodology and the S-bits were sent by only one LVDS line. The trigger was also improved by using a CFD and properly configuring the coincidence logic. These improvements lead to a fluctuation in the reference trigger of less than  $2.5 \pm 0.1$  ns. The time resolution of one GEM sector was measured at  $12.37 \pm 0.24$  ns with these improvements.

By increasing the drift field from 2.65 kV/cm to 2.89 kV/cm, the tail of the distribution collapsed and the time resolution improved to  $9.91 \pm 0.08$  ns. Previous measurements in similar conditions have however shown time resolution of up to 8 ns.

Finally, only muons coming perpendicularly to the chamber chambers have been selected in order to experience conditions closer to those present in CMS. That measurement did not however show any improvement in the time resolution. The result is even a worsening of the time resolution :  $13.37 \pm 0.21$  ns. Our main hypothesis is that variations in atmospheric pressure could change the drift speed during the long measurement duration.

At the end we have demonstrated that the full-size CMS GE1/1 detector filled with 70%Ar and 30%CO<sub>2</sub> can meet the required 10 ns time resolution although the drift field had to be increased to not anticipated value. Our hypothesis is that the CMS GE1/1 prototype we use has less efficient GEM foil stretching system and, over time, the GEM foils are sagging with gravity. Because of this phenomenon, the induction gap is actually wider resulting in a lower electric field and lower electron drift velocity.

In order to be used in the GEM quality control, the firmware and software are being ported to the v3 electronics. The firmware is finalized and the software is being written. However, the differences in the DAQ system do not allow for a straightforward switch from the v2a electronics to the v3 electronics.

By using new GEM chambers and the CFD of the VFAT3, we expect the time resolution to improve and reach or even excel the previous measurements.

## Appendix A

# Delay line code

```
-----  
-- Company:          IIHE - ULB  
-- Engineer:         Laurent Pétré  
--  
-- Module Name:      tdc_delay_line - rtl  
-- Target Devices:   xc6vlx130t-1ff1156  
-- Tool versions:    ISE P.20131013  
--  
-- Description:  
--  
-- This module is a delay line composed by CARRY4. A positive pulse of  
-- g_PULSE_LENGTH taps is launched when 'in_i' rises. The delay line length is  
-- defined by g_TAPS. As it should be placed as close as possible from the input  
-- pin, we can place it with g_LOC_X and g_LOX_Y.  
-- Only 2 outputs of a CARRY4 are used. It allows a longer delay line for the same  
-- number of taps and avoid empty delays due to routing. Therefore, the number of  
-- CARRY4 primitives used is half of g_TAPS.  
-- The last setting is g_VALID_DISTANCE which defines the position of the valid  
-- flip-flop. It must be placed far enough to have the time for the pulse to be  
-- launched.  
-- The default settings work on target device.  
-- WARNING : taps_o can contain "bubbles" and valid_o is asserted more than one  
-- cycle. Only the first cycle is valid and it always returns to 0 between to  
-- events. However, there two flip-flop rows to prevent metastability.  
--  
-----  
library ieee;  
use ieee.std_logic_1164.all;  
  
library unisim;  
use unisim.vcomponents.all;  
  
entity tdc_delay_line is  
  generic (  
    g_TAPS          : integer := 256;  
    g_PULSE_LENGTH  : integer := 8;  
    g_LOC_X         : integer := 0;  
    g_LOC_Y         : integer := 0;  
    g_VALID_DISTANCE : integer := 18 );  
  port (  
    clk_i   : in std_logic;  
    reset_i : in std_logic;  
  
    in_i : in std_logic;
```

```

        taps_o : out std_logic_vector(g_TAPS-1 downto 0);
        valid_o : out std_logic );
end entity;

architecture rtl of tdc_delay_line is

    signal launch_clr : std_logic := '0';
    signal launch : std_logic := '0';
    signal launch_delay : std_logic_vector(2*g_TAPS-1 downto 0) := (others => '1');

    signal taps_carry_ff : std_logic_vector(2*g_TAPS-1 downto 0) := (others => '0');
    signal taps_ff_ff : std_logic_vector(g_TAPS-1 downto 0) := (others => '0');

    signal valid_ff_ff : std_logic := '0';
    signal valid : std_logic := '0';

    -- Avoid optimisations (synth and P&R)
    attribute DONT_TOUCH : string;
    attribute DONT_TOUCH of rtl : architecture is "true";
    attribute KEEP_HIERARCHY : string;
    attribute KEEP_HIERARCHY of rtl : architecture is "true";

    -- Place all components
    attribute RLOC_ORIGIN : string;
    attribute RLOC_ORIGIN of delay0 : label is "X" & integer'image(g_LOC_X) & "Y" & integer'image(g_LOC_Y);

    attribute RLOC : string;
    attribute RLOC of launch_clr_LUT : label is "X2Y" & integer'image(((2*g_PULSE_LENGTH)+3)/4);
    attribute RLOC of launch_FDCE : label is "X2Y" & integer'image(((2*g_PULSE_LENGTH)+3)/4);
    attribute RLOC of delay0 : label is "X0Y0";
    attribute RLOC of valid_ff1 : label is "X2Y" & integer'image(((2*g_PULSE_LENGTH)+3)/4 + g_VALID_DISTANCE);
    attribute RLOC of valid_ff2 : label is "X2Y1";

begin

    -----
    -- Launch --
    -----

    launch_clr_LUT : LUT2
    generic map (
        INIT => "1110" )
    port map (
        I0 => valid,
        I1 => reset_i,
        0 => launch_clr );

    launch_FDCE : FDCE
    generic map (
        INIT => '0')
    port map (
        D => '1',
        Q => launch,
        C => in_i,
        CE => '1',
        CLR => launch_clr );

    launch_delay_gen: for I in 0 to 2*g_TAPS-1 generate
    begin
        launch_delay_position: if I = 0 or I = 2*g_PULSE_LENGTH generate
            launch_delay(I) <= launch;
        end generate;
    end generate;
end generate;

```

```

-----
-- Delays --
-----
delay0: CARRY4
port map (
    CO    => taps_carry_ff(3 downto 0),
    CI    => '0',
    CYINIT => '0',
    DI    => "1111",
    S     => launch_delay(3 downto 0) );

delays_gen: for I in 1 to g_TAPS/2-1 generate
    attribute RLOC of delay : label is "X0Y" & integer'image(I);
begin
    delay: CARRY4
    port map(
        CO    => taps_carry_ff(4*(I+1)-1 downto 4*I),
        CI    => taps_carry_ff(4*I-1),
        CYINIT => '0',
        DI    => "0000",
        S     => launch_delay(4*(I+1)-1 downto 4*I) );
end generate;

-----
-- FFs for delays --
-----
ffs: for I in 0 to g_TAPS-1 generate
    attribute RLOC of ff1 : label is "X0Y" & integer'image(I/2);
    attribute RLOC of ff2 : label is "X1Y" & integer'image(I/2);
begin
    ff1: FDRE
    generic map (
        INIT => '0' )
    port map (
        D => taps_carry_ff(2*I),
        Q => taps_ff_ff(I),
        C => clk_i,
        CE => '1',
        R => '0' );

    ff2: FDRE
    generic map (
        INIT => '0' )
    port map (
        D => taps_ff_ff(I),
        Q => taps_o(I),
        C => clk_i,
        CE => '1',
        R => '0' );
end generate;

-----
-- Valid bit --
-----
valid_ff1: FDRE
generic map (
    INIT => '0' )
port map (
    D => launch,
    Q => valid_ff_ff,
    C => clk_i,

```

```
        CE => '1',
        R  => '0' );

valid_ff2: FDRE
generic map (
    INIT => '0' )
port map (
    D => valid_ff_ff,
    Q => valid,
    C => clk_i,
    CE => '1',
    R  => '0' );

valid_o <= valid;

end architecture;

-- vim: set expandtab tabstop=4 shiftwidth=4:
```

# List of Figures

1.1	Overview of the CERN accelerator complex. The LHC and its four main experiments are drawn in blue. The proton accelerating chain is composed (in order) by the LINAC2 (purple), the BOOSTER (rose), the PS (magenta) and the SPS (blue). [15]	4
1.2	The planned LHC long term calendar. It will lead to the commissioning of the HL-LHC, High Luminosity-LHC around 2025. [16]	6
1.3	CMS system of coordinates. The beam is along the Z axis. In green and brown, one can see the comparison between the $\theta$ angle and the pseudo-rapidity $\eta$ . [32]	7
1.4	Transverse view of one octant of the barrel of CMS. The lines represent the path of different particles through the different sub-detectors : the tracker in black, the ECAL in green, the HCAL in yellow and the muon system in orange. The solenoid is colored in grey. [30]	8
1.5	Location of the different detectors used in the muon system. The collision point is in the bottom left corner. The DTs (in orange) are only present in the barrel. The CSCs (in green) are located only in the endcaps. The RPCs (in blue) are located both in the barrel and the endcaps. [46]	9
1.6	Overview of the CMS trigger system. The yellow bubbles represent the two levels of trigger processing. They successively select the events to a rate that can be stored.	10
2.1	The energy loss of a $\mu^+$ in Cu. The Bethe-Bloch formula is represented in red. [12]	14
2.2	Formation of an avalanche around an anode wire. [43]	16
2.3	Schematic of a drift tube. The cathode is formed by strips along the side of the tube whereas the anode is a wire stretched in the middle of the tube. [19]	18
2.4	Details of the CSCs. [19]	19
2.5	Sectional view of a 2 gaps RPC detector. The readout strips (in brown) are sandwiched by the two gas volumes. The bakelite plates which protect the electrodes are colored in orange. [28]	19
2.6	Electron microscope picture of a GEM foil. The holes have a typical inner diameter of $50\ \mu\text{m}$ , outer diameter of $70\ \mu\text{m}$ with a pitch of $140\ \mu\text{m}$ . [44]	20
2.7	Schematic of a GEM foil enclosed between a cathode and an anode. The electric field lines are colored in red. The drift paths of the electrons and the ions are represented in blue and in red respectively. [48]	21
2.8	Disposition of the three foils in a Triple-GEM detector. The multiple voltages are derived from a single high voltage (HV) source through a resistor divider. [44]	21
3.1	Location of the detectors used in the muon system after upgrade for LHC Phase II. The triple-GEM based detectors are colored in red. [2]	24
3.2	The CMS endcap. The GE1/1 superchambers are highlighted in light red and cyan. [1]	25
3.3	Exploded view of a GE1/1 chamber. [1]	26

3.4	Overview of the GE1/1 readout electronic. The opto-hybrid, in which the TDC will be implemented, is in blue. [31] . . . . .	27
3.5	Block diagram of the VFAT3. The trigger path is highlighted in red and the tracking data is in blue. [7] . . . . .	29
3.6	Picture of a GEB3. [31] . . . . .	29
3.7	Block diagram of the VFAT2. [6] . . . . .	31
3.8	Time-walk induced by a simple threshold discriminator. The two signals have the same shape, but the red one passes the threshold before the green one only because of its bigger amplitude. [24] . . . . .	31
4.1	The basic structure of an FPGA. We can see the CLBs matrix connected by the routing resources. On the edges, one can identify the IOs. [51] . . . . .	34
4.2	Symbol of a D flip-flop . . . . .	35
4.3	Schematics of the CARRY4 primitive. The path which will be used as the delay line is highlighted in yellow. . . . .	36
4.4	Schematic of an ideal tapped delay line. . . . .	37
4.5	From left to right, more advanced versions of a tapped delay line. The red boxes are the launchers. Each CARRY4 with its flip-flops is in blue. . . . .	39
4.6	Calibration graphics for the FPGA TDC. The data are in blue while the red lines represent the ideal case. . . . .	40
4.7	Time diagram of the signals in the tapped delay line for different launchers. The pulse is released at $t_0$ while it is sampled at $t_1$ by a perfect clock (in blue) or a clock with some skew (in red). . . . .	42
4.8	Time distribution measured by the FPGA TDC for a generated interval of 200 ns. . . . .	43
4.9	Evolution of the time resolution for increasing generated time interval between two channels. The commercial TDC is in red while the FPGA TDC is in blue. . . . .	43
4.10	Block diagram of the TDC implemented within the GE1/1 opto-hybrid. . . . .	45
4.11	Floorplan of the FPGA firmware. The TDC module is in green with the delay chain emphasized in pink. The S-bits cluster packer is in orange. All the others elements are colored in cyan. . . . .	45
5.1	Timing diagram of the measurement. At $t_0$ the particle passes through the setup. The signal is over threshold at $t_1$ , but only sampled by the VFAT2 at $t_2$ . The trigger is asynchronously sent at $t_3$ . . . . .	48
5.2	The experimental setup used for the measurements. It is composed of a GEM detector and its electronics, four scintillators and the electronics required to produce the external trigger. . . . .	50
5.3	Signal and data paths from the GEM detector and the PMTs to the OH TDC. Each element on the signal paths may produce fluctuations on the signal timings. . . . .	51
5.4	Simulation of a GEM detector having a time resolution of 8 ns for a setup having an uncertainty of 2.5 ns. . . . .	52
5.5	Overestimation in percent for different value of the GEM time resolution, $\sigma_{det}$ , and setup uncertainties, $\sigma_{ref}$ . . . . .	52
5.6	Time distributions with two different TDCs. . . . .	54
5.7	Overlay of the two distributions obtained with the embedded TDC and the commercial TDC. The distributions have been centered around 0 ns and scaled to contain the same number of events. . . . .	54
5.8	Example of a threshold scan. It shows the passing ratio as a function of the threshold in VFAT units. . . . .	55

5.9	Detail of the step part of a S-Curve. The X axis is graduated in VFAT units whereas the Y axis shows the passing ratio. . . . .	56
5.10	Colormap of the S-Curves for the 128 channels of a VFAT2. . . . .	57
5.11	PMTs measurement setup. . . . .	58
5.12	Relative time distribution of the <i>small PM</i> . . . . .	58
5.13	CFD working principle. The original signal is shown blue. The delayed copy is in black while the purple curve is the copy multiplied by $-1/k$ . The sum of the black and purple signals is shown in red. [thierry_maerschalk_study_2016] . . . . .	60
5.14	Relative time distributions for the PM5 with a single threshold discriminator (a) and with a CFD (b). . . . .	60
5.15	Screenshot of a scope screen measuring the signals involved in the coincidence logic. The yellow signal is the trigger, the cyan signal is the output of the small PM connected to a CDF and the magenta signal is the output of one bottom PMT connected to a simple discriminator. The signals have an amplitude of 800 mV. The horizontal scale is 80 ns/div. . . . .	61
5.16	Time distribution of the NIM electronic jitter. . . . .	62
5.17	Time distribution for an optimized setup with a drift field of 2.65 kV/cm. . . . .	65
5.18	Time distribution for an optimized setup with a drift field of 2.81 kV/cm. . . . .	65
5.19	Time distribution for an optimized setup with a drift field of 2.89 kV/cm. . . . .	66
5.20	Time distribution for an optimized setup with an higher drift field and a selection on the angles at a drift field of 2.81 kV/cm. . . . .	66

## List of Tables

2.1	Primary ionization $n_p$ and average energy per ion pair $W_I$ for the gases used in the triple-GEM detector. [12] . . . . .	15
3.1	History of the GE1/1 prototypes used in tests. [31] The Slow Control Adapter (SCA) is a radiation hardened ASIC dedicated to the slow control functions. The VTTx and VTRx are radiation hardened optical transmitter and transceiver, respectively. . . . .	30
4.1	Truth table of a D flip-flop. . . . .	35
4.2	Characteristics of the implemented TDC. . . . .	44
5.1	Summary of the sources of uncertainties and their measured values. . . . .	62
5.2	Results of the measurements for different drift fields and without selection on the angle of incidence of the muons. . . . .	64



# Bibliography

- [1] A. Colaleo et al. *CMS Technical Design Report for the Muon Endcap GEM Upgrade*. June 3, 2015.
- [2] D. Abbaneo et al. “Overview of large area triple-GEM detectors for the CMS forward muon upgrade”. In: *Nuclear Instruments and Methods in Physics Research Section A: Accelerators, Spectrometers, Detectors and Associated Equipment*. Proceedings of the Vienna Conference on Instrumentation 2016 845 (Feb. 11, 2017), pp. 298–303. ISSN: 0168-9002. DOI: 10.1016/j.nima.2016.05.127.
- [3] Alice Alfonsi. “Time resolution of a Triple-GEM detector for future upgrade of the CMS muon system”. PhD thesis. ISTITUTO NAZIONALE DI FISICA NUCLEARE : Laboratori Nazionali di Frascati, Apr. 27, 2017.
- [4] The ALICE Collaboration et al. “The ALICE experiment at the CERN LHC”. In: *Journal of Instrumentation* 3.8 (2008), S08002. ISSN: 1748-0221. DOI: 10.1088/1748-0221/3/08/S08002.
- [5] G. Apollinari et al., eds. *High-Luminosity Large Hadron Collider (HL-LHC): Preliminary Design Report*. CERN Yellow Reports: Monographs. Geneva: CERN, Dec. 17, 2015. 285 pp. ISBN: 978-92-9083-422-9 978-92-9083-423-6.
- [6] P. Aspell. *VFAT2 - Operating manual*. July 2006.
- [7] P. Aspell. *VFAT3 Basic Specification V1.3*. May 2015.
- [8] The ATLAS Collaboration. “Observation of a new particle in the search for the Standard Model Higgs boson with the ATLAS detector at the LHC”. In: *Physics Letters B* 716.1 (Sept. 2012), pp. 1–29. ISSN: 03702693. DOI: 10.1016/j.physletb.2012.08.020. arXiv: 1207.7214.
- [9] The ATLAS Collaboration et al. “The ATLAS Experiment at the CERN Large Hadron Collider”. In: *Journal of Instrumentation* 3.8 (2008), S08003. ISSN: 1748-0221. DOI: 10.1088/1748-0221/3/08/S08003.
- [10] Walter Blum, Werner Riegler, and Luigi Rolandi. *Particle detection with drift chambers*. 2. ed. Particle acceleration and detection. OCLC: 254908951. Berlin: Springer, 2008. 448 pp. ISBN: 978-3-540-76683-4 978-3-540-76684-1.
- [11] Rene Brun and Fons Rademakers. *ROOT - An Object Oriented Data Analysis Framework*. Version 6.12/06. Nucl. Inst. & Meth. in Phys. Res. A 389 (1997) 81-86. AIHENP’96 Workshop, Lausanne, Sep. 1996.
- [12] C. Patrignani et al. “Review of Particle Physics”. In: *Chin.Phys.* C40 (Oct. 3, 2016), p. 100001. DOI: 10.1088/1674-1137/40/10/100001.
- [13] CAEN, Guido Esposito, and Pierluigi Barba. *Mod. V1290-VX1290 A/N, 32/16 Ch. Multihit TDC rev.16*. Nov. 29, 2016.

- [14] Canberra. *TC 454 Quad CF Discriminator - Instruction Manual*.
- [15] CERN. *Cern Accelerator Complex*. Mar. 20, 2009.
- [16] CERN. *HL-LHC : Plan 2017-1*. July 31, 2017.
- [17] Communications & Outreach Group CERN : Education. *LHC : the guide*. Feb. 2017.
- [18] The CMS Collaboration. “Observation of a new boson at a mass of 125 GeV with the CMS experiment at the LHC”. In: *Physics Letters B* 716.1 (Sept. 2012), pp. 30–61. ISSN: 03702693. DOI: 10.1016/j.physletb.2012.08.021. arXiv: 1207.7235.
- [19] The CMS Collaboration et al. “The CMS experiment at the CERN LHC”. In: *Journal of Instrumentation* 3.8 (2008), S08004. ISSN: 1748-0221. DOI: 10.1088/1748-0221/3/08/S08004.
- [20] Stefano Colafranceschi. “A study of materials used for muon chambers at the CMS Experiment at the LHC: interaction with gas, new materials and new technologies for detector upgrade”. PhD thesis. Feb. 16, 2012.
- [21] *Detector / CMS Experiment*. URL: <https://cms.cern/detector> (visited on 05/10/2018).
- [22] Hugo Dewitte. *Implementation of an FPGA-based calibration procedure at the detector level for the future high-luminosity phase of the CMS*. 2015.
- [23] Brian Dorney. *Re: Questions about the Triple-GEM time resolution measurement*. Apr. 10, 2018.
- [24] Dschwen. *Comparison of threshold triggering and constant fraction triggering. Own image*. Jan. 25, 2006.
- [25] Matthew W. Fishburn et al. “A 19.6 ps, FPGA-Based TDC With Multiple Channels for Open Source Applications”. In: *IEEE Transactions on Nuclear Science* 60.3 (June 2013), pp. 2203–2208. ISSN: 0018-9499, 1558-1578. DOI: 10.1109/TNS.2013.2241789.
- [26] Claus Grupen and Boris Shwartz. *Particle detectors*. Second Edition. Cambridge Monographs on Particle Physics, Nuclear Physics and Cosmology, 2008.
- [27] Jeremie Alexandre Merlin. *Study of long-term sustained operation of gaseous detectors for the high rate environment in CMS*. CERN Document Server. May 26, 2016. URL: <https://cds.cern.ch/record/2155685> (visited on 05/04/2018).
- [28] S K Park et al. “CMS endcap RPC gas gap production for upgrade”. In: *Journal of Instrumentation* 7 (Nov. 15, 2012), P11013. DOI: 10.1088/1748-0221/7/11/P11013.
- [29] K. Klein. “The Phase-2 Upgrade of the CMS Tracker”. In: (2017).
- [30] Marzena Lapka. *Interactive Slice of the CMS detector*. July 2010.
- [31] G. De Lentdecker. “Lessons learned from GE1/1”. CMS Fwd Muon Upgrade Workshop. Apr. 9, 2018.
- [32] Thomas Lenzi. “Development and Study of Different Muon Track Reconstruction Algorithms for the Level-1 Trigger for the CMS Muon Upgrade with GEM Detectors”. In: *arXiv:1306.0858 [hep-ex, physics:physics]* (June 4, 2013). Gilles De Lentdecker. arXiv: 1306.0858.
- [33] Thomas Lenzi. “Development of the DAQ System of Triple-GEM Detectors for the CMS Muon Spectrometer Upgrade at LHC”. PhD thesis. ULB, Dec. 2016.
- [34] The LHCb Collaboration et al. “The LHCb Detector at the LHC”. In: *Journal of Instrumentation* 3.8 (2008), S08005. ISSN: 1748-0221. DOI: 10.1088/1748-0221/3/08/S08005.

- [35] The LHCf Collaboration et al. “The LHCf detector at the CERN Large Hadron Collider”. In: *Journal of Instrumentation* 3.8 (2008), S08006. ISSN: 1748-0221. DOI: 10.1088/1748-0221/3/08/S08006.
- [36] Chong Liu and Yonggang Wang. “A 128-Channel, 710M Samples/Second, and Less Than 10ps RMS Resolution Time-to-Digital Converter Implemented in a Kintex-7 FPGA”. In: *IEEE Transactions on Nuclear Science* 62.3 (June 2015), pp. 773–783. ISSN: 0018-9499, 1558-1578. DOI: 10.1109/TNS.2015.2421319.
- [37] Thierry Maerschalk. “Study of Triple-GEM detector for the upgrade of the CMS muon spectrometer at LHC”. Gilles De Lentdecker. PhD thesis. 2016.
- [38] Arabella Martelli. “The CMS HGCAL detector for HL-LHC upgrade”. In: *arXiv:1708.08234 [hep-ex, physics:physics]* (Aug. 28, 2017). arXiv: 1708.08234.
- [39] P. Moreira et al. *The GBT Project*. CERN Document Server. 2009. URL: <https://cds.cern.ch/record/1235836> (visited on 05/19/2018).
- [40] J. L. Pinfeld. “The MoEDAL Experiment at the LHC – a New Light on the Terascale Frontier”. In: *Journal of Physics: Conference Series* 631.1 (2015), p. 012014. ISSN: 1742-6596. DOI: 10.1088/1742-6596/631/1/012014.
- [41] Corinne Pralavorio. *Record luminosity: well done LHC / CERN*. Dec. 14, 2017. URL: <https://home.cern/about/updates/2017/11/record-luminosity-well-done-lhc> (visited on 05/11/2018).
- [42] S. Bonacini, P. Moreira, and K. Kloukinas. “e-link: A radiation-hard low-power electrical link for chip-to-chip communication”. In: (2009).
- [43] Fabio Sauli. “Principles of operation of multiwire proportional and drift chambers”. In: CERN, Geneva, 1975.
- [44] Fabio Sauli. “The gas electron multiplier (GEM): Operating principles and applications”. In: *Nuclear Instruments and Methods in Physics Research Section A: Accelerators, Spectrometers, Detectors and Associated Equipment*. Special Issue in memory of Glenn F. Knoll 805 (Jan. 1, 2016), pp. 2–24. ISSN: 0168-9002. DOI: 10.1016/j.nima.2015.07.060.
- [45] The CMS Collaboration. *LumiPublicResults < CMSPublic < TWiki*. URL: <https://twiki.cern.ch/twiki/bin/view/CMSPublic/LumiPublicResults> (visited on 05/11/2018).
- [46] The CMS Collaboration. “The performance of the CMS muon detector in proton-proton collisions at  $\sqrt{s} = 7$  TeV at the LHC”. In: *Journal of Instrumentation* 8.11 (Nov. 4, 2013), P11002–P11002. ISSN: 1748-0221. DOI: 10.1088/1748-0221/8/11/P11002. arXiv: 1306.6905.
- [47] The TOTEM Collaboration et al. “The TOTEM Experiment at the CERN Large Hadron Collider”. In: *Journal of Instrumentation* 3.8 (2008), S08007. ISSN: 1748-0221. DOI: 10.1088/1748-0221/3/08/S08007.
- [48] *Welcome on triple GEM detector R&D : IMAGEM and GEMINI*. URL: <https://web.infn.it/GEMINI/index.php/component/content/article?id=2:scientific-program> (visited on 07/12/2018).
- [49] Cheuk-Yin Wong. *Introduction to High-Energy Heavy-Ion Collisions*. WORLD SCIENTIFIC, Sept. 1994. ISBN: 978-981-02-0263-7 978-981-4277-54-9. DOI: 10.1142/1128.
- [50] Jinyuan Wu and Zonghan Shi. “The 10-ps wave union TDC: Improving FPGA TDC resolution beyond its cell delay”. In: *Nuclear Science Symposium Conference Record, 2008. NSS’08. IEEE* (2008), pp. 3440–3446.
- [51] Xilinx, Inc. *Xilinx Introduction to FPGA Design with Vivado High-Level Synthesis (UG998)*.

- [52] Xilinx, Inc. *Xilinx UG364 Virtex-6 FPGA Configurable Logic Block User Guide*.